2021

Ligand Effects on Electronic, Magnetic, and Catalytic Properties of Clusters and Cluster Assemblies

Dinesh Bista
Virginia Commonwealth University

Ligand Effects on Electronic, Magnetic, and Catalytic Properties of Clusters and Cluster Assemblies

A Dissertation Submitted in Partial Fulfillment of the Requirements for the Degree

of Doctor of Philosophy in Nanoscience & Nanotechnology at

Virginia Commonwealth University

by

Dinesh Bista

Director: Shiv N. Khanna, Ph.D.

Chairman and Commonwealth Professor, Department of Physics

Virginia Commonwealth University

Richmond, Virginia

July 2021

Dedicated to my late Sister Devi Bista

ACKNOWLEDGMENTS

Contents

List of Figures

List of Tables

Abstract

LIGAND EFFECTS ON ELECTRONIC, MAGNETIC, AND CATALYTIC PROPERTIES OF CLUSTERS AND CLUSTER ASSEMBLIES

By Dinesh Bista, Ph.D.

A dissertation submitted in partial fulfillment of the requirements for the degree of Doctor of Philosophy in Nanoscience & Nanotechnology at Virginia Commonwealth University.

Virginia Commonwealth University, 2021

Major Director: Shiv N. Khanna, Ph.D.

Commonwealth Professor and Chairman, Department of Physics

Ligands commonly protect metallic clusters against reacting with outside reactants. However, ligands can also be used to control the redox properties enabling the formation of super donors/acceptors that can donate/accept multiple electrons. This thesis focuses on how the ligands can be used to control the electronic and magnetic features of clusters and ligand stabilized cluster-based assemblies, leading to nano pn junctions with directed transport, the possibility of light-harvesting, and catalysts for cross-coupling reactions. The thesis addresses three distinct classes of clusters and their applications. The first class of cluster "metal chalcogen clusters" is the central idea of the thesis focused on recent experiments where metal-chalcogenide clusters have been stabilized in solutions, where clusters assemblies have been synthesized by combining them with counter ions. We also

investigate the fusion of metal-chalcogenide clusters leading to nano pn-junctions with immense dipole moments and their potential applications in photovoltaics and spintronics.

We then investigate simple metal clusters and show how ligands can control the ionization characteristics of aluminum-based clusters and how assemblies of such clusters linked through organometallic wires can form dimer with a significant dipole moment enabling directed transport, applicable in photovoltaics. Finally, we demonstrate how transition metal (palladium-based) clusters adsorbed on double vacant graphene, reduced graphene oxide, and graphene-acid-based supports catalyze cross-coupling reactions in different ligand environments. The graphene supports can also be realized as the solid-state ligands for cross-coupling reactions.

Organization of Thesis

The thesis work is arranged as follows:

Chapter 1

The first chapter introduces the overview of the atomic clusters. Additionally, the concept of superatom, magnetic superatom, cluster assembly using metal-chalcogenide clusters, and the role of ligands in cluster assembly are reviewed.

Chapter 2

The second part of this chapter briefly summarizes the methodology, i.e., density functional theory(DFT). It briefly summarizes the computational details of the subsequent research works done.

Chapter 3

The third chapter discusses the ligand effects on the atomic cluster, including simple metal, metal-chalcogenide, metal-oxide, transition metal clusters, etc. The observed variation in the electronic properties of the atomic clusters due to ligand effects is generalized using phosphine ligands. Furthermore, the physical reason behind a general trend of lowering ionization energy (IE) with phosphine ligation is also offered.

Chapter 4

This chapter presents the dimer formation by combining the ligated metal-chalcogenide clusters. The electronic and magnetic properties of the fused dimers and their potential application as a nono-pn junction and their use in photovoltaics and spintronics-related applications are explored. On the other hand, a theoretical verification of the experimentally synthesized cluster assembled material $[(Co_6Se_8(PEt_3)_5)_2).C_{140}]$, using metal-chalcogenide dimers as a building block is also given. An intriguing phenomenon of the interfacial magnetic moment localized at the junction of the $(Co_6Se_8(PEt_3)_5)_2$ dimer is also expounded.

Chapter 5

It is a short chapter, pretty much like an extension of the third chapter on the fused dimer. The dimer formation is not limited to the metal-chalcogenide clusters but can also be extended to the simple metallic clusters. However, the direct fusion of two simple metallic clusters (aluminum-based clusters) leads to coalescence, and an organometallic linker is needed to link two simple metal clusters. Furthermore, their potential application in photovoltaics is elaborated using time-dependent density functional theory (TDFT).

Chapter 6

In this chapter, the potential applications of transition metal clusters (palladium clusters) in catalysis are explored. Palladium clusters adsorbed on various graphene supports are compared to pursue an improved catalytic performance of the Suzuki cross-coupling reactions.

Chapter 7

The last chapter summarizes all the works contained in the thesis. In addition, the future directions and possible applications of the included results are also briefly analyzed.

Note: The references are given immediately after each chapter.

Chapter 1

Introduction to Clusters and Ligated Cluster Assemblies

Cluster science is a rapidly growing field that offers exciting prospects in understanding the properties of materials and creating exotic materials for human needs. Atomic clusters are defined as a combination of a few to a few hundred atoms that cannot be described by electron-precise bonding, and clusters have emerged as a new phase of matter, intermediate between atoms and bulk materials.[1] In this regime, the properties are governed by quantum confinement due to restricted size. The rise in the interest in cluster science lies in the following two factors.

1) The atomic clusters can be treated as a bridge connecting the ideas between atoms and the bulk materials.[2] Their study can help understand the evolution of electronic, magnetic, and optical properties when atoms come together to form a bulk material.

2) The connection of clusters to the field of nanoscale science seems increasingly profound, where the clusters can serve as the building blocks for new materials with tunable properties. Experimental and theoretical research works over the past few decades have shown that novel behaviors can emerge as the cluster size is reduced to the sub-nanometer scale. The electronic, chemical, and optical properties are found to change with the cluster size. For example, clusters of inert metals like Au are found to be good catalysts, while clusters of a non-magnetic solid like Rh or Pd exhibit magnetic character. More importantly, properties can change dramatically even by the addition of an atom or an electron. For example, the reactivity of Fe_n clusters is found to vary by order of magnitude through just an atom's addition. Consequently, clusters provide an unprecedented strategy to create materials with tailored electronic, magnetic, and optical properties using a bottom-up approach.[3] Such cluster-assembled materials, with their unique properties, can enlarge the scale of materials science.

Not all clusters can maintain their identity as they are assembled, and the stability of a cluster is critical in synthesizing cluster assembled materials. Consequently, identifying clusters that are stable and maintain their identity is crucial in forming the cluster assembled nanoscale materials. In this regard, identifying the physical principles that control the stability of clusters is an essential step in creating such materials. For clusters of metallic elements, the conceptual development of "superatoms" provides a framework for identifying such species.[1] The term superatom, coined by Prof Khanna et al., can be defined as an atomic cluster with a well-defined valence. The clusters' chemical and electronic properties may be projected by their proximity to this valence. A brief overview of atomic clusters, emphasizing ligated metal-chalcogenides clusters, the superatomic concept, and magnetic superatoms, will appear later in this chapter.

1.a Atomic clusters: An agglomeration of a few to a few hundred atoms that are marked by a deficiency of electron-precise bonding constitute an atomic cluster, and clusters show different physical, chemical, and magnetic properties compared with their bulk counterparts. The study of clusters helps us understand the evolution of the structure and collective properties of matter, such as the electrical conductivity, melting point, color, magnetic characters, etc. Size regimes are crucial when dealing with atomic clusters. A schematic view of how properties of matter evolve from a single atom to the bulk solid is shown in Figure 1.1. When the size of a material is reduced, the properties showed a monotonic variation initially, as labeled as a scalable regime in Fig 1b. However, when a critical size (~100 nm or 10^4 atoms) is reached, the variation in properties becomes nonmonotonic. Nanoparticles belong to this critical regime; still, their properties are not highly responsive to the addition or removal of a
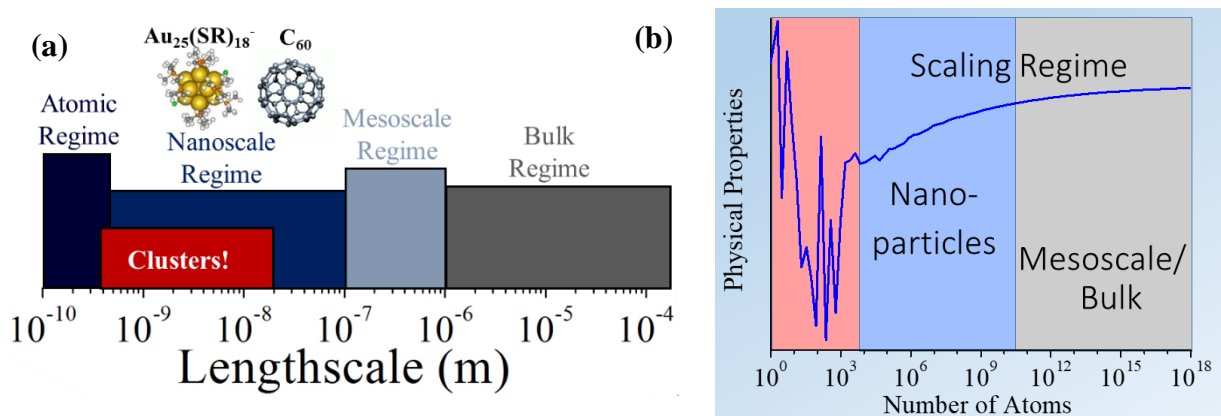
Figure 1.1 (a) Regime of solids with respect to lengthscale (b) Variation in Physical Properties of materials with number of atoms. (Figure Credit Professor Arthur C. Reber)

single atom or an electron.[2] As the particle size is further reduced, the properties change is abrupt and unexpected. Even the addition or removal of a single atom or electron may induce a drastic change in the properties.[4,5] This includes clusters of non-magnetic solids becoming magnetic,[6] reactive metals turning out to be inert,[7] and noble metals showing catalytic activity.[8] The quantum confinement and a large volume to size ratio are responsible for the observed nonmonotonic behaviors. Quantum confinement is defined as a regime where the electron wavelength and its particle size become comparable. Additionally, for the particle size in this regime, the large percent atoms are on their surface; hence such a larger large volume to size ratio plays a crucial role in the unpredictable behaviors of the atomic clusters[9].

One of the biggest breakthroughs in cluster science occurred in 1984 when Knight and co-workers investigated size-selected alkali metal clusters (Na_n) in an interaction-free environment.[9] The mass spectra of alkali metal (Na_n) clusters revealed that specific sizes were more abundant than others, as seen by prominent peaks at N=8, 20, 40, 58, and 92, as seen in Figure 1.2(a).[9] These were labeled as magic numbers in analogy with nuclear physics, where certain nuclei have higher binding energy. It can be understood by using a simplified model called the nearly free electron

gas model, where a cluster could be modeled by a quantum gas of nearly free electrons confined to a sphere with a uniform positive background of the size of the cluster. In addition to the peaks at mass spectra, the magic sizes showed higher ionization energy and low polarizability, patterns consistent with filled electronic shells. The quantum states in such a confined nearly free electron gas are grouped into shells that are in order as 1S, 1P, 1D, 2S, 1F, 2P, ... The model reported the observed magic numbers in Na_n clusters at sizes 2, 8, 18, 20, 34, 40, 58, and 92.

(a)
(b)
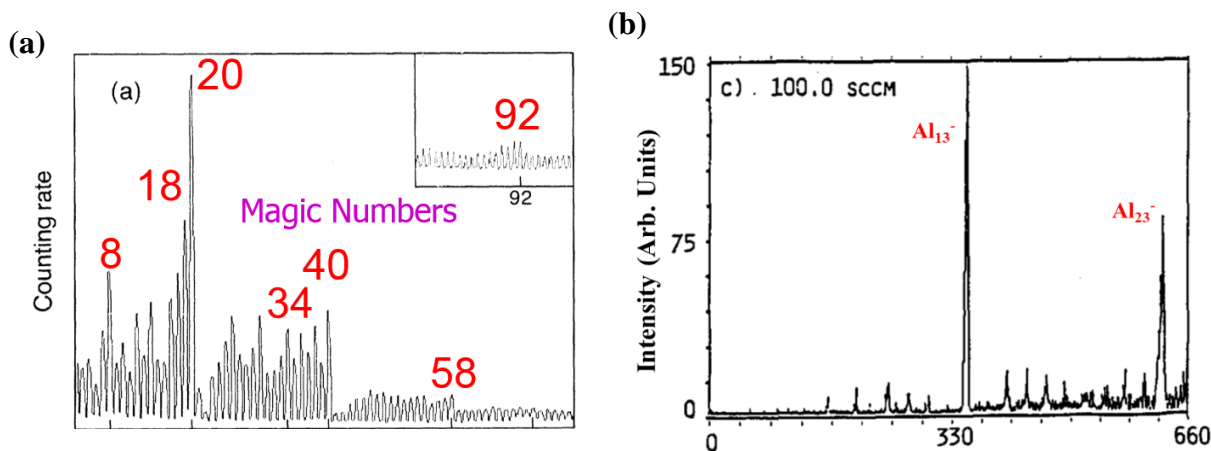
Figure 1.2 (a) Mass Abundance spectrum of Sodium "Na" clusters (Reproduced With Permission)[9](b) Series of mass spectra showing progression of the etching reaction of aluminum cluster anions with oxygen showing peaks at Al_{13}^- and Al_{23}^-(Reproduced With Permission).[5]

More direct evidence is that the electronic shells control the chemistry emanated from experiments on the reactivity of aluminum cluster anions with oxygen. Bulk aluminum is highly reactive with oxygen, but experiments on Al_n^- revealed that clusters including Al_{13}^-, Al_{23}^- ... were resistant to reacting with oxygen, as shown in Figure 2(b).[5] This could be the consequence of filled electronic shells with 40 and 70 electrons, respectively, thus providing explicit chemical evidence of the electronic shell picture. Using this model, an Al_{13}^- had an electronic configuration of $1S^2$, $1P^6$,

4

$1D^{10}$, $1F^{14}$, $2P^6$. This electronic configuration resembled a halogen anion and raised the prospect of an Al_{13} cluster behaving like a halogen atom. Theoretical studies indeed predicted an electron affinity of 3.34 eV for the Al_{13} cluster that was afterward corroborated by experiments.[6] Figure 1.3 compares Cl atom with Al_{13} cluster. Subsequent combined experimental and theoretical findings confirmed that an Al_{14} with 42 valence electrons behaved much like an alkaline earth element.[10] These findings led to a burst of work detecting clusters that mimic multiple valence and magnetic elements.
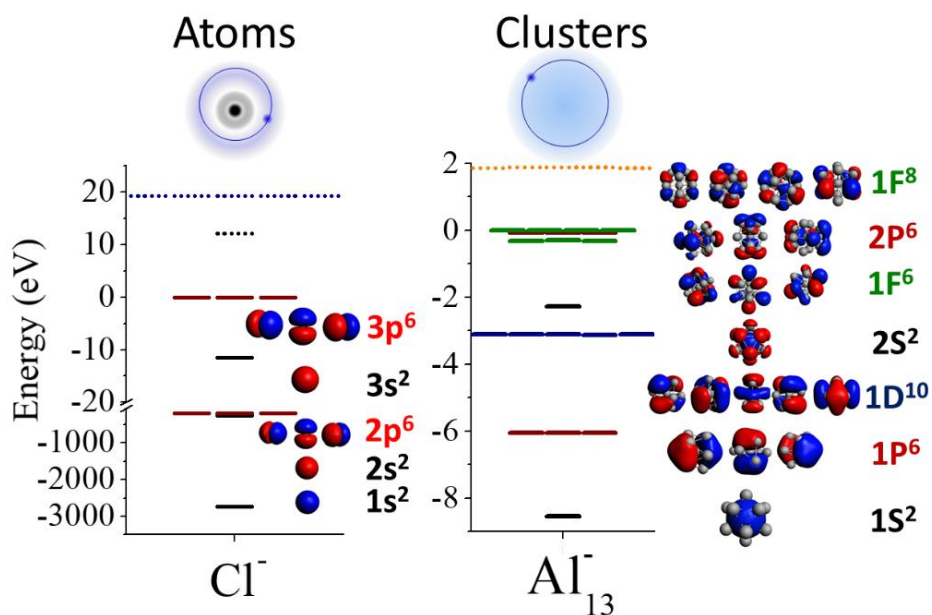
Figure 1.3 Energy levels in atoms and clusters. Electronic levels in a Cl^- atom and Al_{13}^- cluster. (Reused with permission, Copyright American Chemical Society)[11]

b) Superatoms

Symmetric compact clusters have electronic states clustered into electronic shells. The occupancy of the electronic shells defines the chemical behavior of clusters. Clusters with filled shells are found to be more stable, just as found in atoms. Likewise, the clusters with unfilled shells may exhibit a chemical valence, just like in atoms. These features were originally understood for the confined nearly free electron gas is not limited to metal clusters. Hence, the nature of electronic

interactions leading to the filled electronic shells may differ depending on the type of the cluster, and several stable clusters have shown well-defined valence. Hence, these clusters can be deemed
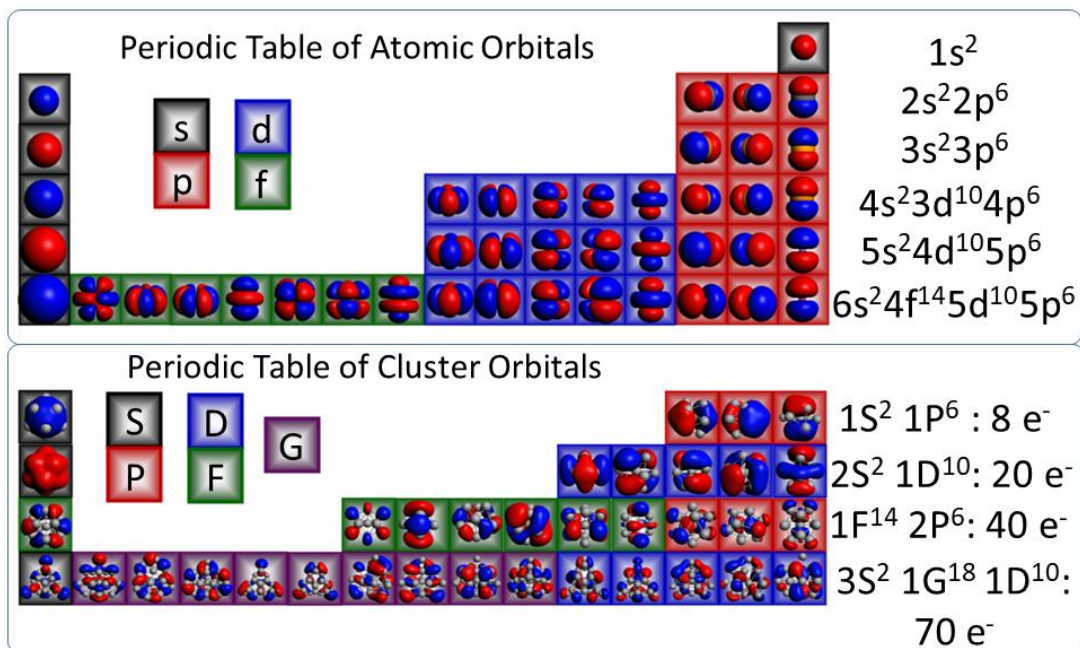
Figure 1.4 A pictorial representation of the periodic table of atomic and superatomic orbitals.(Reused with permission, Copyright American Chemical Society)[11]

as superatoms forming the 3rd dimension of the periodic table.[11] Superatom is a powerful organizing principle for understanding stability of atomic clusters is the concept of "superatom".[1] When a stable cluster keeps its properties intact even after reacting with etchants, these clusters are regarded as "superatom", the name coined by Khanna et al. Previous studies by Khanna and Castleman and co-workers had proposed superatoms resembling alkali, alkaline earth, and multiple valence atoms abundance spectra in larger alkali and alkaline earth systems showed enhanced stability of clusters with complete geometrical shells.[10,12] Furthermore, discovery and characterization of $Al_{13}I^-$ and $Al_{13}I_2^-$ showed that the negative charge is pulled towards Al_{13} even in the presence of iodine.[10] Hence, the Al_{13} cluster displays characteristics of a "super-halogen".

Al_{13}^{-} has enhanced stability from electronic shell closure with 40 electrons. Al_{13} and Al_{14} exhibit behavior of halogen and alkaline-earth metal-like behaviors with one electron deficiency and with two extra electrons, respectively. Hence, Khanna et al. proposed superatoms to form a 3rd dimensional periodic table, as shown in Fig 1.4. The geometric structure also plays a pivotal role in the chemical stability and properties of clusters. For example, superatomic cluster $Ni_9Te_6(PR)_8$ shows stability despite an open electronic shell.[13] Likewise, certain anions of the aluminum cluster that have closed electronic shells are found to be highly reactive when reacted with polar etchants such as water or methanol.[11] This reactivity corresponds to the open geometric structure. Hence, both geometric and electronic shell closure plays a dividend in acquiring stability.[11] Apart from the jellium model, the Wade-Mingos rule[14] and covalent bonding, as shown in Figure 1.5, can also help explain the stability of atomic clusters. The superatoms can be designed to act as both superhalogen and superalkali.[15]
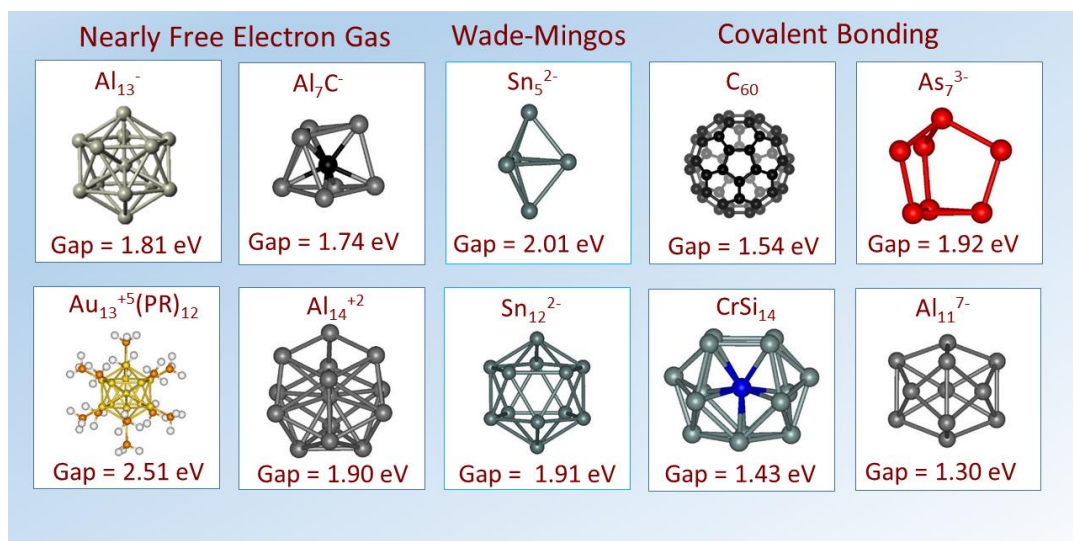
Figure 1.5 Cluster stabilizations explained through NFE, Wade-Mingos, and covalent bonding.

c) Metal clusters:

During the last three decades, metal clusters have been the most extensively explored clusters by experimental and theoretical means. Clusters formed by atoms that form metallic systems in bulk are designated metal clusters. Additionally, metal clusters can be segmented into simple metal, transition metal (TM), noble metal, and mixed or alloy clusters.

i) Simple Metal clusters: The clusters comprised of atoms from group-IA (alkali), group-II(alkaline), and group-IIIA metal elements are called simple metal clusters. The bonding in these clusters is mainly through the delocalized valence electrons of s and p orbitals. The main feature of simple metal clusters is that their stability can be explained by nearly free electron gas theory. One of the most interesting simple metal clusters is Al_{13}^-, also labeled as the first superatom,[6] shown in Figure 1.6, is a very stable cluster with an HL gap of 1.87 eV. In comparison, the Al_{13} cluster behaves much like a halogen exhibiting a momentous electron affinity (EA) of 3.4 eV. Using 3 valence electrons for an Al atom, the Al_{13} cluster corresponds to 39 valence electrons leading to an open shell electronic configuration $1S^2$, $1P^6$, $1D^{10}$, $2S^2$, $1F^{14}$, $2P^5$. When an electron is added to the Al_{13} cluster to form an anion Al_{13}^-, the valence electrons become 40, which is a magic number providing stability through the electronic shell closure. F
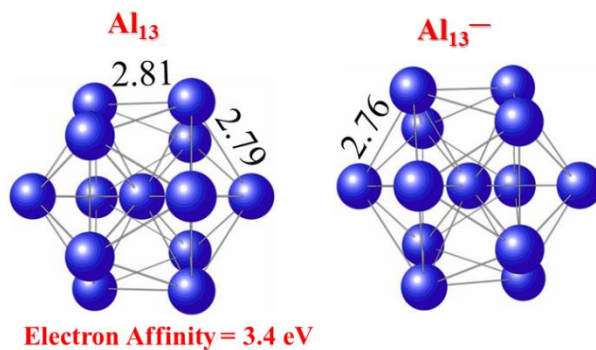
Figure 1.6 First superatoms: Al_{13} and Al_{13}^-.

ii) Transition metal clusters: The transition metal (TM) clusters comprise atoms from 3d, 4d, and 5d series elements. The main characteristic of the transition metal clusters is the partially occupied d orbitals. They commonly favor compact atomic arrangements like icosahedral structures. One of the most exciting features of TM clusters is their magnetic character owing to their partially occupied d orbitals.
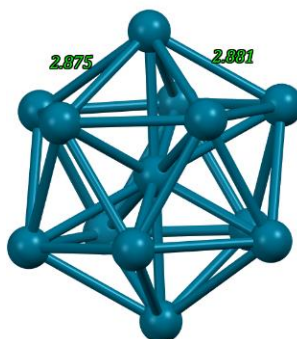
Figure 1.7 Optimized ground state structure of Pd_{13} cluster.

For illustration, Co_N and Fe_N clusters exhibit superior magnetic moments than their corresponding bulk equivalents.[16] The jellium model cannot explain the stability of the transition metal clusters. One of the most exciting transition metal clusters is Pd clusters due to their appeal for catalysis.[17] The Pd_{13} cluster shown in Figure 1.7 is extensively used in catalysis as Pd has a very stable 0 and +2 oxidation state, and hence it can switch back and forth between those oxidation states easily. Therefore, Pd can both act as a very good 2-electrons donor in an oxidative addition stage and an excellent 2e acceptor in the reductive elimination step during cross-coupling reactions. It will be discussed in detail in chapter 5.

iii) Ligated Metal chalcogenide clusters: Chalcogens are the elements of group 16 in the periodic table, including, Sulfur, Selenium, and Tellurium atoms, which accommodate six electrons in their valence shell. Hence, -2 is the most common oxidation state for these elements; however, the +2, +4, and +6 are also possible. A Chalcogenide is a chemical composite consisting of at least one chalcogen anion and at least one more electropositive element. The term is usually reserved for sulfides, selenides, and tellurides. Metal Chalcogenides are referred to as the combination of metal and chalcogen atoms. However, transition metal atoms are generally more favorable to bind with chalcogens to form metal chalcogenides. The bonding between the transition metal and chalcogens shows characteristics in between that of ionic and covalent characters. Apart from their rich redox properties, metal chalcogenides are found helpful in many recent applications. Metal Chalcogenides are a rich source of Nonlinear Optical Materials.[18] Transition Metal Chalcogenides can form ultrathin inorganic materials with tunable electronic properties, which find applications in spintronics, straintronics, and valleytronics.[19]
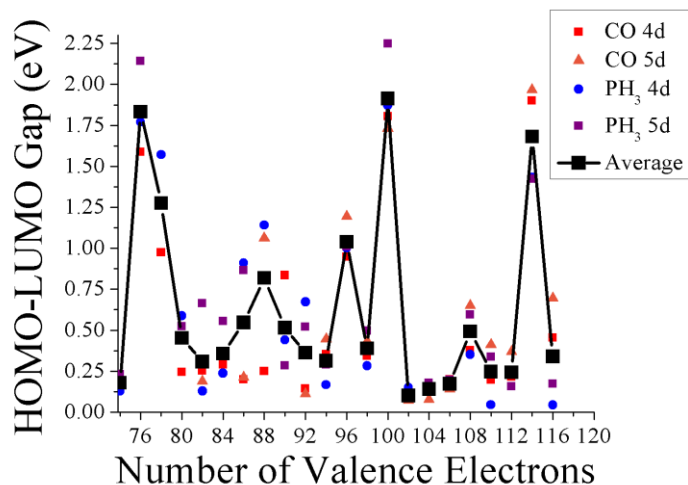
Figure 1.8 The HOMO-LUMO gap of the $M_6Se_8L_6$ clusters, with L=CO, and PH_3, and M=Y-Pd, and La, Hf-Pt. For CO ligated clusters, charge states of +2, 0, and -2 were studied, while for PH_3 ligated cluster charge states of +4, +2 and 0 are shown.

Furthermore, ligated metal chalcogenides are extremely rich in redox behaviors. With phosphine ligands, they can act as a superalkali with ionization energy as low as 3.11 eV for $Re_6Se_8(PMe_3)_6$ cluster lower than Cs atom (3.89 eV). Furthermore, with moderate acceptor ligands like CO, these clusters can act as a super halogen with electron affinity as high as a 3.76 eV for $Mo_6Se_8(CO)_6$ cluster comparable with Cl atom (3.612 eV).

As we know that the critical criteria for a cluster to be considered a superatom is that the cluster has a well-defined valence. Bonding in metal-chalcogenide clusters is a mixture of covalent bonding between the metal and chalcogen and bonding and charge transfer complexes between the metal and ligand. For this reason, a nearly free electron gas cannot determine the electronic counts leading to stable species. The analysis of the electronic structure of metal-chalcogen clusters hinted that these clusters have periodic closed electronic shells that can classify them as superatoms with well-defined valence. In principle, these clusters can be stabilized via two paradigms, the oxidation state of the metal atoms within the cluster may form a closed electronic shell or a shell of delocalized bonding orbitals over the entire symmetric cluster may lead to a large HOMO-LUMO gap and corresponding stability associated with a closed electronic shell. Stabilization may also occur via mixed-valence or Jahn-Teller distortion, resulting in symmetry breaking, and the cluster will no longer remain octahedral. Khanna et al. have thoroughly studied many octahedral metal chalcogenide clusters of the form, $M_6Se_8L_6$ (M = 4d and 5d transition metals including Y-Pd, and La, Hf-Pt, & L = CO/ PH$_3$). For the electron counting, all of the valence s and d electrons of the transition metal, 6 valence electrons from the Se, and 2 electrons per CO and PH$_3$ ligand are considered. Figure 1.8 shows periodic electron counts with large HOMO-LUMO gaps that correspond to 76, 96, 100, and 114 valence electrons, with secondary peaks at 78 and 88 valence electrons for the 4d and 5d transition metal series in different ligand environments (CO/PH$_3$).

Octahedral $M_6X_8L_6$ clusters with 76 valence electrons are stable due to the local oxidation state of the atoms. The second mode of stabilization is through the filling of closely packed states that have the same–energy due to the high octahedral symmetry of the cluster, or similar energies due to coincidental degeneracy. Examples of electron counts with such large HOMO-LUMO gaps include 96, 100, and 114 valence electrons. The peak at 88 valence electrons is due to a Jahn-Teller distortion that breaks the symmetry and leads to the different metal atoms having different charge states. On the other hand, the electron counts of 76, 78, 96, 100, and 114 have O_h symmetry. This result demonstrates that there are electron counts in metal-chalcogen clusters that correspond to enhanced electronic stability.

d) Cluster Assembled Material (CAM): An important class of clusters that have drawn tremendous attention in recent years is based on ligated metal-chalcogenide clusters. These clusters can form solids when combined with counterions. Some of the initially reported clusters include $Co_6Se_8(PEt_3)_6$, $Cr_6Te_8(PEt_3)_6$, $Ni_9Te_6(PEt_3)_8$, $Ni_6Se_5(PR_3)_8$, $Co_6Te_8(PR_3)_6$, $Ni_9Te_6(CO)_8$, $Co_{11}Te_7(CO)_{10}$, and $Co_9Te_6(CO)_8$.[3,20,21] The ligated clusters consist of a central core of transition metals and chalcogens and are stabilized by ligands such as phosphines, CO, or other ligands. These interesting classes of superatoms are found to be highly stable and can be independently prepared in solutions. Further, the ligands offer an additional pathway to tuning the properties of a cluster, either through stabilizing a closed electronic shell, inducing active sites, or controlling the donor-acceptor characteristics. Further, depending on the ligand, they can have charge donor/acceptor characteristics that allow them to form a variety of solids when combined with complementary ions, including C_{60}, $FeCl_4$, and other clusters with high electron affinity, maintaining the identity of the metal-chalcogenide core.
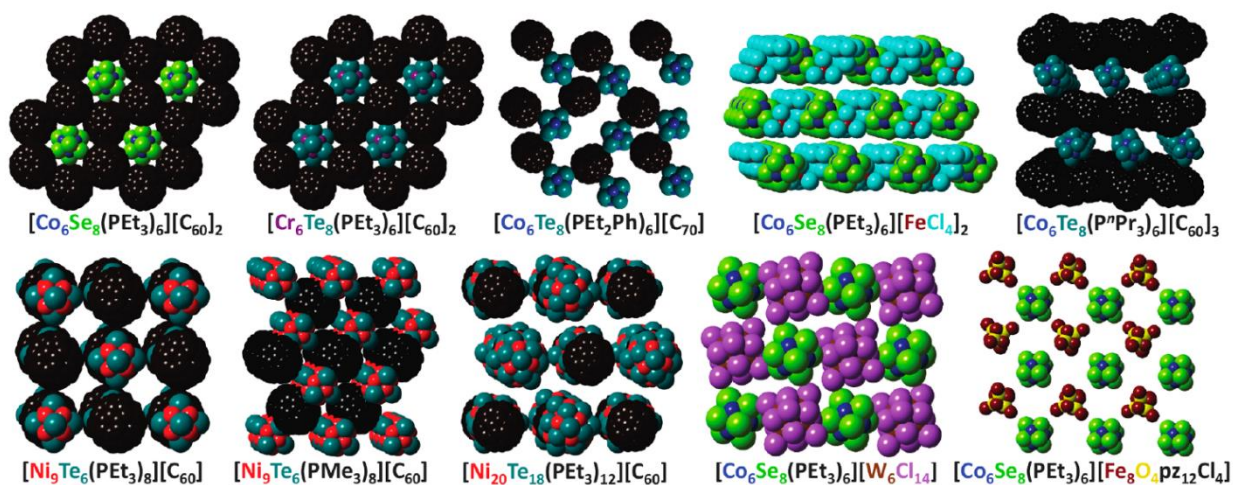
Figure 1.9 Library of SACs self-assembled using complementary charge transfer between superatomic building blocks. Supporting ligands have been omitted for clarity. *(Reused With Permission, Copyright American Chemical Society)*[3]

The primary goal of synthesizing stable atomic clusters and superatomic clusters is to form cluster assembled materials with tailored properties. The clusters and ligand-protected clusters may be used to form CAMs from bottom-up technique, with flexibility in tailoring electronic, magnetic, optoelectronic properties in the material with precision and control. The clusters stabilized by ligands can not only be assembled from wet chemical synthesis but can also be deposited on supports to form CAMs. Figure 1.9 shows some of the solids formed through cluster assembly using metal-chalcogenide clusters.[3]

d) Ligands:

A neutral molecule or ions bound to a metal site is called a ligand. In other words, any functional group that binds strongly to a metal center can be considered a ligand. Ligands are tremendously important in the synthesis of metallic and semiconducting nanoparticles. They can act as a structure-directing agent for the synthesis of nanoparticles.[10] They can also change the

13

solubility of the reagents during synthesis. Ligands are also used for functionalization and protect the surface of the particle from reactions.[11] Moreover, ligands are found to alter the redox properties of the metal clusters. They stabilize the cluster by shifting HOMO levels and can also modulate the magnetic moment of the system.[13,22,23] The stability of clusters in the wet phase can be explained based on the ligand effects. Apart from stabilization, the ligands can also alter the redox properties of the clusters.[22] The shape and size of the ligands play significant roles in cluster assembly and the electron conduction pathway through the cluster assembled material. Figure 1.10 shows the ligands stabilized clusters using phosphines, carbonyl (CO), cyanide (CN), thiols, etc. ligands.

Phosphines	Carbonyl	Cyanide	Thiols	Halides
$Co_6Se_8(PR_3)_6$	$Mo_6Te_8(CO)_6$	$Fe_6S_8(CN)_6^{-5}$	$Au_{18}(SR)_{18}^{-}$	$Au_{13}Cl_2(PR_3)_{10}^{+3}$
Gap = 1.24 eV	Gap = 0.84 eV	Gap = 0.85 eV	Gap = 1.09 eV	Gap = 1.84 eV
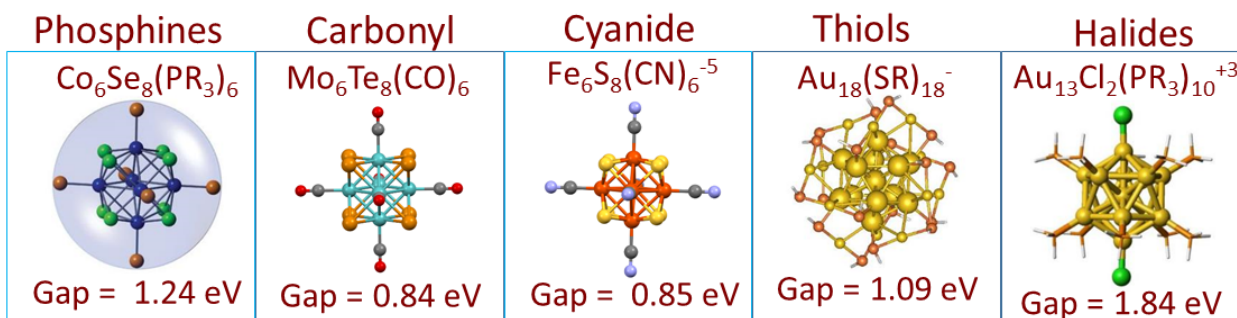
Figure 1.10 Metal chalcogenide and gold clusters stabilized in different ligand environments.

1.2. Motivations

a) Experimental work

More recently, Xavier Roy et al. have successfully assembled different superatomic solids. New classes of materials termed superatomic crystals (SACs) are synthesized through cluster assembly using molecular clusters as superatomic building blocks.[3] Equipped with a rich library of molecular clusters with exciting properties such as diverse functionalization, redox activity, and magnetic ordering, SAC with high tunability, atomic precision, and robust architectures were created.[3,20] Their work has the following four facets:

14

(1) Design and synthesis of molecular cluster superatomic building blocks

(2) self-assembly into SACs (formation of solids)

(3) Study of the resulting collective properties of SACs.

(4) Finding potential applications of SACs

The cluster cores comprise octahedral [M_6E_8] and cubane [M_4E_4] (M = metal; E = chalcogen), which are typically passivated by a shell of supporting ligands, that can also help in direct solid-state assembly. They have designed whole families of binary SACs where the building blocks are held together through electrostatic, covalent, or van der Waals interactions, as shown in Figure 1.11. The blend of atomic precision and intercluster interactions in these SACs generates unique collective properties involving tunable electron transport, crystalline thermal conductivity, and ferromagnetic characteristics. Additionally, they have created a synthetic approach to incorporate redox-active guests into the superstructure of SACs through single-crystal to single-crystal intercalation. This process allows the tuning of the optical and electrical transport properties of the superatomic crystal host. Using a host of techniques, SCXRD, Raman spectroscopy, SQUID magnetometry, electrical transport measurements, electronic absorption spectroscopy, differential scanning calorimetry, and frequency-domain thermoreflectance, the investigation of collective properties of superatomic crystals are achieved. The ability to exactly modulate the structure and properties of nanoscale building blocks is key in developing the next generation of functional materials. The bottom-up assembly of preformed molecular clusters toward well-defined hierarchical materials has proven to be a successful approach in designing new functional materials. These materials exhibit collective physical properties that emerge because of their atomic precision. Their extensive work in modifying the building blocks with functional ligands

has been successful. Additionally, they are exploring a new dimension to employ molecular clusters in various applications.
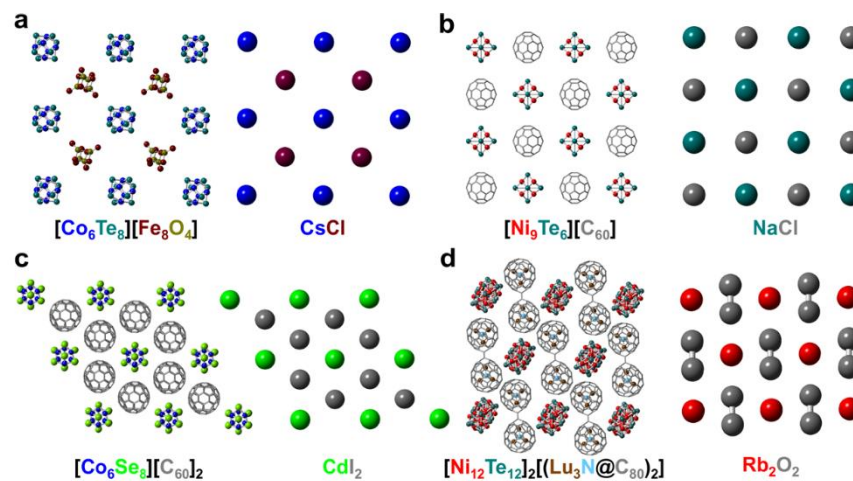
Figure 1.11 The Selected SACs and their atomic structural analogues. Supporting ligands in all of the SACs have been removed for clarity. (a)$[Co_6Te_8(PEt_3)_6][Fe_8O_4pz_{12}C_{14}]$ and CsCl; (b) $[Ni_9Te_6(PEt_3)_8][C_{60}]$ and NaCl; (c) $[Co_6Se_8(PEt_3)_6][C_{60}]_2$ and CdI$_2$; (d) $[Ni_{12}Te_{12}(PEt_3)_8]_2[(Lu_3N@C_{80})_2]$ and Rb$_2$O$_2$. *(Reused With Permission, Copyright American Chemical Society)*[3]

For example, $Co_6Te_8(PEt_3)_6$ clusters have been used as dopants for 2D semiconductors by Yu. et al.[24] These experimental findings and the theoretical works on metal-chalcogenide clusters from our lab, which are discussed below, have inspired my research towards metal-chalcogenide clusters and their cluster assembly.

b) Theoretical Work

Our group has been working with octahedral ligated metal chalcogenides for the past few years. Inspired by the experimental synthesis of cluster assembled materials,[3,20] our group has worked independently and in collaboration with experimental groups to investigate the ligand effects on the electronic and magnetic properties of the metal chalcogenide clusters in different ligand

16

environments. Our group was also the first one to propose the design of magnetic superatom. A few exciting works related to ligand effects on metal chalcogenides clusters and the magnetic superatom has been listed below:

(i) Tuning the properties of metal-chalcogenide clusters using different ligand environments.

Vikas Chauhan et al. showed that the metal-chalcogenide cluster might transform from an electron donor to an electron acceptor through the ligand exchange.[25] Using the first-principles calculations, they showed that when phosphines (PEt$_3$) ligands are exchanged by CO (Carbonyl) ligands, the electronic properties of cluster Co$_6$Te$_8$ are significantly changed while the magnetic character stays the same. Co$_6$Te$_8$(PEt$_3$)$_6$ is a closed electronic shell with small ionization energy of 4.74 eV, comparable with alkali atoms. Upon successive replacement of PEt$_3$ ligands by CO ligand, Co$_6$Te$_8$(CO)$_6$ is formed, exhibiting halogen-like behavior with high electron affinity, as shown in Figure 1.12. Co$_6$Te$_8$(PEt$_3$)$_6$ and Co$_6$Te$_8$(CO)$_6$ both have closed electronic shells marked by high HOMO-LUMO gaps of 1.24 eV and 1.39 eV, respectively. With these two different ligands, only the polarity of interaction between Co 4s orbital and the lone pair of ligands change, while the effective valence count remains intact.
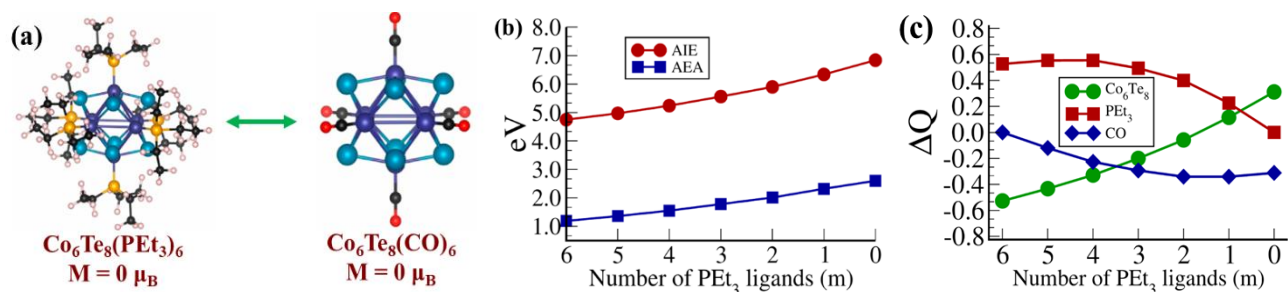
Figure 1.12 (a) Successive replacement of PEt$_3$ ligand by CO ligand (b) IP and EA with subsequent replacement of PEt$_3$ ligands by CO ligands. (c) The plot of total charge with the subsequent exchange of PEt$_3$ ligands by CO ligands. *(Reused With Permission, Copyright American Chemical Society)*[25]

The change in the electronic character is associated with the shift in the electronic spectrum that can be explained as ligands forming Coulomb well that surrounds the cluster and may raise or lower the energy states depending on the donor-acceptor ligand characteristics.

(ii) Inducing super-alkali character of Ni_9Te_6 cluster upon ligation with PEt_3 ligands.

The choice of ligand controls the donor/acceptor properties of ligand protected clusters with closed electronic shells.[26] A bare cluster of Ni_9Te_8 has an ionization energy of 5.88 eV, which upon ligation with PEt_3 ligands, reduces to 3.36 eV lower than the IP of the Cesium atom (3.89 eV). For a completely ligated clusters, the ligands shift the HOMO levels of the system by 1.98 eV. The rearrangement of charges due to the ligands shifts the electronic spectrum. The transfer of charge from a super-alkali metal-chalcogenide cluster ($Ni_9Te_6(PEt_3)_8$) to acceptor counterion C_{60} stabilizes the ionic solid [$Ni_9Te_8(PEt_3)_8.C_{60}$] as shown in Figure 1.13. Ligands can modulate the electronic and magnetic properties of the ligand-protected clusters.
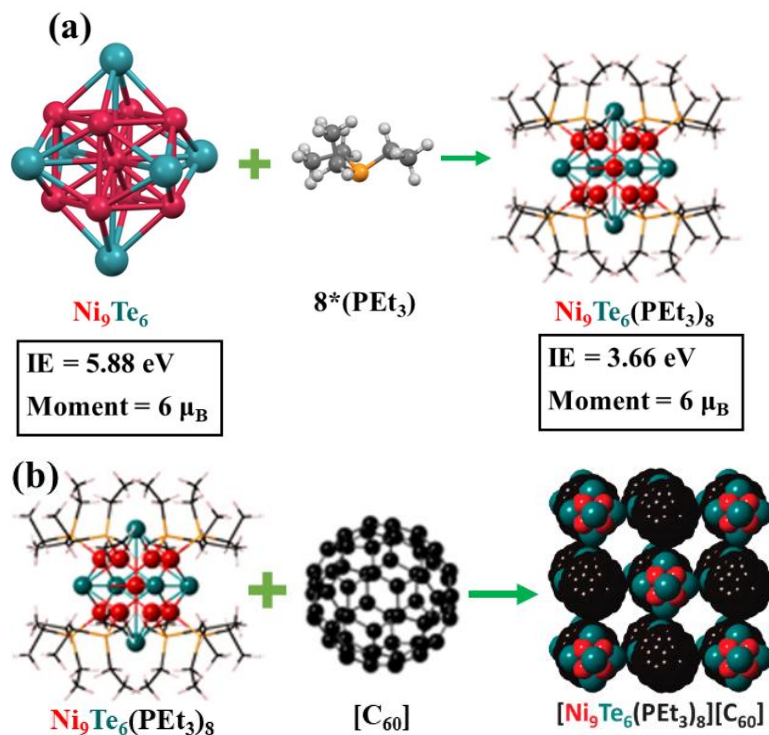
Figure 1.13 (a) IE drop on PEt_3 ligation (b) Schematic of formation of ionic solid $Ni_9Te_6(PEt_3)_8.C_{60}$.

(iii) Modulation of the magnetic moment of Ni$_9$Te$_6$ clusters ligated with CO/phosphines.[13]

When a single ligand is detached from a fully ligated magnetic cluster, Ni$_9$Te$_6$(CO)$_8$[6 μ_B], the magnetic moment is completely quenched, as seen in Fig 1.14. The role of ligand in changing the magnetic moment has been explained as the tussle between Hund's rule and Jahn-Teller distortion for the stability of the cluster. This research concludes that the geometrical structure of the cluster dictates the stabilization of the magnetic state. When the cluster is symmetric, as in bare and fully ligated clusters, the geometric symmetry leads to the degenerate energy states closer to the HOMO. Thus, it follows Hund's rule and attains high spin multiplicity breaking the spin symmetry. However, when there is distortion in geometry, as in the cases with one or seven ligands, Jahn-Teller distortion breaks the spatial symmetry, thereby quenching the magnetic moment maintaining the spin symmetry.
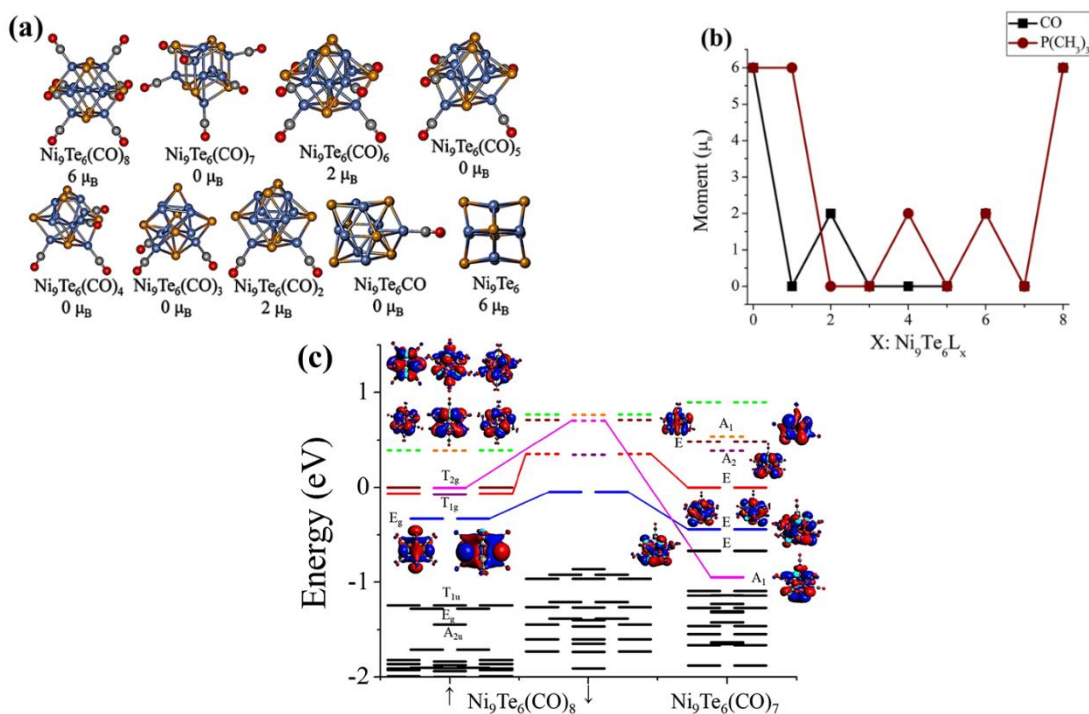
Figure 1.14 (a) ground state structures of Ni$_9$Te$_6$(CO)$_n$ (n=8-0) (b) modulation of magnetic moments with CO and PR$_3$ ligands (c) A molecular orbital diagram of Ni$_9$Te$_6$(CO)$_8$ and Ni$_9$Te$_6$(CO)$_7$. HOMO corresponds to 0 eV. (*Reused with Permission, Copyright JCP*)[13]

19

c) Experimental Collaboration

Our group has successfully collaborated with the experimental group to verify the change in electronic characteristics of ligated metal chalcogenide clusters through ligand substitution. In one of our recent collaborations with experimental groups from Johns Hopkins University and Columbia University, the theoretical predictions confirmed the raising of the electronic spectrum when donor PEt_3 ligands are attached to the Co_6Se_8 cluster core.[27] In contrast, the lowering of the spectrum was observed upon the addition of acceptor CO ligands. A specialized infrared desorption/laser photoemission (IR/PE) supersonic helium expansion source is employed to make the parent anions $Co_6S_8(PEt_3)_{6-x}(CO)_x^-$ in the gas phase. The electronic structure and electron affinity (EA) of a series of cobalt sulfide clusters, whose ligand shells consist of differing combinations of PEt_3 and CO ligands, were probed using the anion photoelectron spectroscopy. The parent cluster $Co_6S_8(PEt_3)_6$ gives $Co_6S_8(PEt_3)_{6-x}(CO)_x$ cluster by ligand substitution with CO.
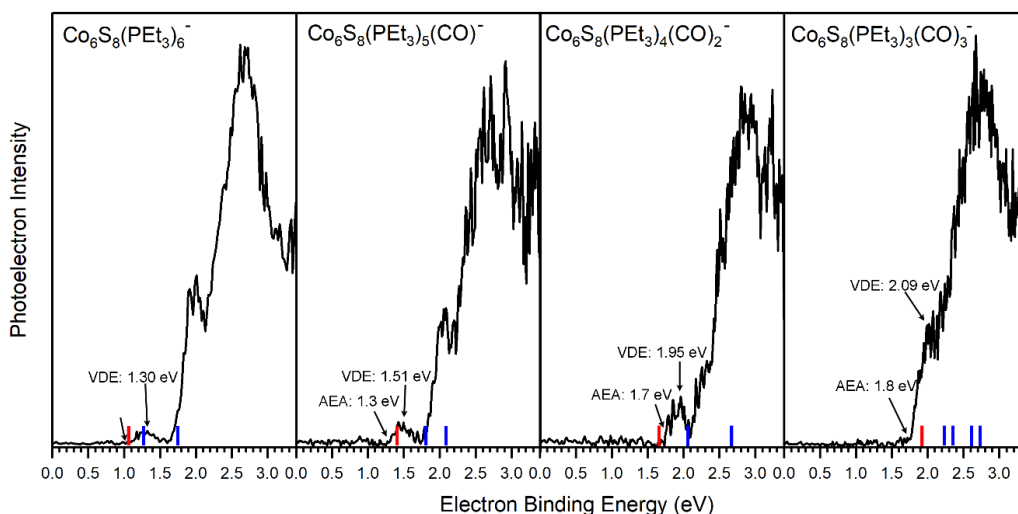
Figure 1.15 Negative ion photoelectron spectra of $Co_6S_8(PEt_3)_{6-x}(CO)_x^-$ (x = 0–3) anions collected using 355 nm (3.49 eV) photons from a Nd:YAG laser. The arrows point to the experimental values of AEA and VDE; the red lines correspond to theoretical AEA, and the blue lines correspond to vertical transitions from the anion to the singlet and triplet neutral states. (Reproduced With Permission)[27]

Mass spectrometry then bolsters the existence of carbonylated products with x up to 3 (i.e., $Co_6S_8(PEt_3)_5(CO)^-$, $Co_6S_8(PEt_3)_4(CO)_2^-$, and $Co_6S_8(PEt_3)_3(CO)_3^-$). The experimental results revealed that the electron affinity and vertical detachment energy increase with the number of CO ligands, demonstrating the electronic spectral tunability of this group of superatoms. Figure 1.15 presents the anion photoelectron spectra of $Co_6S_8(PEt_3)_{6-x}(CO)_x^-$ (x = 0–3) from which the adiabatic electron affinity (AEA) and vertical detachment energy (VDE) of each cluster were determined. The value of the AEA is taken to be the onset of the lowest electron binding energy (EBE) peak in the photoelectron spectrum. The VDE is the vertical transition energy from the ground state of the anion to the neutral state at the anion geometry. It is determined as the EBE value at the intensity maximum of the peak of interest, i.e., typically the first EBE peak. Based on the anion photoelectron spectra, the AEA values of $Co_6S_8(PEt_3)_{6-x}(CO)_x$ are 1.1, 1.3, 1.7 and 1.8 eV for x = 0, 1, 2, 3, respectively, while the corresponding anion VDE values are 1.30, 1.51, 1.95 and 2.09 eV, respectively. By sequentially swapping half of the PEt_3 ligands with CO ligands, the AEA of this superatom increases from 1.1 eV to 1.8 eV, meanwhile maintaining the same oxidation state for the Co_6S_8 core. Hence, the observed variation in AEA for the ligated superatoms, preserving the oxidation state of the Co_6S_8 core across the ligation series, underlined the remarkable characteristics of the superatoms. Henceforth, the unequivocal tendency of increase in AEA and VDE with ligand substitution provides direct evidence that the effective tuning of electronic properties of superatom is viable through the ligand substitution.

(d) Magnetic Superatom:

The existing idea of superatoms hinges on acquiring stability through closed electronic shells of paired electrons. Consequently, it is restricted to non-magnetic species because magnetism

requires unpaired species. However, intriguing hypotheses were proposed for designing the magnetic superatom.[28] The first one proposed by Khanna et al. stated that magnetic superatoms could be attained if the stability is achieved through delocalized electrons while the magnetic character is incorporated through the localized electronic states.
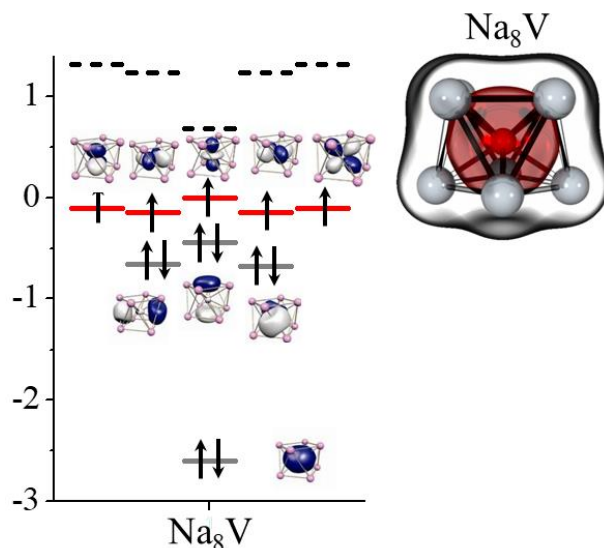
Figure 1.16. Schematic showing electronic states in Na_8V cluster. (Reproduced With Permission)[28]

It is successfully showed that by doping the Vanadium atom in the Sodium cluster (Na_8V), with 13 valence electrons, as shown in Fig 1.16. 8 valence electrons were related to the delocalized shells filling $1S^2$, $1P^6$ while the remaining 5 valence electrons remained localized, half filling the $3d^5$ orbitals, thereby inducing 5 μ_B of magnetic moment in the Na_8V cluster.

References

1 S. N. Khanna and P. Jena, *Phys. Rev. B*, 1995, **51**, 13705–13716.

2 P. Jena and Q. Sun, *Chem. Rev.*, 2018, **118**, 5755–5870.

3 A. Pinkard, A. M. Champsaur and X. Roy, *Acc. Chem. Res.*, 2018, **51**, 919–929.

4 B. V. Reddy, S. K. Nayak, S. N. Khanna, B. K. Rao and P. Jena, *Phys. Rev. B*, 1999, **59**, 5214–5222.

5 R. E. Leuchtner, A. C. Harms and A. W. Castleman, *J. Chem. Phys.*, 1989, **91**, 2753–2754.

6 S. N. Khanna and P. Jena, *Phys. Rev. Lett.*, 1992, **69**, 1664–1667.

7 P. J. Roach, W. H. Woodward, A. W. Castleman, A. C. Reber and S. N. Khanna, *Science*, 2009, **323**, 492–495.

8 A. C. Reber, S. N. Khanna, P. J. Roach, W. H. Woodward and A. W. Castleman, *J. Am. Chem. Soc.*, 2007, **129**, 16098–16101.

9 W. D. Knight, K. Clemenger, W. A. de Heer, W. A. Saunders, M. Y. Chou and M. L. Cohen, *Phys. Rev. Lett.*, 1984, **52**, 2141–2143.

10 D. E. Bergeron, *Science*, 2005, **307**, 231–235.

11 A. C. Reber and S. N. Khanna, *Acc. Chem. Res.*, 2017, **50**, 255–263.

12 A. C. Reber, S. N. Khanna and A. W. Castleman, *J. Am. Chem. Soc.*, 2007, **129**, 10189–10194.

13 A. C. Reber, V. Chauhan and S. N. Khanna, *J. Chem. Phys.*, 2017, **146**, 024302.

14 A. J. Welch, *Chem. Commun.*, 2013, **49**, 3615.

15 H. R. Banjade, Deepika, S. Giri, S. Sinha, H. Fang and P. Jena, *J. Phys. Chem. A*, 2021, acs.jpca.1c02817.

16 I. M. L. Billas, A. Chatelain and W. A. de Heer, *Science*, 1994, **265**, 1682–1684.

17 I. I. Moiseev, T. A. Stromnova and M. N. Vargaftik, *J. Mol. Catal.*, 1994, **86**, 71–94.

18 I. Chung and M. G. Kanatzidis, *Chem. Mater.*, 2014, **26**, 849–869.

19 T. Heine, *Acc. Chem. Res.*, 2015, **48**, 65–72.

20 X. Roy, C.-H. Lee, A. C. Crowther, C. L. Schenck, T. Besara, R. A. Lalancette, T. Siegrist, P. W. Stephens, L. E. Brus and P. Kim, *Science*, 2013, **341**, 157–160.

21 E. A. Doud, A. Voevodin, T. J. Hochuli, A. M. Champsaur, C. Nuckolls and X. Roy, *Nat. Rev. Mater.*, 2020, **5**, 371–387.

22 A. C. Reber, D. Bista, V. Chauhan and S. N. Khanna, *J. Phys. Chem. C*, 2019, **123**, 8983–8989.

23 V. Chauhan, A. C. Reber and S. N. Khanna, *Nat. Commun.*, 2018, **9**, 1–7.

24 J. Yu, C.-H. Lee, D. Bouilly, M. Han, P. Kim, M. L. Steigerwald, X. Roy and C. Nuckolls, *Nano Lett.*, 2016, **16**, 3385–3389.

25 V. Chauhan, A. C. Reber and S. N. Khanna, *J. Am. Chem. Soc.*, 2017, **139**, 1871–1877.

26 V. Chauhan, S. Sahoo and S. N. Khanna, *J. Am. Chem. Soc.*, 2016, **138**, 1916–1921.

27 G. Liu, V. Chauhan, A. P. Aydt, S. M. Ciborowski, A. Pinkard, Z. Zhu, X. Roy, S. N. Khanna and K. H. Bowen, *J. Phys. Chem. C*, 2019, **123**, 25121–25127.

28 J. U. Reveles, P. A. Clayborne, A. C. Reber, S. N. Khanna, K. Pradhan, P. Sen and M. R. Pederson, *Nat. Chem.*, 2009, **1**, 310–315.

Chapter 2

Density Functional Theory and Computational Methods

Introduction and Background

The density functional theory (DFT) has developed the essential computational tool for theoretical and experimental scientists working in diverse fields such as physics, chemistry, materials science, biology, nanoscience, and nanotechnology. DFT has made it possible to perform complicated calculations precisely for many systems within a limited timeframe. Besides, among many others, DFT has been successful in predicting new 2D materials, their properties,[1,2] and applications.[3] Briefly stating, DFT can predict new materials and their properties, thereby helping experimentalist to identify best material of their interest from thousands of materials before they start the synthesis of materials experimentally. This, in turn, reduces the experimental time and cost significantly.

2.1 Background:

The development of quantum mechanics in early 20th century made it possible to understand the microscopic properties of the systems. Besides, it helped to understand the underlying physics behind many fundamental phenomena. Thanks to quantum mechanics and the most famous Schrodinger wave equation (SWE), which makes it possible to explain the microscopic systems. SWE in its simplest form can be represented by equation 2.1.

$$\widehat{H}\psi = E\psi \qquad (2.1)$$

Where, $\widehat{H}$ is the Hamiltonian operator, "E" is the corresponding energy eigenvalue, and ψ represents the wavefunction of the total system containing all the information that can be extracted out for a given system. The expanded form of the Hamiltonian Operator $\widehat{H}$ is given by equation (2.2).

$$\hat{H} = -\frac{1}{2}\sum_{i=1}^{N}\Delta_i^2 - \frac{1}{2}\sum_{A=1}^{M}\frac{\Delta_A^2}{M_A} - \sum_{i=1}^{N}\sum_{A=1}^{M}\frac{Z_A}{r_{iA}} + \sum_{i=1}^{N}\sum_{j>i}^{N}\frac{1}{r_{ij}} + \sum_{A=1}^{M}\sum_{B>A}^{M}\frac{Z_A Z_B}{R_{AB}} \quad \text{------- (2.2)}$$

The Hamiltonian operator ($\hat{H}$) is the sum total of the kinetic energy of electrons and nuclei, electron-nuclei, and electron-electron interactions. The solution of Eq. 2.1. provides an abundance of information that can be useful for physicists, chemists, and material scientists. However, SWE can be solved precisely only for hydrogen-like systems. The equation possesses intrinsic difficulties due to electron-electron interactions present in the system with many electrons.. Hence, solving the many-body Schrödinger equation is probably the most substantial challenge in quantum mechanics. Many wavefunction theories have been developed to incorporate the exchange and correlations of the system for the optimum possible representations. Hartree-Fock's[4] method is a mean-field theory that includes the exchange interaction but unable to contain the correlation. Then Post-Hartree-Fock methods such as CCSD, CI, etc., can encompass the correlation effect; however, the computational cost increases with the number of electrons making their usage impractical for the solids and sizeable molecules.

The wave function has no physical significance as it is not "observable". However, the square of a wave function is directly related to the probability density of electrons. The electron density is observable and can be gauged by fitting experiments such as x-ray diffractions. Hence, using electron density seemed more straightforward and rational. Utilizing electron density as the fundamental parameter of a quantum mechanical system has always been a tempting topic to theoretical chemists because of the following two reasons:

1) Unlike the wave function, the electron density of a quantum mechanical system is an experimentally quantifiable quantity.

2) Compared with the 4N number of variables (3N+ N for the coordinates and the spin) in wave-function formulation, electron density depends only on 3 Cartesian coordinates. Thus, using electron density is computationally cheaper and can also be realized more directly than the wavefunction-based approach. Thomas and Fermi proposed the first simplest approximation of utilizing electron density in the early 1930s, famously known as the Thomas–Fermi(TM) model.[5,6] This model successfully described the total energy of atoms qualitatively; however, due to its complete negligence of exchange and correlation effects, its results do not fit most chemistry and material science.[7] However, the true significance of this model is not due to the accuracy of the method. Still, it provided the first glimpse of the possibility of using electron density as the fundamental variable. DFT is an alternative approach in which the electron density replaces the wave function. The fundamental concepts of quantum chemistry, starting from the evolution of the Schrodinger equation to the Kohn-Sham method, are discussed briefly below.

The Schrodinger equation for an N-electron system using the Born-Oppenheimer approximation is given by equation 2.3,

$$[\sum_{i=1}^{N} \frac{\nabla_i^2}{2} + \sum_{i=1}^{N} V_{ext}(r) + \sum_{i=1}^{N} \sum_{j>i}^{N} V_{ee}(r)]\psi = E\psi \ldots\ldots(2.3)$$

ψ represents the N-electron wavefunction. The first term on the left-hand side of equation (2.3) (inside the square bracket) is the kinetic energy. The second and the third terms are the nucleus-electron interaction and the repulsive electron-electron interaction potentials, respectively. One can solve equation 2.3 using Kohn-Sham equations, which utilize localized and plane-wave basis

sets. The two theorems by Hohenberg and Kohn[8] and the Kohn-Sham method laid the foundation

of the density functional theory, which are briefly summarized below

2.2 (i) First Hohenberg-Kohn theorem

It states that the ground-state electron density $\rho(r)$ of an electronic system distinctively determines

an external potential (V_{ext}) acting on the electrons up to an additive constant. This theorem creates

a one-to-one correspondence between the ground-state electron density and the external potential.

The ground-state electron density determines the total number of electrons(N) of the system.

Hence $\rho(r)$ uniquely determines the Hamiltonian through N and V_{ext}.

(ii) Second Hohenberg-Kohn theorem

The ground state wavefunction and all the ground state properties like kinetic and potential

energies can be distinctively determined by the ground-state electron density $\rho(r)$. Thus, for an

external potential (V_{ext}), the total energy becomes a functional of $\rho(r)$ as follows:

$E[\rho] = T[\rho] + V_{ee}[\rho] + \int \rho(r)V_{ext}\, dr = F_{HK}[\rho] + \int \rho(r)V_{ext}\, dr$ -----------(2.4)

Where, $F_{HK}[\rho]=T[\rho] + V_{ee}[\rho]$ is dubbed the Hohenberg-Kohn functional, specified for the ground

state of an N-electron system. Additionally, it is independent of the external potential (V_{ext}) and is

also known as a universal functional of $\rho(r)$. $T[\rho]$ and $V_{ee}[\rho]$ are the kinetic energy functional and

electron-electron interaction functionals, respectively. The second theorem offers a variational

principle for $E[\rho]$, considering $\rho(r)$ as the primary variable.

(iii) Kohn Sham Method:

Despite offering possibilities of calculating ground state properties via the ground-state electron

density $\rho(r)$, Hohenberg-Kohn theorems lack a computational method to calculate $\rho(r)$ as the

28

functional form of F_{HK} is undetermined. Later, Kohn and Sham provided formalism with a set of equations known as the Kohn-Sham equations, which are solved self-consistently to find $\rho(r)$ that minimizes $E[\rho]$. For a given N-electron interacting system, Kohn and Sham assumed the existence of a non-interacting reference system, with an imposed constraint that the fictitious reference system must have the same electron density $\rho(r)$ in the ground state as the interacting system of curiosity.[9] For such a non-interacting N-electron system, the Hamiltonian of the system can be expressed as the sum of single-electron Hamiltonians. The kinetic energy $T_{KS}[\rho]$ can also be calculated exactly; however, this kinetic energy is not equal to the kinetic energy of the interacting system. Hence, they expressed the $E[\rho]$ as

$$E[\rho] = T_{KS}[\rho] + J[\rho] + E_{xc}[\rho] + \int \rho(r)V_{ext}\, dr \text{ -----------------(2.5)}$$

where, $J[\rho]$ is the classical electron-electron repulsion energy and $E_{xc}[\rho]$ is exchange-correlation functional defined as,

$$E_{xc}[\rho] = T[\rho] - T_{KS}[\rho] + V_{ee}[\rho] - J[\rho\ ]$$

$$E_{xc}[\rho] = \Delta T[\rho] + \Delta J[\rho\ ] \text{ --(2.6)}$$

The first term offers the difference between the kinetic energies of real (interacting) and non-interacting systems. In contrast, the second term provides the non-classical part, which includes the Coulomb repulsion and interaction energy. Hence, the interacting N-electron system in V_{ext} potential can be mapped to the non-interacting electrons in an effective potential of $V_{eff}(r)$. Consequently, a set of the N single-electron equations is given by,

$$[\frac{\Delta_i^2}{2} + V_{eff}(r)]\psi_i = \varepsilon_i\psi_i \quad \text{--------------(2.7)}$$

These N single-electron equations are knowns as Kohn-Sham equations. The ground-state electron density and Kohn-Sham orbitals are related by

$$\rho\,(r) = \sum_{i=1}^{N} |\psi_i(r)|^2 \text{-----------------(2.8)}$$
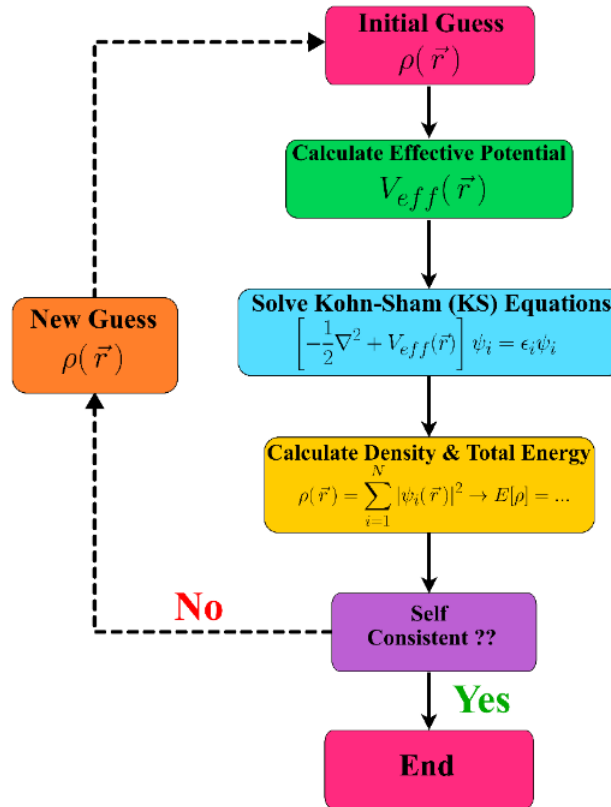
Figure 2.1 Schematic of self consistent calculation (SCF) using Kohn-Sham formalism.

We start with some trial charge density and generate effective potential $V_{eff}(r)$. Then we solve the Kohn-Sham equation 2.7 iteratively to total energy $E[\rho]$ and density $\rho(r)$ of the system. This process repeats until the output charge density is the same as the input charge density, or the system's energy does not alter any longer, as shown in Figure 2.1.

2.3 Exchange-Correlation Energy

The exchange-correlation potential is an exciting and essential piece lacking its exact form in general. Although the complexity of the quantum many-body interactions (that are contained in the exchange-correlation energy) is unknown, several suitable approximations can be made. The most successful way to estimate the exchange-correlation energy is the constraint search method that uses the exact mathematical conditions, universal, assured by the exchange and correlation energies. The approximations to E_{xc} can be exquisitely categorized into Jacob's ladder[10] as defined by J. Perdew. As one rises the ladder, the complexity of the approximation and its accuracy increases, and the computational cost.

(i) Local Density Approximation (LDA)

The local density approximation LDA is the simplest but equally successful approximation for The exchange-correlation energy. LDA assumes that the energy depends on the electron density at every point in space. The key ingredient of this approximation is the uniform electron gas. The exchange-correlation energy per particle of a uniform electron gas of density (ρ) can be disintegrated into an exchange and a correlation part

$$E_{xc}[\rho] = E_x[\rho] + E_c[\rho]$$

The exchange part $E_x[\rho]$ is the exchange energy of an electron in a uniform electron gas of particular density and is known precisely. The correlation energy can also be obtained numerically up to two or three significant figures at selected values of the density[11] and later fitted for all densities.[12] The LDA successfully defines slowly varying electronic density, like bulk metals. Besides, LDA has also accomplished forecasting various materials properties such as structures, vibrational frequencies, elastic moduli, etc., of an appropriate system. Nevertheless, it underrates the binding energy of several systems and somewhat fails to predict the energy barriers in the

chemical reactions. Therefore, it is not very popular in quantum chemistry. Moreover, it tends to

make less accurate predictions in the systems with dominating electron-electron interaction. Apart

from being easier to use, the triumph of LDA lies in the error cancellation between exchange and

correlation. It underestimates $E_c[\rho]$ but overestimates $E_x[\rho]$, generating fair value for $E_{xc}[\rho]$.

(ii) Generalized Gradient Approximation (GGA)

In LDA, one assumes uniform electron density; however, in practice, the electron density in any

real system tends to be spatially inhomogeneous. Hence, it is logical to consider the non-

homogeneity (i.e., the gradient) of the electron density, including uniform electron density. GGA

substantially adjusts the binding energy problems and other systematic errors such as

overestimating molecular atomization energies and bond lengths (as found with LDA). Hence, it

was broadly received by chemists during the early 1990s. Several functionals within GGA have

been developed. Some of the most successful GGA functionals are Perdew-Burke-Ernzehof

(PBE)[13] and Perdew-Wang (PW91)[12] in physics and Becke- Lee-Yang-Parr (BLYP).[14] Nowadays,

many other GGA functionals are available, and new ones are also continuously developed. In

general, the currently available GGAs can produce accurate results for main types of chemical

bonds such as covalent, ionic, and metallic. However, common GGAs and LDAs fail to define

Van der Walls interactions.[15] Hence, other more sophisticated approaches have been developed

within DFT to work with such weak interactions.

(iii) Meta-GGA functionals

The Recent development of exchange functionals has led to a more complex exchange-correlation

functional. In addition to the density and its derivatives, the new ingredient in these complex

functional is the Kohn-Sham kinetic-energy density. Some functionals which depend explicitly on

the semi-local information in the Laplacian of the spin density have been developed. These functionals are named meta-GGA functionals. Meta-GGA functionals show improvements over GGA functionals in many cases, such as atomization energies and metal surface energies, and transition pressure.[16] Furthermore, they also supplement the missing van der Walls interactions required to address the adsorption problems.[17]

(iv) Hybrid Exchange Functionals

All the approximations discussed so far are based on local (LDA) or semi-local (GGA and meta-GGA) functionals of the density. Among others, the most severe drawback of LDA and GGA is the underestimation of the band gaps of Kohn-Sham band structures. To address the band gap problem, recent developments in exchange-correlation functional introduce a non-locality in DFT by incorporating a fraction of Fock exchange with exchange-correlation energy within the GGA. The main shortcoming of this high-level functional is the computational requirement. Some of the widely adopted hybrid functionals in physics include PBE0[18,19], and the Coulomb interaction screened hybrid functional famously known as HSE (Heyd-Scuseria-Ernzehof)[19] based on the PBE exchange-correlation (Exc). In quantum chemistry, a widely used hybrid functional (B3LYP),[20] introduces mixing and other empirical considerations into its forerunner BLYP. These functionals can make substantial upgrades in calculating many material properties, such as bond lengths, atomization energies, and bang gap in solids. When the number of electrons increases, only using DFT might not suffice. Hence, applying a data-driven machine learning approach in conjunction might be key in solving such rigorous problems. Concurrently, such an approach has accomplished in predicting different parameters of materials such as bond lengths, electronic structures, crystal structures, etc.[21]

Due to the success of DFT and the development in the computational resources, every year hundreds of thousands of materials has been added in various databases such as Materials Project, OQMD, and many others. Due to these available datasets material science community has shown their interest towards data-driven approach for the material property prediction. The success of Machine learning in predicting various material properties such as band gap, formation energy, melting point, boiling point, and many others has shown its substantial presence in material science. In addition to DFT machine learning can be the alternative approach to identify the structure-property relations among many crystals.

2.4 Computational Details

The studies performed here are based on the first-principles density functional methods using the Amsterdam Density Functional (ADF) program.[22] The exchange-correlation functional proposed by Perdew, Burke, and Ernzerhof (PBE), which utilizes the generalized gradient approximation (GGA), was used.[23] The Slater type valance triple-ζ basis sets with two polarization functions (TZ2P) basis sets[24,25] were used for all the elements with a large frozen electron core. The local minimum for each structure was found using the quasi-Newton method[26] without any symmetry restrictions, and the lowest energy structures were determined for all the calculated systems. The SCF convergence criterion was set to $1e^{-8}$ Hartree, whereas the default criteria[22] were used for all optimizations. The relativistic effects were incorporated using the zero-order regular approximation (ZORA).[27] We have investigated several spin multiplicities to determine the most energetically stable ground state structure for the anionic, neutral, and cationic species. The geometric optimization and the electronic structure calculation of the periodic crystal structure were performed by the projector-augmented wave (PAW) method[28,29] as implemented in the

34

Vienna Ab-initio Simulation Package (VASP).[30,31] The dispersion-corrected density functional theory (DFT) within the generalized gradient approximation (GGA) framework proposed by Perdew, Burke, and Ernzerhof (PBE)[13] for the exchange and correlation functional is utilized for all calculations. The DFT-D3 method was utilized to include the Van der Waals corrections.[32] The Kohn–Sham orbitals were expanded using a plane-wave basis set, and the cut-off was set to 400 eV. For the VASP calculations, the crystal structure was fully optimized, and the threshold for the electronic convergence was set to 10^{-5} eV, whereas 0.01 eV $Å^{-1}$ was chosen as the criterion for ionic convergence. For catalysis, all the optimizations and transition state calculations are carried out by the hessian-based quasi-Newton approach without any symmetry constraints using the delocalized coordinates.[30,31] Frequency calculations were performed to correctly identify the transition states, and it was ensured that all the reported transition states have a single imaginary frequency of appropriate magnitude.

References

1 H. R. Banjade, J. Pan and Q. Yan, *Physical Review Materials*, 2021, **5**, 014005.

2 J. Pan, Y.-F. Zhang, J. Zhang, H. Banjade, J. Yu, L. Yu, S. Du, A. Ruzsinszky, Z. Hu and Q. Yan, *npj Computational Materials*, 2020, **6**, 1–6.

3 N. H. Attanayake, H. R. Banjade, A. C. Thenuwara, B. Anasori, Q. Yan and D. R. Strongin, *Chem. Commun.*, 2021, **57**, 1675–1678.

4 D. R. Hartree, *Math. Proc. Camb. Phil. Soc.*, 1928, **24**, 89–110.

5 R. G. Parr and W. Yang, *Density-functional theory of atoms and molecules*, Oxford Univ. Press [u.a.], New York, NY, 1. iss. as ... paperback., 1994.

6 W. Koch and M. C. Holthausen, *A chemist's guide to density functional theory*, Wiley-VCH, Weinheim, 2nd ed., 5. reprint., 2008.

7 W. Kohn, *Rev. Mod. Phys.*, 1999, **71**, 1253–1266.

8 P. Hohenberg and W. Kohn, *Phys. Rev.*, 1964, **136**, B864–B871.

9 W. Kohn and L. J. Sham, *Phys. Rev.*, 1965, **140**, A1133–A1138.

10 J. P. Perdew, in *AIP Conference Proceedings*, AIP, Antwerp (Belgium), 2001, vol. 577, pp. 1–20.

11 D. M. Ceperley and B. J. Alder, *Phys. Rev. Lett.*, 1980, **45**, 566–569.

12 J. P. Perdew and Y. Wang, *Phys. Rev. B*, 1992, **45**, 13244–13249.

13 J. P. Perdew, K. Burke and M. Ernzerhof, *Phys. Rev. Lett.*, 1996, **77**, 3865–3868.

14 A. D. Becke, *Phys. Rev. A*, 1988, **38**, 3098–3100.

15 L. J. Sham and M. Schlüter, *Phys. Rev. Lett.*, 1983, **51**, 1888–1891.

16 J. Sun, A. Ruzsinszky and J. P. Perdew, *Phys. Rev. Lett.*, 2015, **115**, 036402.

17 S. Adhikari, H. Tang, B. Neupane, A. Ruzsinszky and G. I. Csonka, *Phys. Rev. Materials*, 2020, **4**, 025005.

18 C. Adamo and V. Barone, *The Journal of Chemical Physics*, 1999, **110**, 6158–6170.

19 J. Heyd, G. E. Scuseria and M. Ernzerhof, *The Journal of Chemical Physics*, 2003, **118**, 8207–8215.

20 A. D. Becke, *The Journal of Chemical Physics*, 1993, **98**, 5648–5652.

21 H. R. Banjade, S. Hauri, S. Zhang, F. Ricci, W. Gong, G. Hautier, S. Vucetic and Q. Yan, *Sci. Adv.*, 2021, **7**, eabf1754.

22 G. te Velde, F. M. Bickelhaupt, E. J. Baerends, C. Fonseca Guerra, S. J. A. van Gisbergen, J. G. Snijders and T. Ziegler, *Journal of Computational Chemistry*, 2001, **22**, 931–967.

23 J. P. Perdew, K. Burke and M. Ernzerhof, *Phys. Rev. Lett.*, 1996, **77**, 3865–3868.

24 E. Van Lenthe and E. J. Baerends, *J. Comput. Chem.*, 2003, **24**, 1142–1156.

25 D. P. Chong, O. V. Gritsenko and E. J. Baerends, *The Journal of Chemical Physics*, 2002, **116**, 1760–1772.

26 L. Fan and T. Ziegler, *The Journal of chemical physics*, 1991, **95**, 7401–7408.

27 E. van Lenthe, J. G. Snijders and E. J. Baerends, *The Journal of Chemical Physics*, 1996, **105**, 6505–6516.

28 P. E. Blöchl, *Physical review B*, 1994, **50**, 17953.

29 G. Kresse and D. Joubert, *Physical review b*, 1999, **59**, 1758.

30 G. Kresse and J. Hafner, *Phys. Rev. B*, 1993, **47**, 558–561.

31 G. Kresse and J. Furthmüller, *Phys. Rev. B*, 1996, **54**, 11169–11186.

32 S. Grimme, S. Ehrlich and L. Goerigk, *Journal of computational chemistry*, 2011, **32**, 1456–1465.

Chapter 3

Transforming Redox Properties of Clusters Using Phosphine Ligands

Our group studied the ligand effects on the fundamental electronic properties of the metal clusters, especially metal-chalcogenide clusters, for the past few years, as briefly summarized in the previous section. Our previous studies suggested that the rise/drop in the highest occupied molecular orbital (HOMO) levels of metal-chalcogenides clusters with donor/acceptor ligands (like phosphines/CO) is responsible for the change in the electronic properties of the atomic clusters. Hence, to generalize the ligands invoked transformation in the electronic properties of atomic clusters, we investigated one of the essential electronic properties, i.e., the ionization energy (I.E.), for various classes of atomic clusters using a common ligand (phosphine). Furthermore, we want to understand the exact reason for the upward shifting of the HOMO levels and check if some other effects are also responsible for lowering the IE induced through PMe_3 ligation. Finally, we successfully expounded the physics behind such a universal trend and explained which impact is more prominent for particular cluster types.

Introduction

Organic ligands that protect the surfaces of clusters and nanoparticles against reactions and control the growth rate are generally considered passive coatings. Here we demonstrate in a computational

study that the ligands can also strongly affect the redox properties of clusters. By attaching phosphine ligands to various clusters such as simple metal, metal-chalcogenide, noble metal, semiconducting, metal-oxide, transition metal clusters, etc., a severe reduction in the ionization energies in all clusters is shown. Several of the simple and noble metal ligated clusters are transformed into super donors with ionization energies nearly half that of cesium atoms and extremely low second and third ionization energies. The reduction in ionization energy can be split into initial and final state effects. The initial state effect derives in part from the surface dipole but primarily through the formation of bonding/antibonding orbitals that shift the HOMO. The final state effect derives from the enhanced binding of the donor ligand to the charged cluster. In comparing simple and noble metal clusters with transition metal clusters, the strength of the different effects dominates over another. For example, the final state effect plays a more prominent role than the initial state effect in transition metal clusters. Ligation is shown to be an excellent strategy for the formation of multiple electron donors.

The electronic properties of bulk surfaces are modified by depositing a surface layer in which charge transfer and the intrinsic dipole moment of the layer results in band bending that can change the work function of the surface.[1–6] The vast majority of functional nanoparticles and clusters are also coated by a similar layer of ligands or surfactants. The effect of this layer is significant, but sometimes it is an overlooked contributor to the properties of clusters and nanoparticles.[6–18] In this work, we seek to demonstrate how the interaction between ligands and particles can be used to alter their redox properties. We demonstrate that even the weakly interacting ligands can dramatically change the redox character by transforming metallic or semiconducting clusters into donors with I.E. substantially lower or comparable to the atoms with the lowest I.E. in the periodic table. For superatomic clusters, this can lead to entities that can donate multiple electrons with low

I.E.. These developments are strongly valuable as clusters and nanoparticles with remarkable oxidative, or reductive properties are extremely useful in applications such as using dopants to modify conductivity in two-dimensional semiconductors,[19,20] carriers for batteries,[21,22] catalysis,[23–32] and pre-programmed motifs for forming ionic cluster assembled solids when combined with counterions.[10,33–40]

In this study, we examine the effect of phosphine ligands on the electronic properties of a variety of clusters, including simple and noble metal, transition metal, and semiconductor clusters, to detail the types of interaction that may occur between a ligand and the cluster core. The objective is to develop concepts that can help understand the role of ligands in stabilizing multiply-charged ionic particles and the microscopic mechanisms underlying the interaction with ligands. In particular, we examine how a charge transfer ligand such as phosphine affects the I.E. of an atom or cluster and how the ligation provides a strategy for developing multiple electron donors. Hence, a species that have extremely low multiple I.E. may be constructed. From an electron donation viewpoint, the removal of the lowest energy electron starts from the Highest Occupied Molecular Orbital (HOMO). The first step towards building multiple charge donors is then to start with units that have multiple electrons in the highest occupied electronic state or in states close to HOMO. The quantum states in small compact metallic clusters are grouped into shells much in the same way as in atoms.[41,42] Within a simplified model of a nearly free electron gas, the quantum states order as $1S^2$, $1P^6$, $1D^{10}$, $2S^2$, $1F^{14}$, $2P^6$, .. and numerous studies have confirmed the presence of such a shell structure.[43–48] Their similarity with electronic states in atoms has promoted the designation of stable clusters with a well-defined valence known as superatoms. As metallic clusters/superatoms typically have high numbers of degeneracies in the outermost electronic shell, they are ideal candidates for multi-electron donors. Highly symmetric structures in semiconductors

or transition metals clusters cause them to have a high degree of degeneracies at or near the HOMO.

The next step towards controlling the donor characteristics of a cluster or nanoparticle is to control the location of the HOMO. Organic ligands, especially those that form charge-transfer complexes, can serve as excellent candidates for such control. Consider the case of developing multi-electron donors using ligands such as PEt_3, PMe_3, N-ethyl-2-pyrrolidone (EP=$C_6H_{11}NO$) that bind to metal clusters by donating charge.[49,50] Such ligands can help lower the I.E. in different ways, as shown in Figure 3.1. First, through charge transfer, these ligands form surface dipoles leading to an electrostatic shift in the vacuum level or lowering I.E. in a manner similar to the lowering of work function in metals.
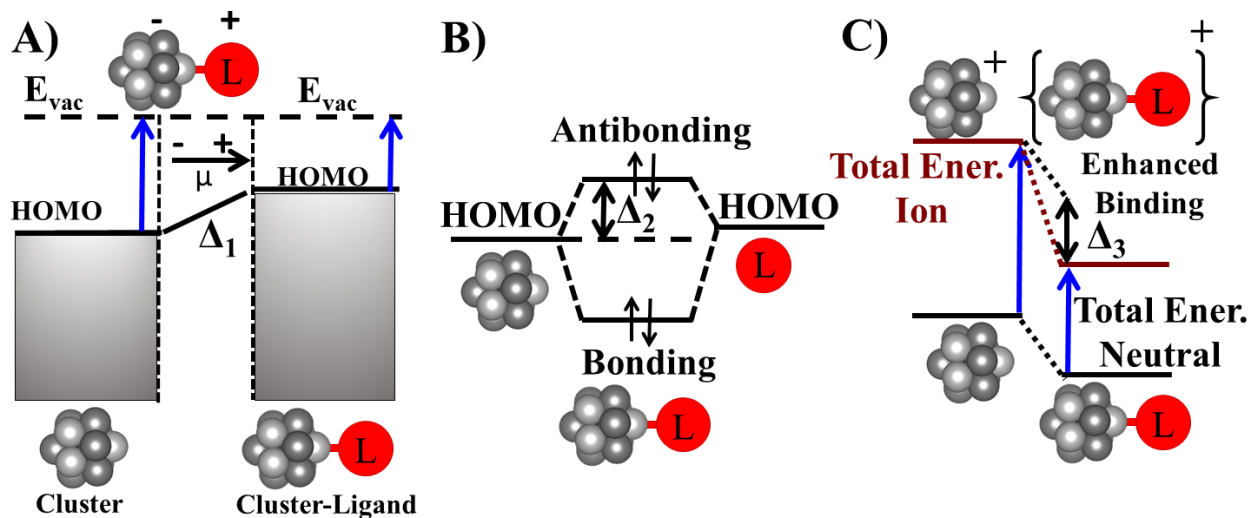
Figure 3.1 Mechanisms that affect the I.E. of a cluster after ligation. A) Dipole-induced shift of the electronic levels. B) Bonding and antibonding shifts in the HOMO, and C) enhanced binding of the ligand to a charged species, and electronic relaxation after ionization.

One can also look upon this change as shifting the HOMO energy (marked as Δ_1 in Figure 3.1) relative to the vacuum level. Secondly, the ligands bond with surface sites forming bonding and

antibonding pairs. The filling of the antibonding states results in the rise of the hybridized HOMO levels marked as Δ_2 in Figure 3.1. The emptying of the antibonding state may also occur, resulting in a reordering of the levels leading to covalent bonding instead of a simple charge-transfer complex. These two effects governed by the nature of the metal cluster and the binding to the ligand can be grouped as *Initial State Effects* (ISE). These effects act on the neutral cluster before ionization. The shift in the energy of the HOMO upon ligation can be used as a rough indicator of the ISE. Finally, the ligands can help lower the I.E. through a *Final State Effect* (FSE) when the ligand binds more strongly to the cationic cluster than to the neutral species, further reducing the I.E., denoted by Δ_3, stabilizing the charged species. This binding enhancement is due to the charge donating nature of the ligand gaining extra stability because the cluster has become a better change acceptor.[23] The combination of these effects can lead to excellent donors that can donate multiple electrons with lower energies, thereby acting as potential reducers. We also examine how the strength of these mechanisms differ as the type of cluster is changed from a simple and noble metallic core to a semiconductor core and a transition metal-based core. The current discussion is aimed towards creating the reducing agents. On the other hand, a similar strategy but using acceptor ligands can lead to controllable oxidizing agents.

Results and discussion

To show how ligation can act to lower the I.E., we consider the Trimethylphosphine, PMe_3 ligand, which is a strong σ-donor that generally increases the electron density in the cluster core through the lone pair of the phosphorus. We found that the lowering in I.E. is a general phenomenon. To clarify how the interplay between the cluster core and the ligand affects the I.E., we examined the change in I.E. of various clusters. The investigations calculated the adiabatic I.E. of simple and noble metal clusters, Au_7,[56] Au_{11},[57] $Au_{13}Cl_2$,[58] Ag_{11}, and Al_7;[59] an Al_4O_6 cluster corresponding to

an insulator;[60] $Ga_{12}N_{12}$,[61] and $Zn_{12}O_{12}$[62] as representative of semiconductor clusters; Co_6, Pd_6, and Pd_7 as representative of transition metal clusters; and Mo_6Te_8[63] corresponding to the essential metal-chalcogenide clusters recently synthesized by Roy and co-workers.[10] In each case, the metal sites were successively covered with PMe_3 ligands. Figure 3.2 shows the ground state geometry and the calculated I.E. of bare and fully ligated clusters considered in this study.

In most cases, the geometry of the bare and ligated cluster are similar; and however, in the case of Au_{11}, Au_7, and $Au_{13}Cl_2$, the structures are notably different. The main reason for different structures is that the phosphine ligands act as charge donors, putting more charge on the metal clusters expanding the bond distances. Gold clusters are unique due to the relativistic contraction of the 6s orbital, and the resulting expansion of the 5d orbital of Gold results in the 5d orbitals participating in bonding.[64,65] The expansion in Au_7 takes the average Au-Au bond distance from 2.69 Å to 2.89 Å. As the distance increases, the interaction between the localized 5d orbitals decreases, and Au tends to behave more like a simple metal. The I.E. of the ligated clusters universally decreases as compared to the bare clusters. The I.E. of the ligated and bare species are shown in Figure 3.2, and Table 3.1 offers additional details. The most significant decrease in I.E. belongs to the noble metal clusters, including Au_7, $Au_{13}Cl_2$, and Au_{11} . The I.E. of $Au_{11}(PMe_3)_{10}$, $Au_7(PMe_3)_7$ $Ag_{11}(PMe_3)_{10}$ are all 2.23 eV to 2.40 eV, slightly more than half that of the atom with the lowest I.E., Cesium (3.89 eV). Even in Mo_6Te_8, which has the most minor decrease in I.E., the I.E. is reduced by 1.68 eV. To analyze the origin of the change in I.E., we examined the HOMO of the bare (A) and ligated clusters and compared the change in HOMO (Δ HOMO) with the shift in the I.E..

Au₁₁(PMe₃)₁₀   Au₁₁   Au₇(PMe₃)₇   Au₇   Au₁₃Cl₂(PMe₃)₁₀   Au₁₃Cl₂

I.E. = 2.23 eV   I.E. = 6.18 eV   I.E. = 2.33 eV   I.E. = 6.53 eV   I.E. = 2.82 eV   I.E. = 6.86 eV

Ag₁₁(PMe₃)₁₀   Ag₁₁   Al₇(PMe₃)₇   Al₇   Al₄O₆(PMe₃)₄   Al₄O₆

I.E. = 2.40 eV   I.E. = 5.40 eV   I.E. = 2.83 eV   I.E. = 5.82 eV   I.E. = 5.68 eV   I.E. = 9.05 eV

Ga₁₂N₁₂(PMe₃)₁₂   Ga₁₂N₁₂   Zn₁₂O₁₂(PMe₃)₁₂   Zn₁₂O₁₂   Mo₆Te₈(PMe₃)₆   Mo₆Te₈

I.E. = 4.15 eV   I.E. = 7.37 eV   I.E. = 4.72 eV   I.E. = 9.05 eV   I.E. = 5.58 eV   I.E. = 7.26 eV

Co₆(PMe₃)₆   Co₆   Pd₆(PMe₃)₆   Pd₆   Pd₇(PMe₃)₇   Pd₇

I.E. = 5.68 eV   I.E. = 9.05 eV   I.E. = 4.54 eV   I.E. = 6.48 eV   I.E. = 4.48 eV   I.E. = 6.38 eV

Figure 3.2 The ground state geometry of bare and fully ligated Au₁₁, Au₇, Au₁₃Cl₂, Ag₁₁, Al₇, Al₄O₆, Ga₁₂N₁₂, Zn₁₂O₁₂, Mo₆Te₈, Co₆, Pd₆, and Pd₇ clusters, along with their respective Ionization Energies.

For all the clusters, the shift in HOMO is calculated using Eq. 3.1, and the % ISE is calculated using Eq. 3.2.

HOMO Shift = HOMO(A-PMe₃)-HOMO(A) …………..(3.1)

%ISE = HOMO Shift / ΔI.E. ………………………… …..(3.2)

The ratio provides an estimate of the portion of the change in the I.E. due to ISE.

Table 3.1 The adiabatic ionization energy of the clusters and the PMe_3 ligated cluster, shift in the HOMO from the neutral cluster to the ligated cluster. PMe_3 binding energy is for the last ligand.

Cluster	I.E. (eV)	I.E. PMe_3 (eV)	Δ I.E. (eV)	HOMO Shift (eV)	FSE (eV)	% ISE	B.E. (eV)
$Au_{13}Cl_2$	6.86	2.82	4.05	3.50	0.55	87	0.30
Au_{11}	6.18	2.23	3.94	3.31	0.63	84	0.43
Ag_{11}	5.40	2.40	3.00	2.43	0.48	81	0.01
$Ga_{12}N_{12}$	7.37	4.15	3.22	2.60	0.62	81	0.69
Au_7	6.53	2.33	4.21	3.38	0.83	80	0.40
Al_4O_6	9.05	5.68	3.37	2.59	0.78	77	1.32
$Zn_{12}O_{12}$	8.11	4.72	3.39	2.64	0.75	77	0.79
Al_7	5.82	2.83	2.99	2.18	0.80	73	0.38
Co_6	6.48	3.77	2.71	1.59	1.12	58	1.60
Pd_7	6.38	4.48	1.91	1.04	0.87	54	1.44
Mo_6Te_8	7.26	5.58	1.68	0.78	0.91	46	1.30
Pd_6	6.48	4.54	1.94	0.81	1.13	41	1.22

Table 3.1 shows the calculated values along with the binding energy of the last ligand. The reduced I.E. falls into two groups depending on the dominance of the ISE or FSE. The first group is marked by a larger ISE and includes simple or noble metal or semiconducting species Au_{11}, Au_7, $Au_{13}Cl_2$, Ag_{11}, Al_7, Al_4O_6, $Ga_{12}N_{12}$, and $Zn_{12}O_{12}$. In contrast, the second group marked by a relatively larger FSE (42%-59%) has transition metal and metal chalcogenide clusters, including Co_6, Pd_6, Pd_7, and Mo_6Te_8. Note that Mo_6Te_8, a cluster with a HOMO-LUMO gap of 0.84, might be expected to behave like the other semiconductor cluster; however, its ISE, FSE, and I.E. are more similar to the other transition metal clusters. This suggests that the presence of *3d* and *4d* valence electrons is more important to this effect than the bandgap energy of the nanoparticle.

The I.E. of the semiconducting and transition metal-based clusters are slightly higher and are in the range of 3.77-5.68 eV, still comparable to the I.E. for alkali atoms. The difference in the two groups is better seen in Figure 3.3 that separates the change in I.E. (ΔI.E.), breaking it down into the ISE (ΔHOMO), and the FSE. The relative size of the ISE and FSE differ considerably with clusters with transition metal atoms and those that have simple or noble metal cores. An intriguing feature of the ligated species is that the reduction in I.E. is not specific to the first I.E., opening the pathway to species that can donate multiple electrons without excessive increase in I.E.. To show this exciting aspect, we examined the 1st, 2nd and 3rd I.E. for the bare and ligated species and found that even the 3rd I.E. in ligated species are less than 11 eV, indicating that the ligated species are truly super donors. For example, $Au_{11}(PMe_3)_{10}$ has a 3rd I.E. of 7.01 eV, less than the first I.E. of the Mg atom, 7.65 eV, and 15.03 eV is the second I.E. of Mg atom. The reduction from the value in bare clusters is not uniform; noble and simple metal clusters undergo larger reductions in I.E., while the smallest reductions in I.E. are for the four transition metal-based clusters. These differences are rooted in the relative importance of ISE and FSE which depend on the nature of the cluster.
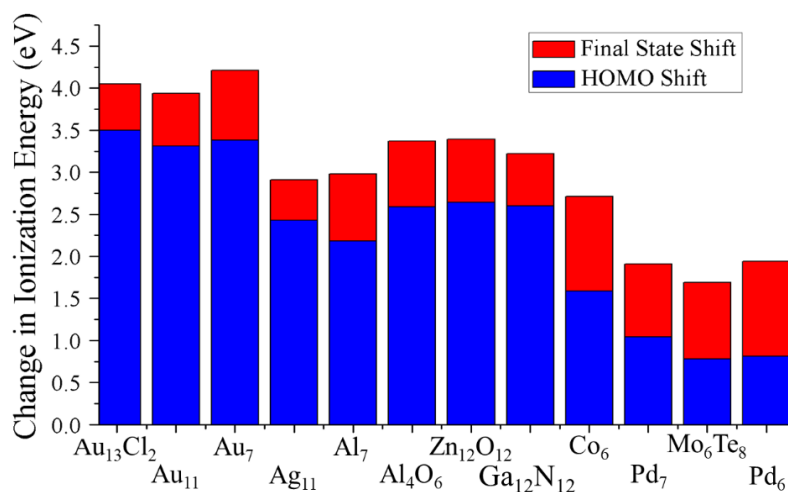
Figure 3.3 The initial and HOMO shift in the ionization energy of the clusters.

The variations in the relative proportion of ISE and FSE are rooted in the nature of bonding. To highlight this difference, we present the interaction diagram that depicts the formation of the electronic states in ligated cluster starting from the bare cluster and the ligands in Figure 3.4. We have examined $Ga_{12}N_{12}$, Au_7, Pd_7, and Co_6 as they represent a semiconductor, noble metal, and two transition metal-based species. In $Ga_{12}N_{12}$, the empty $5s$ orbitals of Ga is filled by interaction with the lone pair of PMe_3, leading to an increase in the HOMO level, while the electronic structure of the cluster is stabilized with a large HOMO-LUMO gap of 2.11 eV. For Au_7, the bonding with s-states leads to the formation of the antibonding orbitals that considerably increase the energy of the HOMO, a larger increase than in the case of $Ga_{12}N_{12}$. As the antibonding orbital between the phosphine ligand pushes up the HOMO, this destabilizes the neutral cluster leading to an extremely
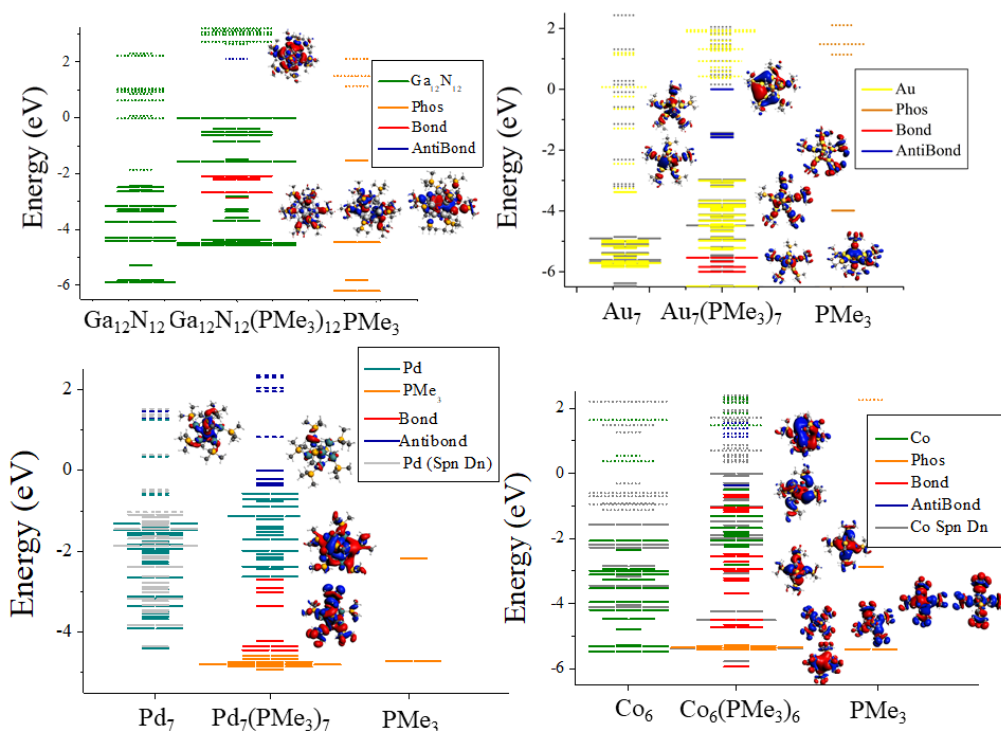
Figure 3.4 Molecular orbital diagrams for the binding of $Ga_{12}N_{12}$, Au_7, Pd_7, and Co_6 to PMe_3. Continuous lines represent filled orbitals while the dashed lines represent unfilled orbitals. Colored lines or for the spin majority channel, the gray lines are for the spin minority channel.

low I.E. For Pd7, the change in HOMO is smaller than that seen in other clusters due to the electronic relaxation when the covalent bond forms between the cluster and the PMe3. This electronic relaxation is shown by forming the antibonding orbitals near the HOMO. In contrast, other antibonding orbitals derived from the *4d* orbitals of Pd are partially emptied, quenching the magnetic moment. This phenomenon is also observed in the Co6 cluster as the orbitals near the HOMO are also antibonding in nature. The magnetic moment of the cluster decreases from 14 μ_B to 8 μ_B. Thus, the increase in the HOMO level is decreased due to the ability of changing the occupations in s and d orbitalss. This reduces the initial state effect while the final state effect is maintained. To analyze this phenomenon in a more straightforward system, we have examined how the I.E. of Na, Mg, Al, Mo, Co, Pd, Au, and Zn atoms are affected by PMe3. The largest decrease in I.E. after ligation is found for Au, Zn, and Mo, where the I.E. decreases by 3.92, 2.97, and 2.57 eV, respectively.
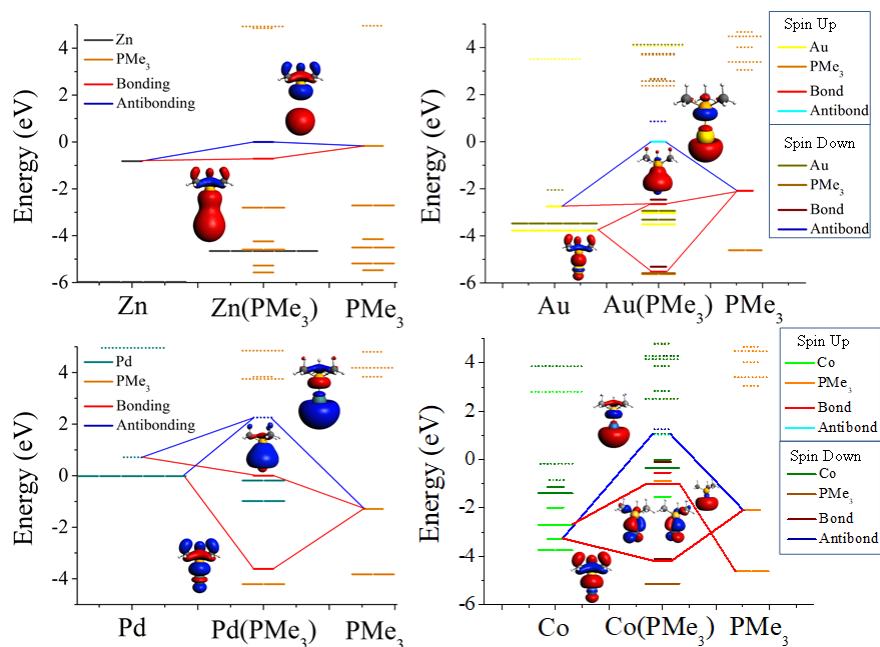
Figure 3.5 Molecular orbital diagrams for the atoms Zn, Au, Pd, and Co when binding with PMe3 ligand

By using only a single ligand, we can use the dipole moments to analyze if the initial state effect is dominated by the surface dipole. Despite having larger dipole moments, surprisingly, Al and Na have the smallest changes in I.E.. Hence, we can infer that the dipole moment and change in I.E. are not strongly correlated, nor is the dipole moment and the shift in the HOMO levels. In analyzing the importance of the final state effect, it is seen that the ISE is only 1% for Pd. This is due to the ligand field splitting of the atomic *4d* orbitals of Pd in which the ligand forms weakly bonding and antibonding orbitals with the *5s* orbital of Pd atom, as shown in Figure 3.5. There is a trivial change in the energy of the HOMO due to the weakly bonding orbital being the HOMO. The binding energy of the ligand to the Pd neutral is quite strong at 2.17 eV, but the binding energy of the cation is even higher, almost twice that of the neutral atom. The change in I.E. is then almost entirely due to FSE, where the removal of the electron enhances the binding with the cation.

Returning to the ligated clusters, we find further evidence that the formation of bonding and antibonding orbitals are critical for understanding the reduction in the I.E.. We do this by examining the charge transfer between the ligand and cluster by studying the Hirshfeld charges on the clusters. However, the ligands donate charge to most of the neutral clusters, not to Pd_6 and Pd_7 Clusters. Thus, the dipole due to charge transfer has the opposite sign suggesting the I.E. should increase. Instead, the bonding/anti-bonding effects in the ISE overshadow the dipole-induced changes leading to an increase in the energy of the HOMO. We calculated the binding energy of the last ligand to the neutral and charged species, and Figure 3.6 shows the variation of the binding energy with charged state, including the binding energy to the neutral species. For simple and noble metal species Al_7, Au_7, Au_{11}, $Au_{13}Cl_2$, the binding energy varies linearly with the charge state, which, if extrapolated, has a y-intercept close to zero at 0.27 eV. For the transition metal clusters, the binding energy of the neutral clusters is typically more prominent, with a y-intercept

49

averaging 1.33 eV and the slope being positive but somewhat lower than the slope for the metallic clusters. This implies that in the transition metal clusters, the electronic structure is affected by the binding, and the ligands are non-innocent.

In contrast, for the simple and noble metal clusters, the ligands are innocent. The striking result is that the binding energy of phosphine to metallic clusters is greatly enhanced by charging the cluster. This effect is a significant portion of the FSE, as phosphine being a better charge donor binds much more strongly to a decent charge acceptor. By making the cluster more positively charged, it enhances the binding energy of the ligand. For this reason, the vast majority of phosphine-protected gold clusters have multiple positive charges.
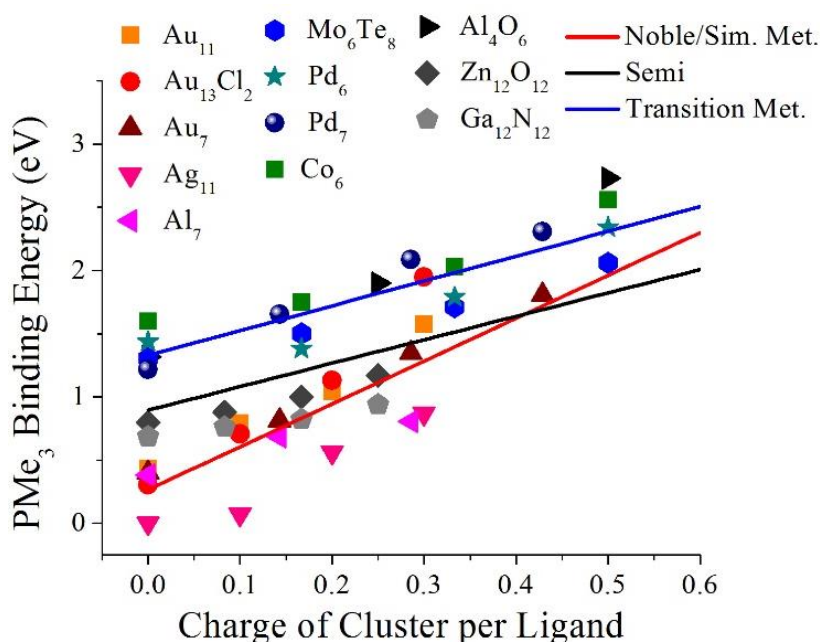
Figure 3.6 The binding energy of PMe$_3$ as a function of the charge of the cluster divided by the number of PMe$_3$ ligands. A linear regression is plotted for the noble metal and simple metal clusters, Au$_{11}$, Au$_{13}$Cl$_2$, Au$_7$, Ag$_{11}$, and Al$_7$, the transition metal clusters, Mo$_6$Te$_8$, Pd$_6$, Pd$_7$, and Co$_6$, and the semiconducting clusters, Al$_4$O$_6$, Zn$_{12}$O$_{12}$, and Ga$_{12}$N$_{12}$. Lines are plotted using a linear least squares method.

Conclusions

The present studies investigated the ligand effects on the I.E. of various clusters, including simple metal and noble metal, semiconductor, and transition metal-based clusters before and after PMe_3 ligation. The substantial reduction in the I.E. of clusters was found to be a universal phenomenon incurred by phosphine ligation. An analogous effect has recently been experimentally observed in the electron affinities of Cobalt-Sulfide Clusters, with the ligand exchange from PEt_3 to CO ligands leading to a systematic increase in the electron affinity.[8] The mechanism by which this shift in I.E. occurs is different from the conventional approach in bulk. The formation of the dipole layer can lead to a reduction in the work function, and in the atomic case where the filling of electronic shells controls I.E.. As we show, the I.E. of different clusters can be reduced by attaching ligands that form charge-transfer complexes. While part of the reduction is associated with a cluster version of band bending, the formation of bonding/anti-bonding pairs labeled as the initial state effect.

On the other hand, the binding enhancement in the cationic clusters and their stabilization at the charged state by the ligands also play a crucial role. The effect is called the final state effect. We also found that the nature of the cluster core affects how the I.E. would be reduced. In the simple metal and noble metal clusters, the initial state effect is more prominent as the antibonding orbitals formed between phosphine and the metal increase the HOMO of the neutral cluster leading to a lowering of the I.E.. In transition metal clusters, the electronic relaxation of the cluster core prevents the HOMO from increasing as much as in simple metal and noble metal clusters. After the electron is removed, the covalent binding may be enhanced through further electronic relaxation. The ligand effect in a finite size has several additional features. Firstly, the I.E. can be controlled by changing the number of ligands, enabling species with tunable ionization characteristics. Secondly, the ligand effect allows a pathway to create donor species that can donate

multiple electrons. Finally, the ligand effect can be combined with the electronic shell effect in simple metal and noble metal clusters to create multiple donor species with very low I.E.. Such species could be utilized as dopants (donors) in semiconductors.

References

(1)   Zhou, Y.; Fuentes-Hernandez, C.; Shim, J.; Meyer, J.; Giordano, A. J.; Li, H.; Winget, P.; Papadopoulos, T.; Cheun, H.; Kim, J.; et al. A Universal Method to Produce Low–Work Function Electrodes for Organic Electronics. *Science* **2012**, *336*, 327–332.

(2)   Alloway, D. M.; Graham, A. L.; Yang, X.; Mudalige, A.; Colorado, R.; Wysocki, V. H.; Pemberton, J. E.; Randall Lee, T.; Wysocki, R. J.; Armstrong, N. R. Tuning the Effective Work Function of Gold and Silver Using ω-Functionalized Alkanethiols: Varying Surface Composition through Dilution and Choice of Terminal Groups. *J. Phys. Chem. C* **2009**, *113*, 20328–20334.

(3)   Ford, W. E.; Gao, D.; Knorr, N.; Wirtz, R.; Scholz, F.; Karipidou, Z.; Ogasawara, K.; Rosselli, S.; Rodin, V.; Nelles, G.; et al. Organic Dipole Layers for Ultralow Work Function Electrodes. *ACS Nano* **2014**, *8*, 9173–9180.

(4)   Roberts, F. S.; Anderson, S. L.; Reber, A. C.; Khanna, S. N. Initial and Final State Effects in the Ultraviolet and X-Ray Photoelectron Spectroscopy (UPS and XPS) of Size-Selected Pd_n Clusters Supported on TiO_2(110). *J. Phys. Chem. C* **2015**, *119*, 6033–6046.

(5)   Reber, A. C.; Khanna, S. N.; Roberts, F. S.; Anderson, S. L. Effect of O_2 and CO Exposure on the Photoelectron Spectroscopy of Size-Selected Pd_n Clusters Supported on TiO_2(110). *J. Phys. Chem. C* **2016**, *120*, 2126–2138.

(6)   Boles, M. A.; Ling, D.; Hyeon, T.; Talapin, D. V. The Surface Science of Nanocrystals. *Nature Materials* **2016**, *15*, 141–153.

(7)   Clayborne, P. A.; Lopez-Acevedo, O.; Whetten, R. L.; Gronbeck, H.; Hakkinen, H. Evidence of Superatom Electronic Shells in Ligand-Stabilized Aluminum   Clusters. *J. Chem. Phys.* **2011**, *135*, 094701.

(8)   Liu, G.; Pinkard, A.; Ciborowski, S. M.; Chauhan, V.; Zhu, Z.; Aydt, A. P.; Khanna, S. N.; Roy, X.; Bowen, K. H. Tuning the Electronic Properties of Hexanuclear Cobalt Sulfide Superatoms via Ligand Substitution. *Chem. Sci.* **2019**, *10*, 1760–1766.

(9)   Aikens, C. M. Electronic Structure of Ligand-Passivated Gold and Silver Nanoclusters. *J. Phys. Chem. Lett.* **2011**, *2*, 99–104.

(10)   Roy, X.; Lee, C.-H.; Crowther, A. C.; Schenck, C. L.; Besara, T.; Lalancette, R. A.; Siegrist, T.; Stephens, P. W.; Brus, L. E.; Kim, P.; et al. Nanoscale Atoms in Solid-State Chemistry. *Science* **2013**, *341*, 157–160.

(11)   Abreu, M. B.; Powell, C.; Reber, A. C.; Khanna, S. N. Ligand-Induced Active Sites: Reactivity of Iodine-Protected Aluminum Superatoms with Methanol. *J. Am. Chem. Soc.* **2012**, *134*, 20507–20512.

(12)   Luo, Z.; Reber, A. C.; Jia, M.; Blades, W. H.; Khanna, S. N.; Castleman, A. W. What Determines If a Ligand Activates or Passivates a Superatom Cluster? *Chem. Sci.* **2016**, *7*, 3067–3074.

(13)   E. Johnson, G.; Olivares, A.; Hill, D.; Laskin, J. Cationic Gold Clusters Ligated with Differently Substituted Phosphines: Effect of Substitution on Ligand Reactivity and Binding. *Physical Chemistry Chemical Physics* **2015**, *17*, 14636–14646.

(14)   Johnson, G. E.; Laskin, J. Understanding Ligand Effects in Gold Clusters Using Mass Spectrometry. *Analyst* **2016**, *141*, 3573–3589.

(15)   Akin, S. T.; Zamudio-Bayer, V.; Duanmu, K.; Leistner, G.; Hirsch, K.; Bülow, C.; Ławicki, A.; Terasaki, A.; von Issendorff, B.; Truhlar, D. G.; et al. Size-Dependent Ligand Quenching of Ferromagnetism in $Co_3(Benzene)_n^+$ Clusters Studied with X-Ray Magnetic Circular Dichroism Spectroscopy. *J. Phys. Chem. Lett.* **2016**, *7*, 4568–4575.

(16)   An, P.; Anumula, R.; Wu, H.; Han, J.; Luo, Z. Charge Transfer Interactions of Pyrazine with Ag_{12} Clusters towards Precise SERS Chemical Mechanism. *Nanoscale* **2018**, *10*, 16787–16794.

(17)   Pinkard, A.; Champsaur, A. M.; Roy, X. Molecular Clusters: Nanoscale Building Blocks for Solid-State Materials. *Acc. Chem. Res.* **2018**, *51*, 919–929.

(18)   Yue, L.; Wang, N.; Zhou, S.; Sun, X.; Schlangen, M.; Schwarz, H. The Electric Field as a "Smart" Ligand in Controlling the Thermal Activation of Methane and Molecular Hydrogen. *Angewandte Chemie International Edition* **2018**, *57*, 14635–14639.

(19)   Yu, J.; Lee, C.-H.; Bouilly, D.; Han, M.; Kim, P.; Steigerwald, M. L.; Roy, X.; Nuckolls, C. Patterning Superatom Dopants on Transition Metal Dichalcogenides. *Nano Lett.* **2016**, *16*, 3385–3389.

(20)   Reber, A. C.; Khanna, S. N. $Co_6Se_8(PEt_3)_6$ Superatoms as Tunable Chemical Dopants for Two-Dimensional Semiconductors. *npj Computational Materials* **2018**, *4*, 33.

(21)   Yoshikawa, H.; Kazama, C.; Awaga, K.; Satoh, M.; Wada, J. Rechargeable Molecular Cluster Batteries. *Chemical Communications* **2007**, 3169–3170.

(22)   Kawasaki, N.; Wang, H.; Nakanishi, R.; Hamanaka, S.; Kitaura, R.; Shinohara, H.; Yokoyama, T.; Yoshikawa, H.; Awaga, K. Nanohybridization of Polyoxometalate Clusters and

Single-Wall Carbon Nanotubes: Applications in Molecular Cluster Batteries. *Angew. Chem. Int. Ed.* **2011**, *123*, 3533–3536.

(23)   Metiu, H.; Chrétien, S.; Hu, Z.; Li, B.; Sun, X. Chemistry of Lewis Acid–Base Pairs on Oxide Surfaces. *J. Phys. Chem. C* **2012**, *116*, 10439–10450.

(24)   Reber, A. C.; Khanna, S. N. Effect of Embedding Platinum Clusters in Alumina on Sintering, Coking, and Activity. *J. Phys. Chem. C* **2017**, *121*, 21527–21534.

(25)   Yang, Y.; E Castano, C.; Frank Gupton, B.; C. Reber, A.; N. Khanna, S. A Fundamental Analysis of Enhanced Cross-Coupling Catalytic Activity for Palladium Clusters on Graphene Supports. *Nanoscale* **2016**, *8*, 19564–19572.

(26)   Yang, Y.; Reber, A. C.; Gilliland, S. E.; Castano, C. E.; Gupton, B. F.; Khanna, S. N. More than Just a Support: Graphene as a Solid-State Ligand for Palladium-Catalyzed Cross-Coupling Reactions. *J. Catal.* **2018**, *360*, 20–26.

(27)   Arceo, E.; Jurberg, I. D.; Álvarez-Fernández, A.; Melchiorre, P. Photochemical Activity of a Key Donor–Acceptor Complex Can Drive Stereoselective Catalytic α-Alkylation of Aldehydes. *Nature Chemistry* **2013**, *5*, 750–756.

(28)   Wu, Z.; Hu, G.; Jiang, D.; Mullins, D. R.; Zhang, Q.-F.; Allard, L. F.; Wang, L.-S.; Overbury, S. H. Diphosphine-Protected Au_{22} Nanoclusters on Oxide Supports Are Active for Gas-Phase Catalysis without Ligand Removal. *Nano Lett.* **2016**, *16* (10), 6560–6567.

(29)   Yang, Y.; Reber, A. C.; S. E. Gilliland, I. I. I.; Castano, C. E.; Gupton, B. F.; Khanna, S. N. Donor/Acceptor Concepts for Developing Efficient Suzuki Cross-Coupling Catalysts Using Graphene-Supported Ni, Cu, Fe, Pd, and Bimetallic Pd/Ni Clusters. *J. Phys. Chem. C* **2018**, *122*, 25396–25403.

(30)   Ha, M.-A.; Baxter, E. T.; Cass, A. C.; Anderson, S. L.; Alexandrova, A. N. Boron Switch for Selectivity of Catalytic Dehydrogenation on Size-Selected Pt Clusters on Al_2O_3. *J. Am. Chem. Soc.* **2017**, *139*, 11568–11575.

(31)   Baxter, E. T.; Ha, M.-A.; Cass, A. C.; Zhai, H.; Alexandrova, A. N.; Anderson, S. L. Diborane Interactions with Pt_7/Alumina: Preparation of Size-Controlled Borated Pt Model Catalysts. *J. Phys. Chem. C* **2018**, *122*, 1631–1644.

(32)   Shekhar, M.; Wang, J.; Lee, W.-S.; Williams, W. D.; Kim, S. M.; Stach, E. A.; Miller, J. T.; Delgass, W. N.; Ribeiro, F. H. Size and Support Effects for the Water–Gas Shift Catalysis over Gold Nanoparticles Supported on Model Al_2O_3 and TiO_2. *J. Am. Chem. Soc.* **2012**, *134*, 4700–4708.

(33)   Qian, M.; Reber, A. C.; Ugrinov, A.; Chaki, N. K.; Mandal, S.; Saavedra, H. M.; Khanna, S. N.; Sen, A.; Weiss, P. S. Cluster-Assembled Materials: Toward Nanomaterials with Precise Control over Properties. *ACS Nano* **2009**, *4*, 235–240.

(34)   O'Brien, E. S.; Trinh, M. T.; Kann, R. L.; Chen, J.; Elbaz, G. A.; Masurkar, A.; Atallah, T. L.; Paley, M. V.; Patel, N.; Paley, D. W.; et al. Single-Crystal-to-Single-Crystal Intercalation of a Low-Bandgap Superatomic Crystal. *Nature Chemistry* **2017**, *9*, 1170.

(35)   Champsaur, A. M.; Velian, A.; Paley, D. W.; Choi, B.; Roy, X.; Steigerwald, M. L.; Nuckolls, C. Building Diatomic and Triatomic Superatom Molecules. *Nano Lett.* **2016**, *16*, 5273–5277.

(36)   Mandal, S.; Reber, A. C.; Qian, M.; Weiss, P. S.; Khanna, S. N.; Sen, A. Controlling the Band Gap Energy of Cluster-Assembled Materials. *Acc. Chem. Res.* **2013**, *46*, 2385–2395.

(37) Turkiewicz, A.; Paley, D. W.; Besara, T.; Elbaz, G.; Pinkard, A.; Siegrist, T.; Roy, X. Assembling Hierarchical Cluster Solids with Atomic Precision. *J. Am. Chem. Soc.* **2014**, *136*, 15873–15876.

(38) Shott, J. L.; Freeman, M. B.; Saleh, N.-A.; Jones, D. S.; Paley, D. W.; Bejger, C. Ball and Socket Assembly of Binary Superatomic Solids Containing Trinuclear Nickel Cluster Cations and Fulleride Anions. *Inorg. Chem.* **2017**, *56*, 10984–10990.

(39) Kysliak, O.; Nguyen, D. D.; Clayborne, A. Z.; Schnepf, A. [PtZn$_2$Ge$_{18}$(Hyp)$_8$] (Hyp = Si(SiMe$_3$)$_3$): A Neutral Polynuclear Chain Compound with Ge$_9$(Hyp)$_3$ Units. *Inorg. Chem.* **2018**, *57*, 12603–12609.

(40) Li, B.; Li, W.; Li, H.; Wu, L. Ionic Complexes of Metal Oxide Clusters for Versatile Self-Assemblies. *Acc. Chem. Res.* **2017**, *50*, 1391–1399.

(41) Knight, W. D.; Clemenger, K.; de Heer, W. A.; Saunders, W. A.; Chou, M. Y.; Cohen, M. L. Electronic Shell Structure and Abundances of Sodium Clusters. *Phys. Rev. Lett.* **1984**, *52*, 2141–2143.

(42) Khanna, S. N.; Jena, P. Atomic Clusters: Building Blocks for a Class of Solids. *Phys. Rev. B* **1995**, *51*, 13705–13716.

(43) Leuchtner, R. E.; Harms, A. C.; Castleman, A. W. Thermal Metal Cluster Anion Reactions: Behavior of Aluminum Clusters with Oxygen. *J. Chem. Phys.* **1989**, *91*, 2753.

(44) Martin, T. P.; Bergmann, T.; Göhlich, H.; Lange, T. Observation of Electronic Shells and Shells of Atoms in Large Na Clusters. *Chemical Physics Letters* **1990**, *172*, 209–213.

(45) Fedrigo, S.; Harbich, W.; Belyaev, J.; Buttet, J. Evidence for Electronic Shell Structure of Small Silver Clusters in the Optical Absorption Spectra. *Chemical Physics Letters* **1993**, *211*, 166–170.

(46)   Li, X.; Wu, H.; Wang, X.-B.; Wang, L.-S. S- p Hybridization and Electron Shell Structures in Aluminum Clusters: A Photoelectron Spectroscopy Study. *Phys. Rev. Lett.* **1998**, *81*, 1909–1912.

(47)   Wrigge, G.; Hoffmann, M. A.; Issendorff, B. v. Photoelectron Spectroscopy of Sodium Clusters: Direct Observation of the Electronic Shell Structure. *Phys. Rev. A* **2002**, *65*, 063201.

(48)   Chauhan, V.; Singh, A.; Majumder, C.; Sen, P. Structural, Electronic and Magnetic Properties of Binary Transition Metal Aluminum Clusters: Absence of Electronic Shell Structure. *J. Phys.: Condens. Matter* **2014**, *26*, 015006.

(49)   Chauhan, V.; Reber, A. C.; Khanna, S. N. Metal Chalcogenide Clusters with Closed Electronic Shells and the Electronic Properties of Alkalis and Halogens. *J. Am. Chem. Soc.* **2017**, *139*, 1871–1877.

(50)   Chauhan, V.; Reber, A. C.; Khanna, S. N. Strong Lowering of Ionization Energy of Metallic Clusters by Organic Ligands without Changing Shell Filling. *Nature Communications* **2018**, *9*, 2357.

(51)   te Velde, G.; Bickelhaupt, F. M.; Baerends, E. J.; Fonseca Guerra, C.; van Gisbergen, S. J. A.; Snijders, J. G.; Ziegler, T. Chemistry with ADF. *J. Comput. Chem.* **2001**, *22*, 931–967.

(52)   Perdew, J. P.; Yue, W. Accurate and Simple Density Functional for the Electronic Exchange Energy: Generalized Gradient Approximation. *Phys. Rev. B* **1986**, *33*, 8800–8802.

(53)   Van Lenthe, E.; Baerends, E. J. Optimized Slater-Type Basis Sets for the Elements 1–118. *Journal of Computational Chemistry* **2003**, *24*, 1142–1156.

(54)   van Lenthe, E.; van Leeuwen, R.; Baerends, E. J.; Snijders, J. G. Relativistic Regular Two-Component Hamiltonians. *Int. J. Quantum Chem.* **1996**, *57*, 281–293.

(55)   van Lenthe, E.; Ehlers, A.; Baerends, E.-J. Geometry Optimizations in the Zero Order Regular Approximation for Relativistic Effects. *J. Chem. Phys.* **1999**, *110*, 8943–8953.

(56)   Van der Velden, J. W. A.; Beurskens, P. T.; Bour, J. J.; Bosman, W. P.; Noordik, J. H.; Kolenbrander, M.; Buskes, J. A. K. M. Intermediates in the Formation of Gold Clusters. Preparation and x-Ray Analysis of $[Au_7(PPh_3)_7]^+$ and Synthesis and Characterization of $[Au_8(PPh_3)_6I]PF_6$. *Inorg. Chem.* **1984**, *23*, 146–151.

(57)   Bertino, M. F.; Sun, Z.-M.; Zhang, R.; Wang, L.-S. Facile Syntheses of Monodisperse Ultrasmall Au Clusters. *J. Phys. Chem. B* **2006**, *110*, 21416–21418.

(58)   Briant, C. E.; Theobald, B. R. C.; White, J. W.; Bell, L. K.; Mingos, D. M. P.; Welch, A. J. Synthesis and X-Ray Structural Characterization of the Centred Icosahedral Gold Cluster Compound $[Au_{13}(PMe_2Ph)_{10}Cl_2](PF_6)_3$; The Realization of a Theoretical Prediction. *J. Chem. Soc., Chem. Comm.* **1981**, 5, 201.

(59)   Reveles, J. U.; Khanna, S. N.; Roach, P. J.; Castleman, A. W. Multiple Valence Superatoms. *Proceedings of the National Academy of Sciences* **2006**, *103*, 18405–18410.

(60)   Rahane, A. B.; Deshpande, M. D.; Kumar, V. Structural and Electronic Properties of $(Al_2O_3)_n$ Clusters with n = 1–10 from First Principles Calculations. *J. Phys. Chem. C* **2011**, *115*, 18111–18121.

(61)   Zhao, J.; Wang, B.; Zhou, X.; Chen, X.; Lu, W. Structure and Electronic Properties of Medium-Sized Ga_nN_n Clusters (n=4–12). *Chemical Physics Letters* **2006**, *422*, 170–173.

(62)   Reber, A. C.; Khanna, S. N.; Hunjan, J. S.; Beltran, M. R. Rings, Towers, Cages of ZnO. *Eur. Phys. J. D* **2007**, *43*, 221–224.

(63)   Gocke, E.; Schoellhorn, R.; Aselmann, G.; Mueller-Warmuth, W. Molybdenum Cluster

Chalcogenides Mo_6X_8: Intercalation of Lithium via Electron/Ion Transfer. *Inorg. Chem.* **1987**,

26, 1805–1812.

(64)   Häkkinen, H.; Moseler, M.; Landman, U. Bonding in Cu, Ag, and Au Clusters: Relativistic

Effects, Trends, and Surprises. *Phys. Rev. Lett.* **2002**, *89*, 033401.

(65)   Blades, W. H.; Reber, A. C.; Khanna, S. N.; López-Sosa, L.; Calaminici, P.; Köster, A. M.

Evolution of the Spin Magnetic Moments and Atomic Valence of Vanadium in VCu_x^+, VAg_x^+,

and VAu_x^+ Clusters (x = 3–14). *J. Phys. Chem. A* **2017**, *121*, 2990–2999.

Chapter 4

Fused superatomic clusters

The fusion of superatomic clusters to form dimers leads to strong inter superatomic coupling. The combination of electronic structure and optical data has exhibited delocalization of electronic coupling and electron delocalization during the fusion.[1] One of the most fundamental questions was to find how the coupling between the constituent clusters incurs the magnetic state and the internal electric dipole in the fused cluster. We have found that the magnetic state and the dipole moment can be significantly enhanced for the fused cluster. Then there arises a question if enhancement of such fundamental properties can be used for different applications. This part of the thesis will put some light on such promising possibilities.

Furthermore, as discussed in the previous section, ligation can also induce variations in the individual clusters' redox properties. Thus, with plenty of flexibility to tune electronic and redox properties, fused superatomic clusters are an interesting subject to study. However, the research on the fused cluster is still in its infancy. Still, we have shown its potential applications in nano p-n junctions, spintronics, photovoltaics, and a flexible building block for the cluster assembled materials.

The first section of this chapter deals with our research article where metal chalcogenide dimer, $[Re_6S_8(PEt_3)_3Cl_2]_2$, exhibits band-bending-like properties. Furthermore, it is shown to behave like a nano p-n junction, and the external field can modulate the electronic levels. Moreover, it is found that such dimer is helpful in light-harvesting applications.

In the second section, the formation of magnetic dimer [(PMe$_3$)$_5$(Fe$_6$S$_8$)$_2$(CO)$_5$] is elaborated. Additionally, its potential spintronics-related applications due to the intense internal electric diploe and gigantic magnetic moment are also explored.

Finally, in the third section, the theoretical work explaining the formation of the cluster assembled material using [Co$_6$Se$_8$(PEt$_3$)$_5$]$_2$ dimer and [C$_{70}$]$_2$ dimers in the presence of Toluenes solvents are shown. Apart from the theoretical explanations of the formation of cluster assembled materials, we also discovered an intriguing magnetic character in the metal-chalcogenides dimers. The metal chalcogenide dimers in the solid exhibited the localized magnetic moment at the junction of the metal chalcogenide dimers, where two Co$_6$Se$_8$(PEt$_3$)$_5$ clusters combine to form the dimer through their unligated (transition metal atoms) sites.

Chapter 4a

Superatomic Molecules with Internal Electric Fields for Light Harvesting.

The study of superatomic dimer [Re$_6$S$_8$(PEt$_3$)$_3$Cl$_2$]$_2$ is found to display band-bending-like characteristics at the junction of the fused dimer, where two clusters combine to form a fused dimer. The fused dimer showed promising potential in photovoltaics applications. This chapter has been reproduced from the article which I co-authored. It has been slightly adapted for the readability in the framework of my dissertation. Still, it has not been changed in any way affecting the data, meaning, or interpretation. Adapted from *Nanoscale*, **2020**, **12**, 4736-4742. Copyright (2020) Royal Society of Chemistry.

4a.1. Introduction

Traditional p-n junctions used for photovoltaics require an interface where an electric field separates a light-induced electron-hole pair. Developing alternate strategies for forming strong internal electric fields for electron-hole pair separation offers the possibility for better performance. We demonstrate that fusing two superatomic clusters with donor/acceptor ligands on opposite sides of the cluster spearheads a strong internal electric field. In a fused metal-chalcogenide dimer consisting of $Re_6S_8Cl_2(L)_4$ superatomic clusters with donor PMe_3 ligands and acceptor CO ligands on the opposite sides, the electronic levels undergo shifts analogous to band bending in traditional p-n junctions. The fused cluster has a large dipole moment, and an optical spectrum shows strong absorption excitations above the HOMO-LUMO gap of the fused clusters but is optically very weak for the lowest energy excitations that can lead to electron-hole pair recombination. This is because the electron is localized on the CO portion of the fused cluster, while the electron-hole is localized on the PMe_3 side of the cluster. Furthermore, it is demonstrated that the electronic states localized on each side of the cluster can be aligned/misaligned by applying voltage in different directions, offering diode-like characteristics.

The formation of an interface with an internal electric field can allow for the separation of electron-hole pairs as well as directed electrical transport.[2–6] In typical p-n junctions, n- and p- type semiconductors are joined together, and the chemical potential imbalance leads to a flow of charge across the junction boundary resulting in the formation of a depletion layer and an internal electric field.[7] The internal electric field can separate electron-hole pairs or provide a diode character as the width of the depletion layer can change with the direction of the applied voltage.[8,9] To construct a p-n junction at the cluster level, one would need to join two clusters with different chemical potentials to produce such an internal electric field. However, in most fused clusters, where two

superatomic clusters are strongly bound, the clusters are identical.[10,11] A dimer of two identical clusters will not generally exhibit a large internal electric field or dipole moment, and the binding of two different atom precise clusters requires exquisite chemical control.[12–14] One promising candidate for such systems is metal chalcogenide clusters, as Roy and co-workers have reported the formation of highly stable ligated metal chalcogenide clusters, including $Co_6Se_8(PEt_3)_6$, $Cr_6Te_8(PEt_3)_6$, $Ni_9Te_6(PEt_3)_8$. The clusters are composed of metal-chalcogenide cores with ligands such as triethylphosphine (PEt_3) attached to the metal sites.[15–20] However, to create an internal electric field, the location of the energy levels in the constituent units needs to be controllable. In recent work, we investigated this possibility in metal-chalcogenide clusters.[21–25] The electronic donor or acceptor characteristics of these clusters can be controlled by attaching appropriate ligands.[21,22] The electronic spectrum of metal-chalcogenide clusters can be raised or lowered by using donors (e.g., phosphine) or acceptors (e.g., CO) ligands where the phosphine raises the electronic spectra making the cluster a better donor, while the CO lowers the spectrum making the cluster a better acceptor.[21,22] This can be done via raising or lowering the electronic spectra, without significant variation in the HOMO-LUMO (Highest Occupied Molecular Orbital, Lowest Unoccupied Molecular Orbital) gap. These predictions have since been confirmed by experiment and provide a unique possibility to tune donor or acceptor characteristics without changing the electron count.[26] Recent experiments by Nuckolls and co-workers have also shown that it is possible to make molecular dimers of metal-chalcogenide clusters with precise control over the placement of ligands.[11] These fused metal-chalcogenide clusters are an ideal system for creating p-n junctions in the cluster size regime, but how can an internal electric field be induced? This work demonstrates that large dipole moments in fused molecular clusters can be generated by joining identical metal-chalcogenide clusters and breaking the

64

symmetry by ligating opposite units of the fused cluster with donor or acceptor ligand Re_8S_8 is our first example because it has the largest HOMO-LUMO gap of the metal chalcogenide clusters when it is in the +2 oxidation state, and it is known to be a semiconductor when assembled into materials.[27–31] When the clusters are fused together, the interface is marked by bonds between the Re and S sites belonging to the two units. We then attach charge donating PMe_3 (Trimethylphosphine) ligands that make one side of the fused cluster a better donor and charge accepting ligands, CO, making the other side of the fused cluster a better acceptor. The shift in the electronic levels in the composite superatomic molecule is reminiscent of the band bending found in conventional p- and n- junctions without the formation of the depletion layer. The difference in redox properties induced by the ligands leads to a large dipole moment. Investigations into the electric field required to counter the dipole indicate that the effect is equivalent to applying a voltage of 1.7 V across the cluster. We consider the fused cluster with separated donor-acceptor ligands to be a nano p-n junction. It is shown that the junction has an interesting transport characteristic in that the application of an electric field increases or lowers the barrier at the interface depending on the direction of the field, suggesting that the nano unit has diode-like characteristics. The absorption spectra reveal that the optical gap (the lowest energy excitation that readily absorbs light) of the fused clusters is significantly higher than the HOMO-LUMO gap of the fused clusters, and because the absorption at the HOMO-LUMO gap once the electron-hole pairs are separated is optically weak, this suggests that electron-hole pair recombination will be inhibited. The findings are fairly general, and we also present results on Co_6S_8 based clusters to show that the concept may be extended to other dimeric superatom clusters.

4a.2. Results and discussion
Metal-chalcogenide clusters with large HOMO-LUMO Gaps

The first step towards developing such p-n junctions is the identification of clusters with well-defined valence and large HOMO-LUMO gaps. Such clusters may be classified as superatoms and are well-positioned to maintain identity when integrated into assemblies.[32,33] Within this context, metal chalcogenide clusters have recently received considerable attention for the formation of functional solids with tunable properties, including ferromagnetism, semiconductors with tunable optical gaps, and variable conductivity.[11,15–20,34–36] An important advantage of this approach over traditional atomic solids is that the characteristics of the building blocks can be tuned pre-assembly,

$Re_6S_8Cl_2(PMe_3)_4$
H-L Gap = 2.25 eV
E.A. = 0.96 eV
I.E. = 6.00 eV

$Re_6S_8Cl_2(PMe_3)_3CO$
H-L Gap = 1.86 eV
E.A. = 1.66 eV
I.E. = 6.40 eV

$Re_6S_8Cl_2(PMe_3)_2(CO)_2$
H-L Gap = 1.70 eV
E.A. = 2.13 eV
I.E. = 6.82 eV

$Re_6S_8Cl_2(PMe_3)(CO)_3$
H-L Gap = 1.54 eV
E.A. = 2.69 eV
I.E. = 7.28 eV

$Re_6S_8Cl_2(CO)_4$
H-L Gap = 1.45 eV
E.A. = 3.21 eV
I.E. = 7.78 eV
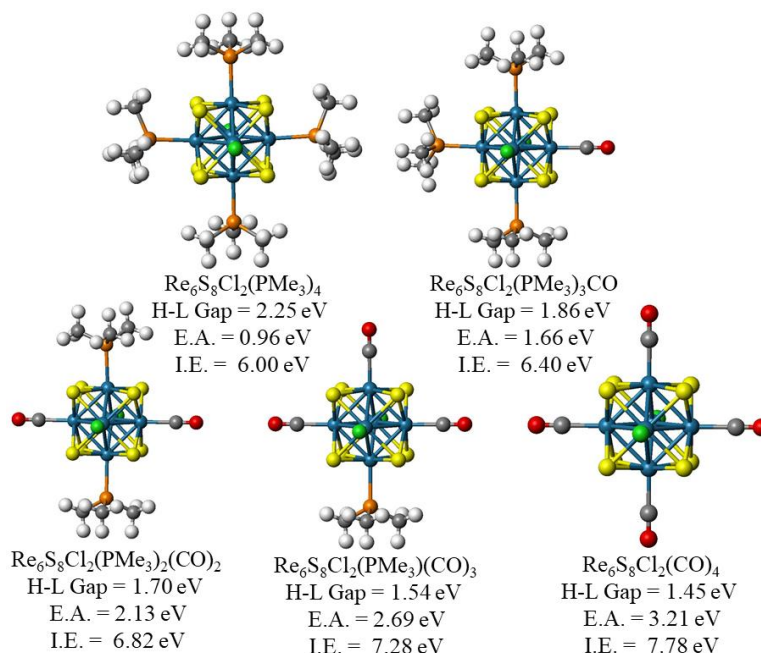
Figure. 4.1 The ground state structure, HOMO-LUMO gap, adiabatic electron affinity (E.A.), and adiabatic ionization energy (I.E.) of $Re_6S_8(Cl)_2(PMe_3)_m(CO)_n$

and the building blocks are highly stable. Figure 4.1 shows the ground state of $Re_6S_8Cl_2(L)_4$ clusters, L=CO, or trimethyl phosphine (PMe_3). These clusters have HOMO-LUMO gaps of 1.49-2.25 eV depending on the ligand, and Figure 2 shows the electronic levels of the cluster. $Re_6S_8(L)_6$ clusters are well-known to be highly stable with 84 valence electrons, so the additional 2 Cl ligands is needed to close the electronic shell.

Tuning the Electronic Spectrum of Metal-chalcogenide cluster.

By changing the ligand, superatomic clusters with closed electronic shells and large HOMO-LUMO gaps can be transformed into donors or acceptors while maintaining their electron shell closure. The electron affinity for $Re_6S_8Cl_2(CO)_4$ is 3.21 eV, making it an excellent electron acceptor despite its large gap, and the cluster's electron affinity is much larger than the 0.96 eV electron affinity of $Re_6S_8Cl_2(PMe_3)_4$. $Re_6S_8Cl_2(PMe_3)_4$ has an ionization energy of 6.00 eV, much lower than the 7.78 eV of $Re_6S_8Cl_2(CO)_4$, making the phosphine ligated cluster a significantly better electron donor.
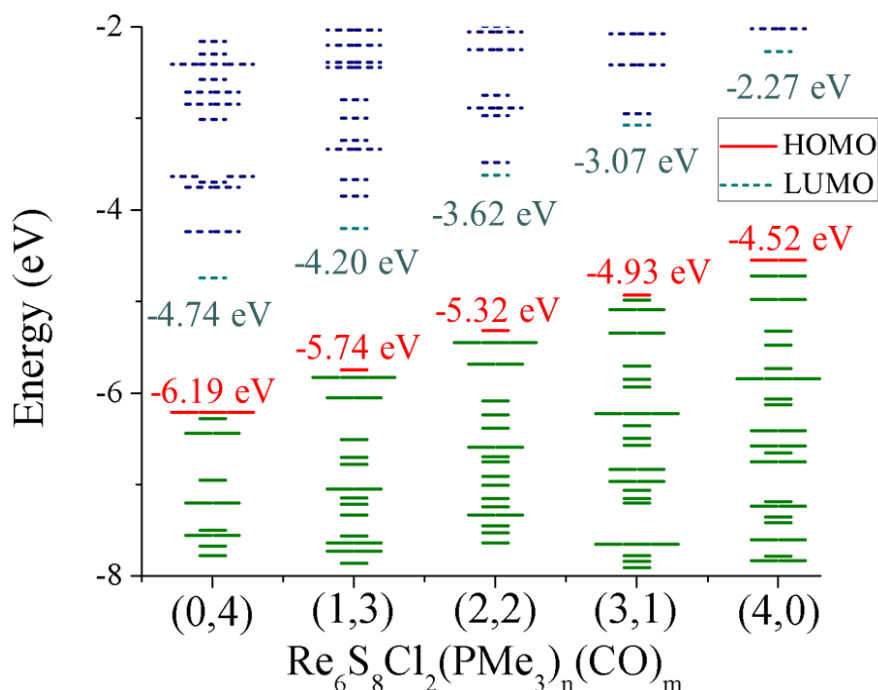
Figure 4.2 The electronic structure of $Re_6S_8(Cl)_2(PMe_3)_m(CO)_n$

The unusual feature is that irrespective of the combination of ligands, the ligated species always have a closed-shell electronic configuration with a high HOMO-LUMO gap, and that that the change in the electronic character is not associated with a change in the electron count.

Instead, the donor/acceptor transformation is due to a shift in the electronic spectrum that can be rationalized as ligands forming a coulomb well that surrounds the cluster and may raise or lower the energy of the states depending on the donor-acceptor characteristics of the ligand. This can be clearly seen in Figure 2, in which the absolute HOMO and LUMO of the ligated clusters are graphed. The electronic structure of the ligated clusters is effectively isoelectronic with each other, but their donor/acceptor characteristics are drastically different. In recent works, these findings have been confirmed by experiments.[26]

Cluster Fusion

Based on this concept that the ligand may transform a cluster from a donor to an acceptor, we fused two $Re_6S_8Cl_2(L)_4$ clusters. We consider the case where the PMe_3 ligand transforms one cluster into

A) $(Re_6S_8Cl_2(PMe_3)_3)_2$
H-L Gap = 2.00 eV
Dipole = 0.31 Debye

B) $(Re_6S_8Cl_2)_2(CO)_3(PMe_3)_3$
H-L Gap = 1.11 eV
Optical Gap 1.52 eV
Dipole = 11.2 Debye

C) $(Re_6S_8Cl_2(CO)_3)_2$
H-L Gap = 1.48 eV
Dipole = 0.30 Debye
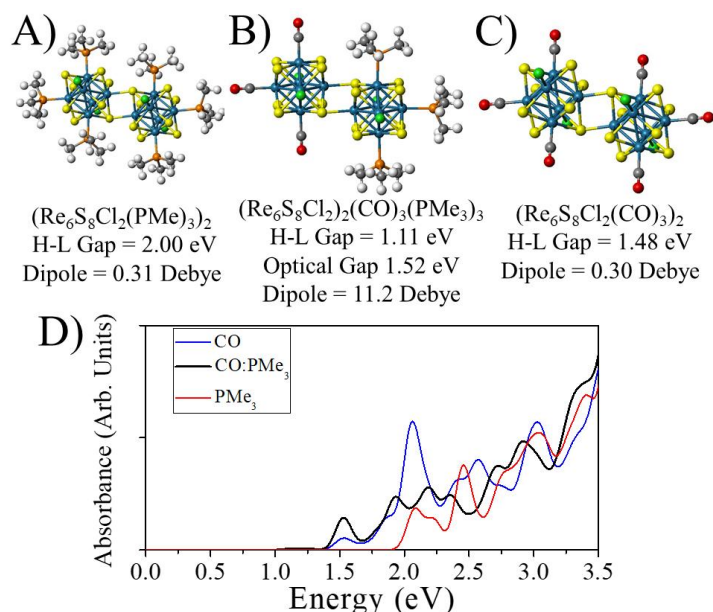
Figure 4.3 The structure, HOMO-LUMO gap, Optical Gap, and Dipole moment of A) $(Re_6S_8Cl_2(PMe_3)_3)_2$, B) $Re_6S_8Cl_2(CO)_3$: $Re_6S_8Cl_2(PMe_3)_3$, and C) $(Re_6S_8Cl_2(CO)_3)_2$. D) The calculated optical absorption spectra of $(Re_6S_8Cl_2(PMe_3)_3)_2$, $Re_6S_8Cl_2(CO)_3$: $Re_6S_8Cl_2(PMe_3)_3$, and $(Re_6S_8Cl_2(CO_3))_2$

The superatoms bind with the Sulfur of one cluster, binding the Re of the adjacent cluster. Hence, we decorated the stable $Re_6S_8Cl_2$ cluster with 3 CO and 3 PMe_3 ligands to form $Re_6S_8Cl_2(CO)_3$ and $Re_6S_8Cl_2(PMe_3)_3$ motifs. Figure 3 shows the structure of the three fused clusters or superatomic molecules with two $Re_6S_8Cl_2(PMe_3)_3$ motifs, B) the mixed $Re_6S_8Cl_2(PMe_3)_3:Re_6S_8Cl_2(CO)_3$ cluster, and C) two $Re_6S_8Cl_2(CO)_3$ clusters. The binding energies of the fused clusters are 1.67 eV, 1.80 eV, and 1.62 eV, respectively, showing that the fused clusters are reasonably stable. The enhanced binding energy of the fused clusters with mixed ligands is more stable due to the binding enhancement due to donor-acceptor pair forming.[24,37–41] The HOMO-LUMO gap of the clusters are 2.00 eV, 1.11 eV, and 1.48 eV, showing that they all have a significant gap.

The next question is whether the fusion of these superatomic clusters results in a strong internal electric field. The simplest way to test this is to find the dipole moment of the clusters. The dipole moment of the mixed cluster is 11.2 Debye, an extremely large dipole moment, while the moment of all PMe_3 and CO clusters are 0.31 and 0.30 Debye. This result suggests that there is an extremely strong internal electric field in the mixed cluster that causes a redistribution of charge, and this result is consistent with our donor-acceptor hypothesis. Next, we investigate the optical spectra of the cluster, using Time Dependent-Density Functional Theory (TD-DFT). We have checked our results with a TD-DFT calculation that includes a perturbative spin-orbit coupling and finds no significant excitation energy changes.[42] We find that the optical absorption of the mixed cluster is optically very weak for the HOMO-LUMO gap, and the optical gap is effectively 1.52 eV. This corresponds to the 8th lowest excitation, which is the first excitation with a non-negligible oscillator strength. The pure CO cluster has nearly the same optical gap of 1.50 eV, which corresponds to the lowest energy excited state, and the PMe_3 cluster has an optical gap of 2.03 eV. The results with the mixed cluster suggest that an excitation of the CO side of the cluster may strongly absorb light; however, the lower energy excitations that the cluster will decay to are optically weak, which should inhibit electron-hole pair recombination.[43,44]

A Cluster p-n junction

We now want to determine if the combined donor-acceptor units are genuine superatomic models of p-n junctions and whether they can separate electron-hole pairs. The combined superatomic molecule $Re_6S_8Cl_2(CO)_3$: $Re_6S_8Cl_2(PMe_3)_3$ is composed of an acceptor (CO) and donor (PMe_3) superatoms. The I.E. and E.A of 6.49 eV and 2.90 eV, which are in between the values of the clusters with all PMe_3 ligands, 5.86 eV, and 1.68 eV, and all CO ligands, 7.37 eV, and 3.54 eV. An analysis of the charge distribution indicates that there is a net charge flow of 0.14 e^- from the PMe_3 donor side to the CO acceptor. Next, we look at the charge distribution of the anionic and cationic clusters. The anionic cluster (Figure 4A), shows the excess charge is localized on the acceptor, CO side of the cluster, while in Figure 4B, the hole is localized on the PMe_3 side of the cluster. This demonstrates that the electron-hole pair is well-separated on the different sides of the fused cluster. Next, we want to know if the superatomic molecule (Figure 4C) has band bending at the interface, one of the hallmark characteristics of a p-n junction.
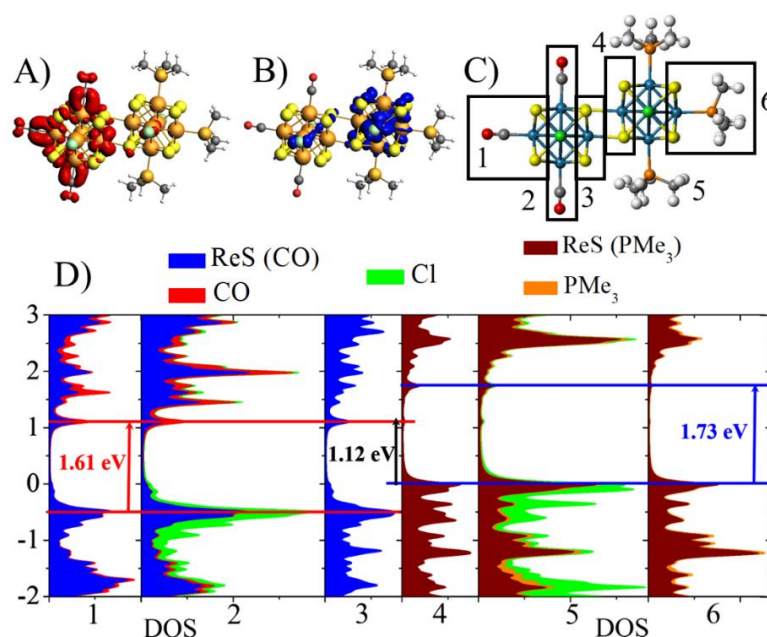
Figure 4.4 The structure of the A) Anionic, B) Cationic, and C) Neutral $Re_6S_8Cl_2(CO)_3Re_6S_8Cl_2(PMe_3)_3$. The isosurface indicates the excess charge, and electron hole. D) shows the density of states at different locations in the fused cluster. The position is indicated in part C.

Figure 4D shows the local density of states as a function of the position. The acceptor, CO, side of the cluster has effectively no density at the HOMO energy level, and the valence band energy is at -0.49 eV. The conduction band energy of the CO side is at 1.12 eV, with the gap on the CO side of the cluster being effectively 1.61 eV. On the PMe_3 side of the cluster, the valence band is at 0 energy, and the conduction band is at 1.73 eV. Thus the valence band of the PMe_3 side is 0.49 eV higher than the CO side, and the conduction band is 0.61 eV higher in energy. It is intriguing that both sides of the cluster have a local density of states with gaps of 1.61 and 1.73 eV, but the states of PMe_3 side are raised with respect to the CO side, a precise analog of band bending. This gives the look of a reduction of overall bandwidth, but is in fact, due to band bending.

Effect of an External Electric Field on the Fused Clusters

To examine the response of the electronic structure, an external field was applied to the mixed cluster, and the density of states and band energies are shown as a function of the voltage across the two-terminal Re atoms. The field strength corresponds to 2.57×10^9 V/m for the 2.6 V calculation, which is similar in strength to the 10^9 V/m electric fields found under an STM tip.[45]
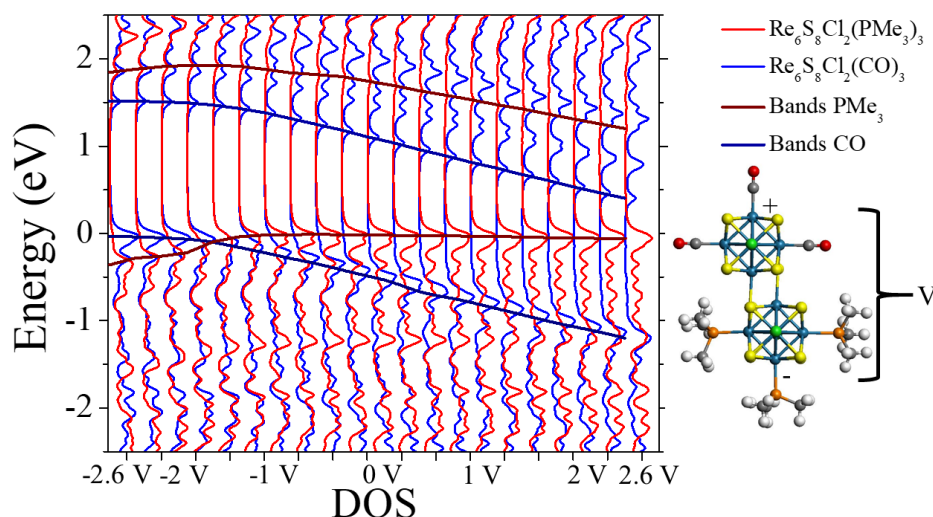
Figure 4.5 The density of states of the $Re_6S_8Cl_2(CO)_3$:$Re_6S_8Cl_2(PMe_3)_3$ cluster as a function of an electric field perpendicular to the cluster. The voltage across the terminal Re atoms are given, and the valence and conduction band energies of the CO and PMe_3 sides of the cluster are plotted.

Figure 5 shows the density of states as a function of the field. When the voltage across the terminal Re atoms is -1.55 V, the dipole moment approaches zero, and the HOMO-LUMO gap of the cluster increases to 1.47 eV. At a voltage of -1.55 V, the valence band of both sides of the cluster become aligned, causing this increase in the HOMO-LUMO gap. On the other hand, if the electric field is aligned as positive towards the acceptor CO, and negative towards the donor PMe_3, the electronic spectrum on the CO side of the fused cluster is lowered in energy versus the PMe_3 side. This leads to a reduction in the HOMO-LUMO gap, and the potential drop from the PMe_3 valence band to the CO valence band increases to 1.19 eV, versus the 0.49 eV at zero fields. This field-dependent shift indicates that the unit could be used as a rectifier in that it allows less resistance to the current in one direction. In contrast, the resistance (barrier due to difference in HOMO) increases as the field is applied in the opposite direction. It is essential to highlight that the current diode action is not due to any depletion layer as in conventional semiconductors but due to the misalignment of states in the two regions.

To determine if this concept can be further extended, we have examined the electronic structure of four fused $Re_6S_8Cl_2L_4$ clusters. In the tetramer cluster, the dipole moment has increased to 17.6 Debye. The HOMO-LUMO gap of the tetramer is 1.25 eV, the electron affinity increases from 2.86 eV for the dimer to 3.07 eV for the tetramer, and the ionization energy increases negligibly from 6.49 eV to 6.51 eV. The density of states reveals that the band bending across the cluster molecule has increased with the valence band on the far CO end of the cluster being 1.00 eV below the HOMO, while the energy of the valence band on the PMe_3 side is at the HOMO. Most of the band bending is at the junction, but there is a shift of 0.16 eV in the valence band across the outer and central CO ligated cluster and a shift of 0.34 eV in the valence band across the outer and central PMe_3 cluster. The shifts in the valence band are approximately the same. The separation and low oscillator strength suggest that electron-hole pair recombination will be inhibited. When we apply an electric field across the tetramer, we find that the bands are aligned when the voltage across the

terminal Re atoms are 1.7 V, slightly higher than the 1.55 V of the dimer. This shows that the concept may be extended to longer wires and may even be used to produce pnp or npn type junctions. In this work, we have focused on metal-chalcogenide species based on Re_6S_8 cores. However, our findings are fairly general. To show this, we investigated the $Co_6S_8(CO)_5$: $Co_6S_8(PMe_3)_5$ fused cluster. We find that the clusters bind by 2.45 eV and that the cluster has a dipole moment of 18.0 Debye, an even larger dipole than that for the Rhenium cluster. The cobalt cluster does not need Chlorine to close its electronic shell, so the dipole is larger. The HOMO-LUMO gap is only 0.29 eV, with the frontier orbitals being localized in the p-n junction. However, we found from the optical absorption spectra that the Cobalt cluster is unlikely to work for electron-hole pair excitation due to the presence of the defect states in the junction, and the concept may be applied to other ligated clusters.

4a.3. Conclusions

The dimer formed by fusing two metal-chalcogenide $Re_6S_8Cl_2(L)_4$ clusters with the charge donating ligands on one side and the charge accepting ligands on the other side acquires a substantial dipole moment and internal electric field. This internal electric field may easily separate electron-hole pairs because the electron is localized on the charge accepting CO side of the cluster. In contrast, the hole is localized on the charge donating PMe_3 side of the cluster. Because of this strong internal electric field, the electron and hole are separated, inhibiting recombination. The fused clusters behave much like a cluster p-n junction, with the ligands acting as charge transfer dopants. An external electric field may realign the levels, and the response suggests that these fused clusters may behave much like a diode. The fused clusters may be extended into nanowires, opening the possibility of more complicated pnp and npn type junctions using this strategy.

Furthermore, this concept may be applied to other ligated clusters. However, the presence of defect states in the cluster junction may prevent electron-hole separation, so the choice of the cluster

requires care for applications related to photovoltaics. Additionally, such an atom-precise material synthesis is quite challenging; however, such fused clusters have been successfully synthesized.[11] The use of multi-dentate ligands may be used to encapsulate one side of the cluster, greatly enhancing the binding. Another strategy would be to use a surface as a ligand. A surface such as a metal-chalcogenide or a graphene surface may act as a donor or acceptor, and free ligands may serve as the acceptor or donor. These results reveal an alternative strategy for forming and engineering internal electric fields at the scale of a single nanometer.

Section 4b

A Magnetic Superatomic Dimer with an Intense Internal Electric Dipole and Magnetic Moment

Continuing with the dimer formation, the Fe_6S_8-based clusters formed a dimer $[(CO_5)(Fe_6S_8)_2(PMe_3)_5]$ with a gigantic magnetic moment and electric dipole moment. Such dimers can be valuable entities for spintronics-related applications.

4b.1. Introduction

The electronic and magnetic properties of ligand decorated Fe_6S_8 cluster, and fused superatomic dimer are investigated using the first-principles density functional theory. It is shown that the redox properties of the Fe_6S_8 cluster can be efficiently controlled by varying the nature of the attached ligands. Donor ligands such as phosphines reduce the ionization energy of the Fe_6S_8 cluster, whereas the acceptor ligands such as CO increase the electron affinity. Such variation in the redox properties of the Fe_6S_8 cluster is the result of

the ligand-induced shift in the cluster's electronic levels keeping the occupation number mostly unaffected, leading to a marginal change in the spin magnetic moment of the cluster. Combining two identical Fe_6S_8 clusters decorated with unbalanced ligands results in a superatomic dimer with a massive dipole moment and a large spin magnetic moment. Donor ligands on one side and the acceptor ligands on the other side cause significant inter-cluster charge transfer across the superatomic dimer. The resulting superatomic dimer offers an exciting motif for spintronics-related applications.

Recent developments in synthetic chemical techniques that allow their facile synthesis in solutions and their assembly into solids have attracted considerable interest in ligated metal-chalcogenide clusters.[46–51] These ligated species are highly stable, can be prepared in solutions, and have charge donor and acceptor characteristics, allowing them to form solids with complementary units maintaining individual clusters' identity.[49–53] They represent a new class of superatoms, some of which have open electronic shells that can lead to magnetic materials.[54] This exciting class of solids has been extensively investigated by Roy, Nuckolls, and co-workers[49–53]. They have successfully synthesized a wide range of cluster-based solids from an assembly of superatoms acting as electron donors that exchange charge with C_{60} counterions to form ionic materials. Roy et al. reported many such solids, including those based on $[Co_6Se_8(PEt_3)_6]$, $[Cr_6Te_8(PEt_3)_6]$, $[Re_6S_8Cl_2(PEt_3)_4]$, and $[Ni_9Te_6(PEt_3)_8]$.[49–53] The metal chalcogenide-based clusters are typically fully ligated by phosphine ligands such as tri-ethylphosphine (PEt_3) connected to the metal atoms, thus protecting the metallic core. The phosphine-ligated clusters become excellent charge donors and combine with the charge acceptor C_{60} to form superatomic ionic solids similar to CdI_2 or $NaCl$.[51] The resulting solids offer exciting properties, including enhanced conductivity, ferromagnetism, and unusual magneto-optical properties.[50–52] Materials in which the metal-chalcogen clusters can directly bind to each other produce dimeric or extended structures, which have also been synthesized, offering the opportunity for extended semiconducting materials constructed from cluster building blocks.[11,55–57] This includes dimeric structures of $([Co_6Se_8](PEt_3)_5)_2$ and extended sheets of $[Re_6S_8Cl_2]$ clusters. These results demonstrate that exquisite control of superatomic solids is possible, including superatomic dimer structures

Iron-sulfur clusters are also known for their reversible electron transfer chemistry and are marked by high spin multiplicity making them behave as small magnetic units.[58–60] Thus, understanding how redox properties can be controlled without quenching the magnetic characteristics is an essential undertaking with extensive applications including spintronics materials.[61–64] In this work, we have investigated the nature of electronic states and the magnetic properties of $Fe_6S_8L_n$ (L= ligands) clusters. The magnetic and electronic properties of the Fe_6S_8 cluster are found to be controlled by changing the number and the nature of the attached ligands.[64–67,26,68] Tri-methylphosphine (PMe_3) is used as a donor ligand, while carbon monoxide (CO) serves as an acceptor ligand. The bare Fe_6S_8 cluster is observed to be magnetic with a high spin magnetic moment. The addition of donor ligands reduces the ionization energy of clusters with a minor reduction in the magnetic moment. The ligated clusters' donor-acceptor nature becomes apparent when a fully ligated cluster $Fe_6S_8(PMe_3)_6$ is investigated through the successive replacement of PMe_3 ligands by CO ligands. The sequential replacement of PMe_3 ligand by CO leads to an increment in the electron affinity and the ionization energy of the cluster. Microscopic analysis reveals that the calculated changes in redox properties are driven by raising or lowering the electronic states without changing the respective occupation of the minority or majority spins levels. The effect of the charge transfer ligands can be thought of as creating a Coulomb potential well that shifts the electronic levels without changing the exchange splitting or the moment in the majority of cases.[69] This unusual ability of ligands to control the location of the electronic levels leads to intriguing possibilities. We have shown that by combining two identical bare clusters and decorating them with different kinds of ligands, one can create an interface with units where the electronic states on individual clusters are misaligned, resembling a semiconductor junction.[70,71] When the superatomic dimer is formed, the charge transfer across the clusters on different sides leads to align the highest occupied molecular orbital, similar to the alignment of Fermi energy in the p-n junctions. What is unique in this case is that the alignment does not destroy the magnetic features leading to a superatomic molecule with a large magnetic moment and a massive electrical dipole moment that could be utilized to design a spin polarizer.[72]

76

4b.2. Results and Discussion

Controlling the HOMO, LUMO, and Exchange Splitting via Ligands

Our discussion starts with a brief review of how PMe_3 ligands can control the position of energy levels. The ground-state structure of the Fe_6S_8 cluster, which has a spin magnetic moment of 8 μ_B, consists of an octahedron of 6 Fe sites with faces decorated with 8 S atoms. Figure 4.6 shows the ground state geometries of $Fe_6S_8(PMe_3)_n$ clusters (n = 0-6. For the electronic properties, we have monitored the progression of **(1)** HOMO-LUMO (HL) gap: the energy difference between the highest occupied molecular orbital (HOMO) and the lowest unoccupied molecular orbital (LUMO), **(2)** the adiabatic ionization potential (AIP), and **(3)** adiabatic electron affinity (AEA).
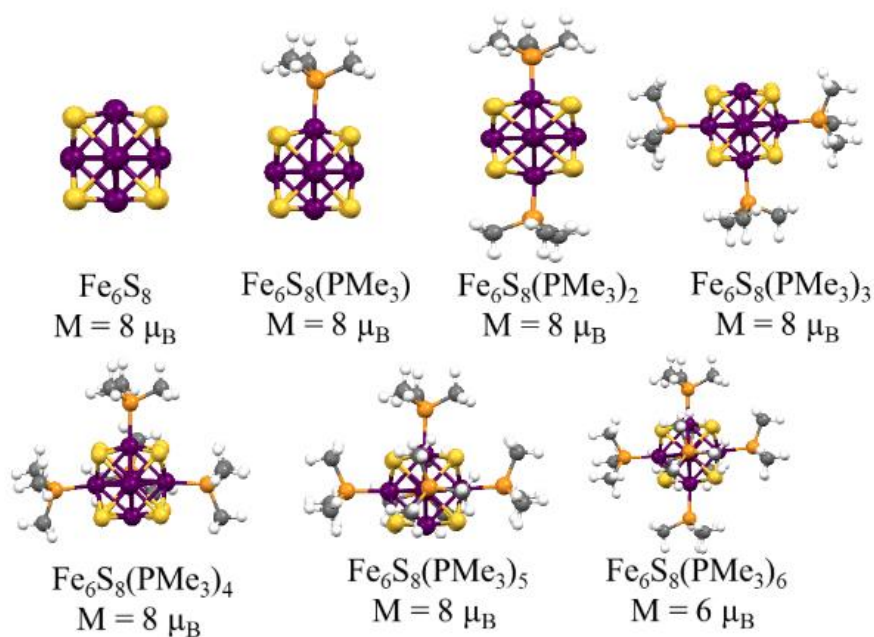
Figure 4.6. Ground state structures of $Fe_6S_8(PMe_3)_n$ (n = 0-6). The net magnetic moments for each system are given in μ_B.

Similarly, we have also investigated the progression in the magnetic moment with the subsequent addition of PMe_3 ligands, shown in Figure 4.7(a). One would expect that the addition of charge donor ligands changes the magnetic moment; [73–76]; however, the overall magnetic moment remains constant until the addition of the fifth PMe_3 ligand.
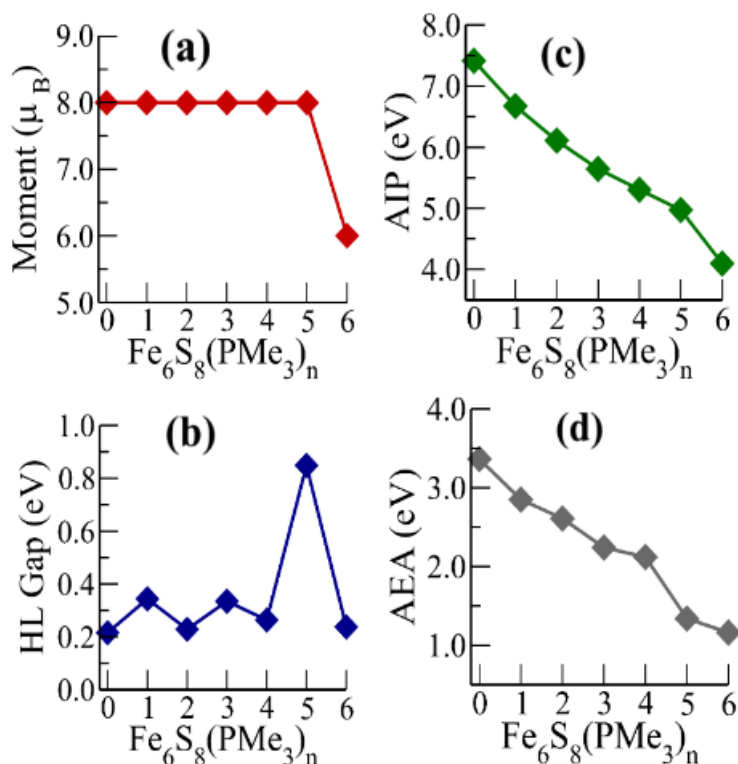
Figure 4.7. (a) Magnetic moment (b) HOMO-LUMO (HL) Gap (c) Adiabatic Ionization

Potential (AIP), and (d) Adiabatic Electron Affinity (AEA) for $Fe_6S_8(PMe_3)_n$ (n = 0-6).

The sixth ligand addition reduces the moment to 6 μ_B from 8μ_B, as shown in Figure 4.7(a). The HOMO-LUMO gap varies between 0.22-0.85 eV, and the cluster $Fe_6S_8(PMe_3)_5$ is found to possess the largest HOMO-LUMO gap of around 0.85 eV, as shown in Figure 4.7(b). It is unique to have a stable cluster with one metal (Fe) site unligated, especially with a large spin magnetic moment. Such clusters provide some intriguing opportunities, e.g., such stable clusters can be combined to form a fused dimer and can also be used as n/p type dopants on 2D semiconducting surfaces.[77] The AIP monotonically decreases with the addition of the ligands, as shown in Figure 4.7(c), finally attaining a value of 4.09 eV, the IP of cesium (3.9 eV). Figure 4.7(d) shows a parallel decrease in the AEA, achieving a low value of 1.16 eV for $Fe_6S_8(PMe_3)_6$. The monotonic decrease in the AIP and AEA while maintaining the constant spin moment until the 5th ligand implies that the variations in electronic properties are probably not due to the filling of the electronic states. The alteration of HOMO and LUMO levels with the addition of the PMe_3 ligands for both alpha and beta channels are shown in Figure 4.8. The major effect of adding PMe_3 ligands is an upward shift in the

electronic levels. Interestingly, the shift is observed for both spin states; however, the majority and minority spin states undergo slightly different shifts that change the exchange splitting of the system. The reduction in the magnetic moment of $Fe_6S_8(PMe_3)_6$ is associated with the lifting of a minority spin state to the occupied manifold. To understand the change in the magnetic moment during the transition from
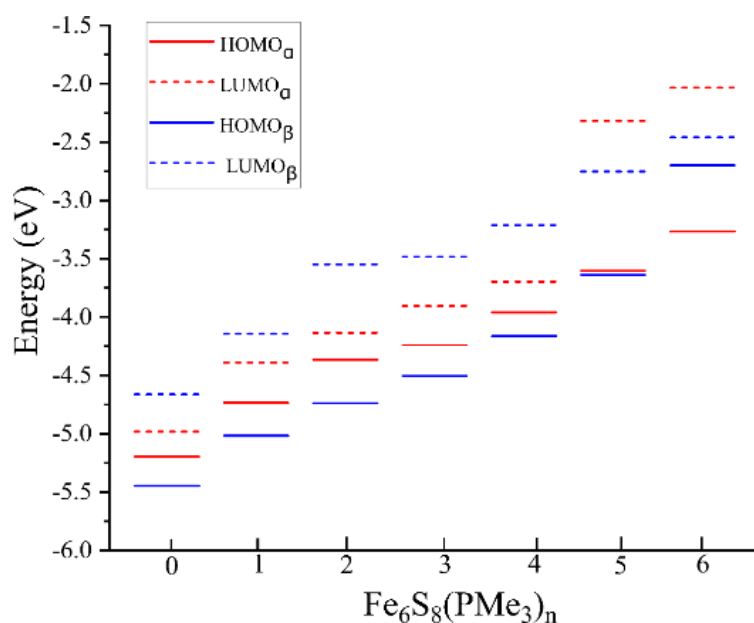
Figure 4.8 HOMO and LUMO levels in alpha and beta channels of **$Fe_6S_8(PMe_3)_n$** (n = 0-6). The red solid and dashed lines represent HOMO and LUMO levels in α-channel while the blue solid and dashed lines represent HOMO and LUMO levels in the β-channel.

$Fe_6S_8(PMe_3)_5$ to $Fe_6S_8(PMe_3)_6$, we investigate the similar evolution in going from $Fe_6S_8(CO)_5$ to $Fe_6S_8(CO)_6$ cluster. Both the PMe_3 and CO-based systems exhibit a similar change in a magnetic moment from 8 μ_B to 6 μ_B with the final (6th) ligand. Both $Fe_6S_8(PMe_3)_5$ and $Fe_6S_8(CO)_5$ have relatively large HOMO-LUMO gaps of 0.84 eV and 0.68 eV, respectively, especially for the high spin clusters. Besides, the C_{4v} symmetry of the CO ligated clusters allows for a simpler analysis of the cluster orbitals. Starting with $Fe_6S_8(CO)_5$ in C_{4v} symmetry, we find a half-occupied cluster orbital with A_1 symmetry indicated in red in Figure 4.9 (a) (I). This orbital is primarily constructed from the $3d_z^2$ orbital of the unligated Fe-atom, and it is occupied in the The destabilized $17A_1$ state becomes unoccupied in the majority spin channel;

hence the HOMO state is now an A_2 orbital of the minority channel that becomes occupied after the complete attachment of the CO ligand, as shown in Figure 4.9(a) (II-III). The 1-electron energy level diagram given in Figure 4.9(a) (III) shows that the A_1 orbital (in a red box) in the α-channel gets destabilized and becomes unoccupied with the beta-channel HOMO level becoming filled. Hence, the magnetic moment decreases spin majority channel and unoccupied in the spin minority channel.
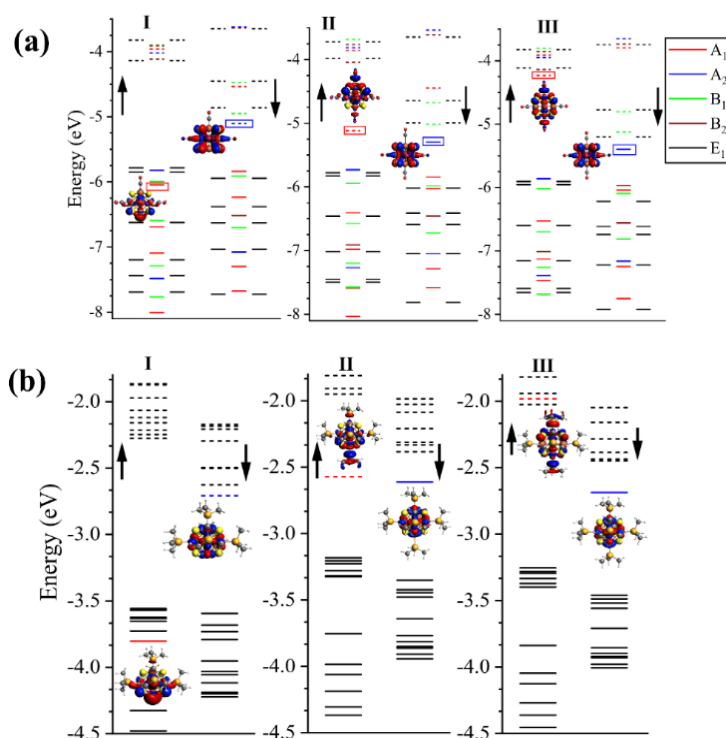
Figure 4.9 One-electron energy levels of (a) (I-III) $Fe_6S_8(CO)_5$, when the sixth CO ligand is brought closer to $Fe_6S_8(CO)_5$ until $Fe_6S_8(CO)_6$ is formed in C_{4V} symmetry. The solid and dashed lines represent the occupied and unoccupied energy states respectively. The solid red box shows the raising of a particular energy state(A_1) in α-channel while the blue box marks the state(A_2) which finally gets occupied in the β-channel for $Fe_6S_8(CO)_6$. (b) One-electron energy levels of (I-III) $Fe_6S_8(PMe_3)_5$, when the sixth PMe_3 ligand is brought closer to $Fe_6S_8(PMe_3)_5$ until $Fe_6S_8(PMe_3)_6$ is formed.

Next, as a CO ligand is brought in with a bond distance that is 0.5 Å longer than the expected Fe−CO bond length, the half-filled $3d_z^2$ orbital is pushed up in energy as seen in Figure 4.9(a)(II) due to the crystal-field effect, where the charge on the CO destabilized this orbital. by 2 μ_B. A similar process occurs with PMe$_3$ ligands; we observe the raising of the states shown by the solid red line in Figure 4.9(b)(I) in α-channel. The sixth PMe$_3$ ligand is brought closer to the Fe$_6$S$_8$(PMe$_3$)$_5$ cluster until it forms Fe$_6$S$_8$(PMe$_3$)$_6$. The LUMO in the minority channel shown by the blue line in Figure 4.9(b)(I) gets occupied at the expense of the destabilization of the α-channel state depicted by red color, as can be seen in Figure 4.9(b)(II-III). Therefore, the magnetic moment is reduced by 2 μ_B.

The stability of Fe$_6$S$_8$(PMe$_3$)$_5$ can be explained using the cationic cluster [Fe$_6$S$_8$(PEt$_3$)$_6$]$^+$, which was observed to have an unusually stable oxidation state with a large spin magnetic moments of approximately 7 μ_B and high symmetry.[78] Again, we can use Fe$_6$S$_8$(CO)$_5$ and [Fe$_6$S$_8$(CO)$_6$]$^+$ clusters as their symmetry provides a more accessible analysis of the cluster orbitals. The electronic structures in Figure 4.10 show that the electronic structures of Fe$_6$S$_8$(CO)$_5$ and [Fe$_6$S$_8$(CO)$_6$]$^+$ are almost identical and that [Fe$_6$S$_8$(CO)$_6$]$^+$ has O$_h$ symmetry. Furthermore, we calculated the deformation coefficient[79], Δ, which offers the overall symmetry of the system. The spherical cluster or octahedral cluster will have Δ=1, whereas a deformed oblate structure will have Δ<1. A planar structure will be marked by Δ=0. We hypothesize that if the stability in the metal-chalcogenide cluster is due to a shell filling, then the symmetry will be high, and the deformation coefficient will be 1. However, if the stability is due to a Jahn-Teller distortion or due to mixed oxidation states of Fe, then the sites will be inequivalent, and the deformation coefficient will move away from 1.[79] The deformation coefficient of Fe$_6$S$_8$(CO)$_5$ is found to be close to 1, similar to [Fe$_6$S$_8$(CO)$_6$]$^+$, while Fe$_6$S$_8$(CO)$_4$ and Fe$_6$S$_8$(CO)$_6$ have deformations away from the symmetry. Note that in this argument, [Fe$_6$S$_8$(CO)$_6$]$^+$ is stabilized by the filling of the electronic shells delocalized over the cluster, so the shell filling should correspond to the symmetric cluster with a deformation coefficient of

1, confirmed by stable oxidation state in the experiments, and the high symmetry of $[Fe_6S_8(CO)_6]^+$. Also, the spin moment on all of the atoms should be identical. Likewise, we found $\Delta \sim 1$ for $Fe_6S_8(PMe_3)_5$ and $[Fe_6S_8(PMe_3)_6]^+$. However, $Fe_6S_8(PMe_3)_5$ has a high spin magnetic moment of 8 μ_B. So, what is occurring when the ligand is removed from the $Fe_6S_8(CO)_6$ cluster to form $Fe_6S_8(CO)_5$, an empty A_1 antibonding state in the spin alpha channel that CO destabilized gets filled after the removal of the ligand. So, we have magnetic clusters with a large HOMO-LUMO gap in both $Fe_6S_8(CO)_6^+$ and $Fe_6S_8(CO)_5$, however the spin of $Fe_6S_8(CO)_5$ increases from 7 to 8 μ_B because of the occupation of this extra d_z^2 state on the unligated
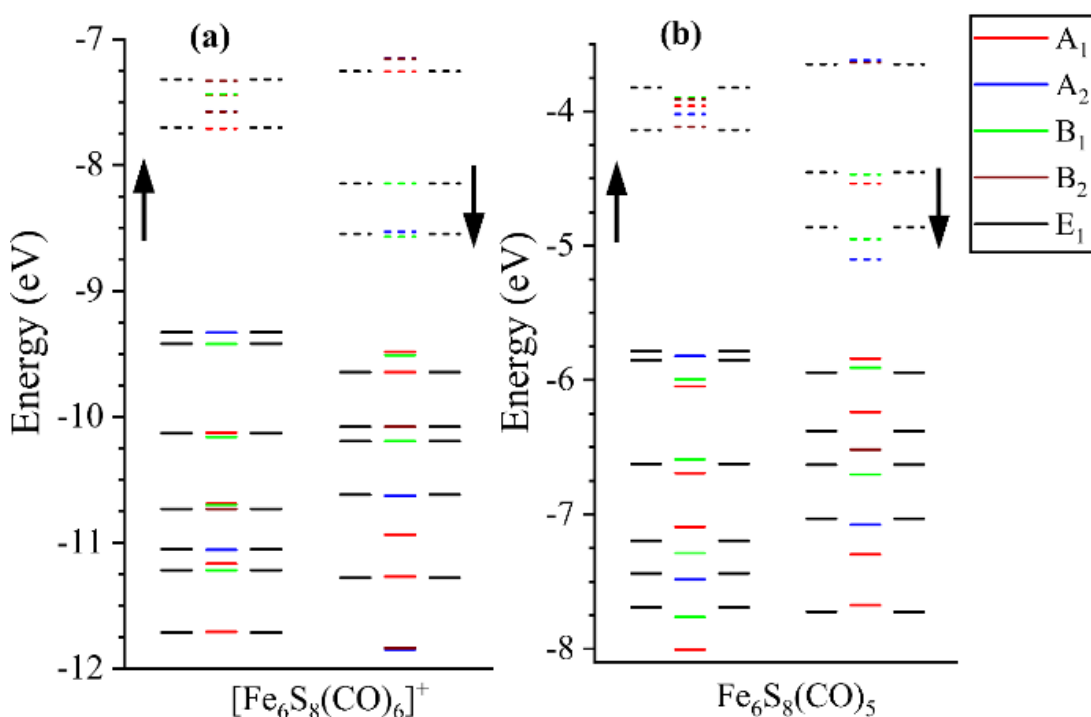
Figure 4.10 One-electron energy levels of (a) $[Fe_6S_8(CO)_6]^+$ (b) $Fe_6S_8(CO)_5$ in C_{4V} symmetry. The solid and dashed lines represent the occupied and unoccupied energy states respectively. The up- and down-arrow represent the majority and minority spin-channels respectively.

Fe atom. The origin of the high stability of $Fe_6S_8(PMe_3)_5$ is confirmed by its spatial symmetry, the high spin state of 8 μ_B, and its substantial HOMO-LUMO gap. The donor-acceptor nature of PMe_3 and CO ligands becomes more evident when PMe_3 ligands of a fully ligated $Fe_6S_8(PMe_3)_6$ cluster is subsequently replaced by CO ligands.

Properties of Fe₆S₈(PMe₃)₆₋ₙ(CO)ₙ Clusters (n=0-6)

The charge donor and acceptor features of the ligated cluster depend on the nature of the attached ligands. One of the quantities of interest is the variation in a fully ligated cluster's electronic properties as the acceptor ligands (CO) successively replace the donor ligands (PMe₃). Figure 4.11 shows the ground-state structures of the $Fe_6S_8(PMe_3)_{6-n}(CO)_n$ clusters. Note that we have explored all possible sites for the CO ligands

$Fe_6S_8(PMe_3)_6$
M = 6 μ_B

$Fe_6S_8(PMe_3)_5(CO)$
M = 6 μ_B

$Fe_6S_8(PMe_3)_4(CO)_2$
M = 6 μ_B

$Fe_6S_8(PMe_3)_3(CO)_3$
M = 6 μ_B

$Fe_6S_8(PMe_3)_2(CO)_4$
M = 6 μ_B

$Fe_6S_8(PMe_3)(CO)_5$
M = 6 μ_B

$Fe_6S_8(CO)_6$
M = 6 μ_B
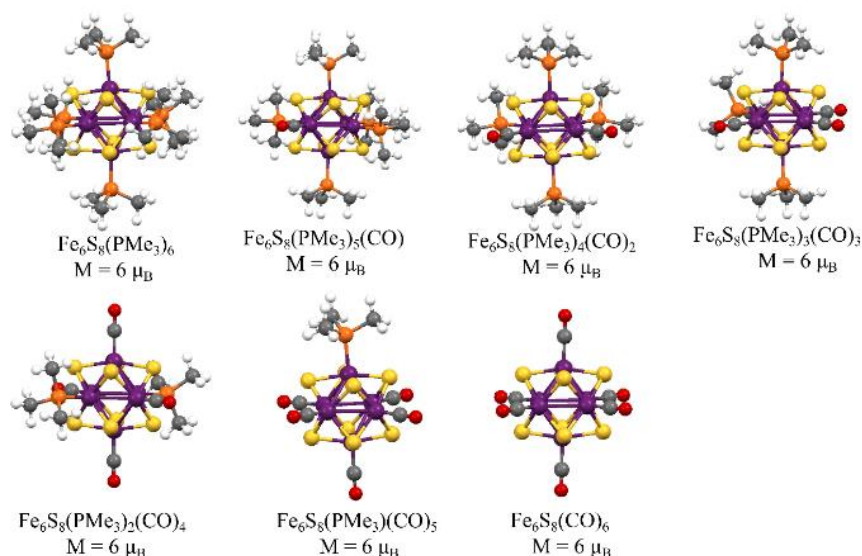
Figure 4.11 Ground state structures of $Fe_6S_8(PMe_3)_{6-n}(CO)_n$ (n = 0-6). The net magnetic moments for each system are given in μ_B.

to partially replace PMe₃ ligands. Irrespective of the number of PMe₃/CO ligands in fully ligated clusters, they always exhibit the same magnetic moment of 6 μ_B. The replacement of PMe₃ by CO leads to a monotonic increase in the AIP and AEA, as shown in Figure 4.12(a). The AIP increases from a low value of 4.09 eV, which is reminiscent of alkali metals' low ionization potential, to a higher value of 7.06 eV. The AEA is increased from 1.16 eV to 3.68 eV, close to the electron affinity of a Cl atom.[80]
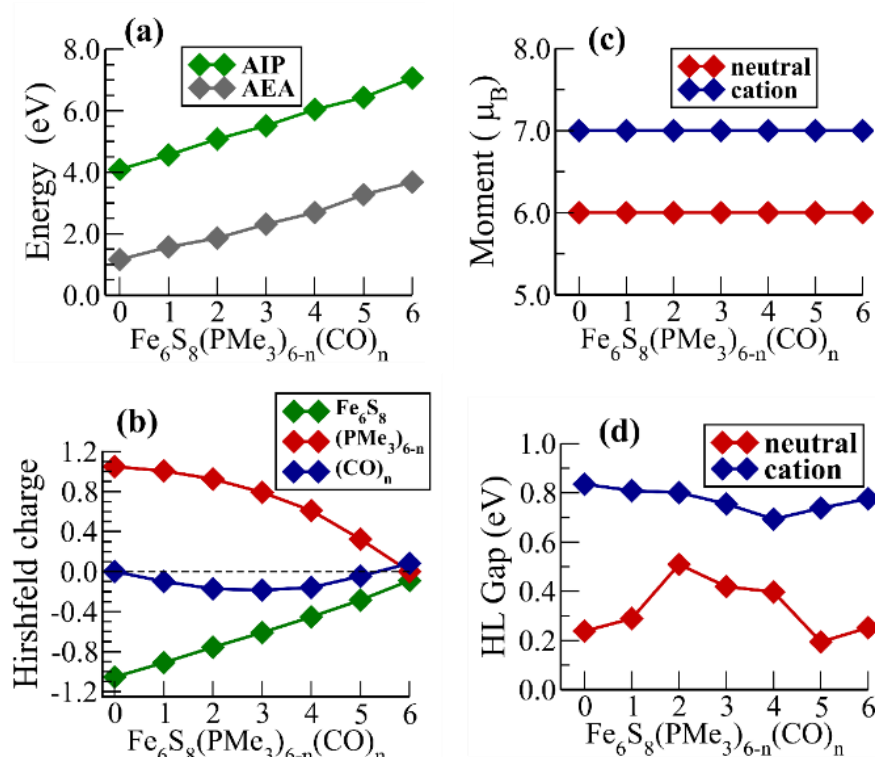
Figure 4.12 (a) Adiabatic Ionization Potential (AIP) and Adiabatic Electron Affinity (AEA) for $Fe_6S_8(PMe_3)_{6-n}(CO)_n$ (n = 0-6). (b) Variation in Hirshfeld charge[50] in $Fe_6S_8(PMe_3)_{6-n}(CO)_n$ (n = 0-6). (c) Variation in Magnetic moment and (d) HOMO LUMO Gap for neutral and cationic clusters of $Fe_6S_8(PMe_3)_{6-n}(CO)_n$ (n = 0-6).

We confirmed the electronic spectrum's lowering when CO replaces PMe_3 by analysis of 1-electron energy level. There are some variations in the HOMO-LUMO gap; however, the magnetic moment stays constant. To show that the effect is general, we also carried out similar calculations on singly ionized clusters $[Fe_6S_8(PMe_3)_{6-n}(CO)_n]^+$. The magnetic moment remained constant while the HOMO-LUMO gaps slightly varied but with larger values, as shown in Figures 4.12(c) and 4.12(d), respectively. These cationic systems with larger HOMO-LUMO gaps and the magnetic moment of 7 μ_B confirm the stable high spin clusters discussed in the previous section.

Finally, the Hirshfeld charge[81] plot in Figure 4.12(b) shows that CO ligands exhibit a moderately weak charge accepting nature in $Fe_6S_8(PMe_3)_{6-n}(CO)_n$ for n = 1-6. As the number of the CO ligands are subsequently increased, the overall negative charge on the Fe_6S_8 is observed to decrease. This is because CO ligand acts as a σ donor (base) as well as a π acceptor (acid) when it binds to a metal center.[82,83] The Fe atoms can easily donate charge to the empty π* orbital of CO via $d_{Fe} \rightarrow \pi_{CO}*$ back donation as they are energetically very close.[82,83] In PMe$_3$ ligands, such back-donation is not possible, since the sigma antibonding (σ*) orbitals of P−C bonds are energetically much higher compared to the filled 'd' orbitals of the metal centers.[83] Thus, the observed effect of $(CO)_n$ is synergistic and depends on which of the electronic effect (σ donor or π acceptor) dominates over the other. It is evident from the plot (Figure 4.12(b)), that the maximum negative charge accumulation on $(CO)_n$ is observed when the numbers of PMe$_3$ and CO ligands are equal, i.e., at n= 3.

Magnetic Superatomic Molecule (PMe$_3$)$_5$(Fe$_6$S$_8$)$_2$(CO)$_5$

Next, we investigated the stability and structure of a fused dimer formed by combining two $Fe_6S_8(L)_5$ clusters. There are two possibilities for the fused superatomic dimer: a dimer where the ligands are all the same and an unbalanced dimer where acceptor CO ligands are on one Fe_6S_8 cluster, while donor PMe$_3$ ligands are on the other Fe_6S_8 cluster. The dimers with only PMe$_3$ ligands are found to have binding energies (BE) of 0.38 eV, HOMO-LUMO gap of 0.08 eV, and total spin magnetic moment of 14 u_B while the binding energy, HOMO-LUMO gap, and the total spin magnetic moment for the only CO-ligated dimers are found to be 0.88 eV, 0.26 eV and 12 μ_B respectively. It is observed that the large HOMO-LUMO gaps of the monomeric clusters, $Fe_6S_8L_5$ are reduced by the fusion. The weak binding between the monomers is due to the relatively high stability of the $Fe_6S_8(L)_5$ clusters. Furthermore, both the dimers also possess negligible dipole moments, showing minimal charge transfer between the monomers. The high spin magnetic moment of the dimers suggests that such fused superatomic clusters may be attractive

motifs for spintronics applications; however, the dimer with unbalanced ligand may be even more interesting because of the possibility of charge transfer across the junction between the dimer.
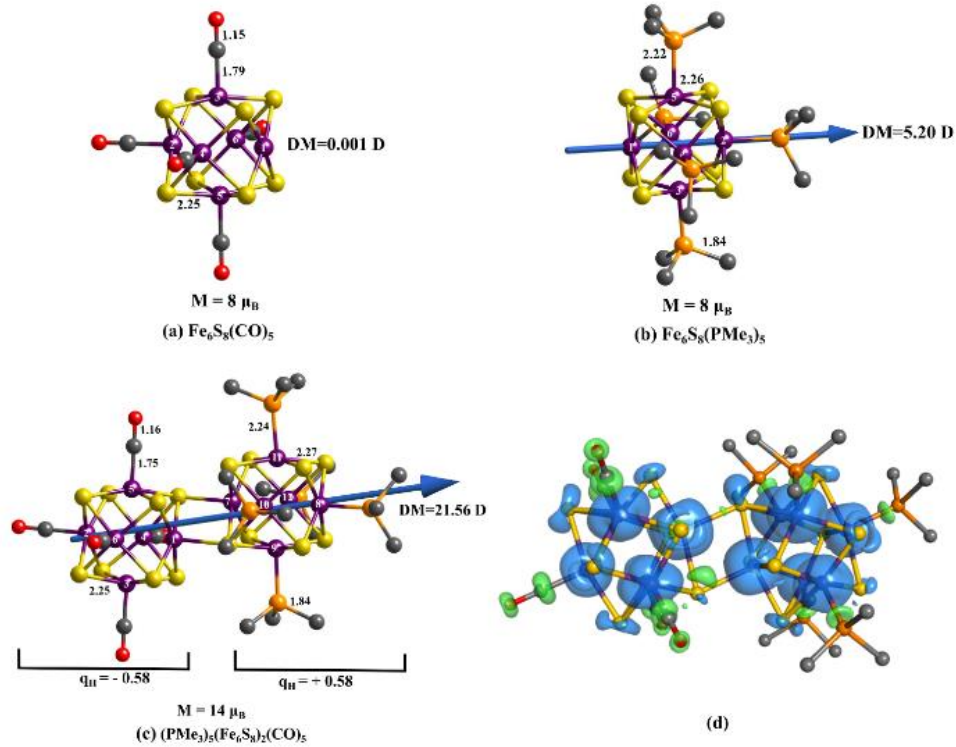
Figure 4.13 The ground state optimized structures of (a) $Fe_6S_8(CO)_5$ (b) $Fe_6S_8(PMe_3)_5$ and (c) $(PMe_3)_5(Fe_6S_8)_2(CO)_5$. The dipole and magnetic moment values are also shown. The important bond lengths are in Å. Figure (d) shows the spin density isosurface for $(PMe_3)_5(Fe_6S_8)_2(CO)_5$.

For this reason, we investigated a fused dimer, $(PMe_3)_5(Fe_6S_8)_2(CO)_5$, consisting of a Fe_6S_8 cluster ligated with CO ligands on one side and the PMe_3 ligated cluster on the other side. Figure. 4.13(a), 4.13(b) and 4.13(c) show the optimized ground state structures, dipole moment, and spin magnetic moment of the $Fe_6S_8(CO)_5$, $Fe_6S_8(PMe_3)_5$, and $(PMe_3)_5(Fe_6S_8)_2(CO)_5$, respectively. The electronic and magnetic properties of the monomeric and dimeric clusters are listed in Table 4.1. The dimer with unbalanced ligands has a spin magnetic moment of 14 u_B and has a relatively larger binding energy of 1.58 eV. We calculated the binding energy of the dimer using the expression,

$$B.E. = E_{Fe_6S_8(CO)_5} + E_{Fe_6S_8(PMe_3)_5} - E_{(PMe_3)_5(Fe_6S_8)_2(CO)_5} \quad (4.1)$$

where $E_{Fe_6S_8(CO)_5}$, $E_{Fe_6S_8(PMe_3)_5}$, and $E_{(PMe_3)_5(Fe_6S_8)_2(CO)_5}$ are the total energies of the $Fe_6S_8(CO)_5$, $Fe_6S_8(PMe_3)_5$, and $(CO)_5(Fe_6S_8)_2(PMe_3)_5$ clusters, respectively. The binding energy of the dimer with the unbalanced ligand is significantly larger than for the dimers with the same ligands on both sides of the cluster due to the enhanced charge transfer. We find the net charge on the donor PMe_3 side of the dimer is +0.58 e-, and the charge on the acceptor CO side is -0.58 e-. This confirms that the PMe_3 is causing one side of the cluster to act as a donor, and the CO is causing its side of the cluster to act as an acceptor. This results in a large dipole moment of 21.56 D. The HOMO of the monomeric PMe_3 is 2.2 eV higher than that of the CO, lying at -3.59 and -5.78 eV, as shown in Table 1. The HOMO of the fused dimer lies approximately in the middle at -4.26 eV. The HOMO of the dimer is an antibonding state between the two monomers, and this orbital is spread across the junction.
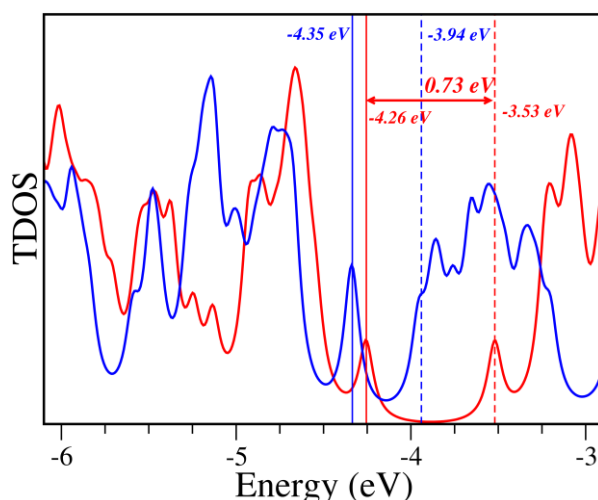
Figure 4.14 The total density of states (TDOS) for $(PMe_3)_5(Fe_6S_8)_2(CO)_5$. Solid and dashed lines represent the occupied and unoccupied energy levels respectively. The red solid and dashed lines represent HOMO and LUMO levels in the alpha-channel while blue solid and dashed lines represent HOMO and LUMO levels in the beta-channel.

The bond formation and charge rearrangement in dimer across the monomeric units lead to a significant change in the electronic and magnetic features compared to the individual species. The dimer has a spin magnetic moment of 14 μ_B. The 14 unoccupied orbitals in β-channel and their corresponding counterparts

occupied in α-channel are detectable. Figure 4.14 shows the total density of states (TDOS) for both spins in $(PMe_3)_5(Fe_6S_8)_2(CO)_5$. Note that the majority spin states are marked by a gap of around 0.73 eV above the HOMO. On the other hand, the minority spin states have an appreciable density of states in the gap region following the HOMO. This indicates that any electrical transport will be polarized by carriers from the minority spins. The situation is like half-metallic ferromagnets, where the conducting carriers are spin-polarized.

TABLE 4.1 Electronic and Magnetic Properties of $Fe_6S_8(CO)_5$, $Fe_6S_8(PMe_3)_5$, and $(PMe_3)_5(Fe_6S_8)_2(CO)_5$ clusters. The x, y, and z components of the dipole moment are included within parenthesis. *

System	Magnetic Moment (μ_B)	Dipole Moment (Debye)	Electronic Properties (eV)				
			α-spin	β-spin	Both spin	AIP	AEA
$Fe_6S_8(CO)_5$	8	0.00 (0.0, 0.0, 0.0)	H= -5.78 L= -4.14 Δ_{H-L}= 1.64	H= -5.84 L= -5.10 Δ_{H-L}= 0.74	H= -5.78 L= -5.10 Δ_{H-L}= 0.68	7.48	3.59
$Fe_6S_8(PMe_3)_5$	8	5.20 (0.35, 0.64, 5.15)	H= -3.60 L= -2.32 Δ_{H-L}= 1.28	H= -3.64 L= -2.75 Δ_{H-L} = 0.89	H= -3.60 L= -2.75 Δ_{H-L}= 0.85	4.97	1.34
$(PMe_3)_5(Fe_6S_8)_2(CO)_5$	14	21.56 (-3.29, -5.27, -20.64)	H= -4.26 L= -3.52 Δ_{H-L}= 0.74	H= -4.33 L= -3.96 Δ_{H-L}= 0.37	H= -4.26 L= -3.96 Δ_{H-L}= 0.30	5.33	2.75

*H and L are the energies (eV) of HOMO and LUMO states, respectively. Δ_{H-L} is the HOMO-LUMO gap in eV.

4b.3. Conclusions

In this work, we have shown that the electronic and redox properties of Fe_6S_8 clusters can be predictably altered by using suitable donor/acceptor ligands. Successive attachment of donor ligands (e.g., PMe_3) to the cluster induces an upward shift to the electronic levels, reducing the AIP significantly. However, the cluster's magnetic moment remains the same except for the fully ligated cluster, i.e., $Fe_6S_8(PMe_3)_6$. On the other hand, when CO ligands sequentially replace PMe_3 ligands in $Fe_6S_8(PMe_3)_6$ such that the cluster always remains fully ligated, lowering the energy levels is observed. The CO ligand's π-acceptor characteristics are responsible for the substantial increase in AIP and AEA without perturbation in the net magnetic moment. The increase in the AIP and AEA suggests that a donor cluster, $Fe_6S_8(PMe_3)_6$, has transformed into an acceptor cluster, $Fe_6S_8(CO)_6$, through a simple ligand substitution. Finally, the combination of two stable cluster motifs: $Fe_6S_8(PMe_3)_5$ and $Fe_6S_8(CO)_5$, consisting of ligands with two different natures, leads to a superatomic dimer, $(PMe_3)_5(Fe_6S_8)_2(CO)_5$ marked by massive internal electric dipole moment and a large magnetic moment. Such dimers with rare properties might offer tremendous potentials in various applications such as spin-polarized transport and could act as building blocks for ferroelectric materials consisting of weakly coupled magnetic units.

Chapter 4c

Interfacial Magnetism in a Fused Superatomic Cluster $[Co_6Se_8(PEt_3)_5]_2$

The study of superatomic dimer $[Co_6Se_8(PEt_3)_5]_2$ studied shadowing an experiment where a cluster assembly used the dimer as a building block. We successfully explained the formation of the cluster assembled materials consisting of $[Co_6Se_8(PEt_3)_5]_2$ dimer and fullerenes. Furthermore, an intriguing magnetic character is also detected. There exists an interfacial magnetism at the junction of $[Co_6Se_8(PEt_3)_5]_2$, where two $[Co_6Se_8(PEt_3)_5$ clusters fuse to form a dimer.

4c.1. Introduction

An isolated $Co_6Se_8(PEt_3)_6$ cluster is non-magnetic; however, we find that a magnetic unit can be formed by fusing two $Co_6Se_8(PEt_3)_5$ superatoms into a $[Co_6Se_8(PEt_3)_5]_2$ dimer. Theoretical studies indicate that the dumbbell-shaped $[Co_6Se_8(PEt_3)_5]_2$ dimer has a spin moment of 2 μ_B, and the spin density is primarily localized at the interfacial Co-sites of the fused dimer. The dimer has a low ionization energy of 4.17 eV, allowing donation of charge to C_{70} while forming a cluster assembled material, as seen in recent experiments by Nuckolls and co-workers. The donation of charge causes the dimer's magnetic moment to drop to 1 μ_B. We hypothesize that adding electrons to the dimer, such as doping impurities to the crystal lattice, may enhance the magnetic moment by neutralizing the charged cluster, revealing a strategy for stabilizing magnetic moments in ligated cluster assemblies.

Ligated metal chalcogenide clusters have emerged as a new class of superatoms that have attracted considerable interest.[46–51,84] The most common central core of metal-chalcogenide clusters has a composition of $TM_6X_8(L)_6$ (TM: transition metal, X: Chalcogen, L: Ligand). These building blocks are highly stable, can be prepared in solution, and are redox-active, allowing the formation of ionic cluster assembled solids with various complementary units.[49–53,84,85] These interesting classes of solids were initially reported by Roy et al.,[49–53,84,85] who synthesized three such solids, including $[Co_6Se_8(PEt_3)_6][C_{60}]_2$, $[Cr_6Te_8(PEt_3)_6][C_{60}]_2$, and $[Ni_9Te_6(PEt_3)_8][C_{60}]$. In each case, the core consists of chalcogenide-based clusters decorated with 6 or 8 triethylphosphine (PEt_3) ligands connected to the metal atoms, thus protecting the sensitive metallic core. In the solid phase, the ligated clusters donate charge to C_{60} (charge acceptor) to form an ionic assembly analogous to CdI_2 or NaCl class of ionic salts.[51] Recent theoretical investigations have revealed that the ligands protect the metallic cores and control the electronic and magnetic properties. Furthermore, donation of charge to counterions promotes the formation of stable crystalline solids through ionic cluster assemblies.[86–89]

The attached ligands generally protect the clusters and promote the formation of the ionic solids; however, the ligands may quench the magnetic moment of the transition metal atoms in the cluster.[90] Thus, we seek a way to protect the metal-chalcogenide cluster with ligands while also stabilizing the respective magnetic state. In this work, we show that by fusing two ligated superatomic clusters, one can form a dimer with a magnetic moment localized at the interface between the fused clusters.[11,91–93] We demonstrate this by considering the metal-chalcogenide cluster-core of Co_6Se_8 with PEt_3 ligands. The addition of six PEt_3 ligands to the Co-sites quenches the spin magnetic moment of the cluster.

In contrast, removing the PEt$_3$ ligands can restore the spin moment. However, the unligated cluster becomes unstable. One way to overcome this problem is to join two Co$_6$Se$_8$(PEt$_3$)$_5$ clusters into a composite [Co$_6$Se$_8$(PEt$_3$)$_5$]$_2$ unit through covalent bonding between Co and Se sites on different clusters. Here we show that such a composite cluster has a finite spin moment localized at the interfacial sites, thus offering a unique opportunity for a tunable spin magnetic moment in a ligand protected cluster. Additionally, these magnetic units can also be arranged into a magnetic cluster assembly.

Our investigations are inspired by the recent experimental work by Nuckolls et al.,[94], who have stabilized metal-chalcogenide dimers, [Co$_6$Se$_8$(PEt$_3$)$_5$]$_2$ with C$_{70}^-$ dimers forming a cluster assembled solid using toluene solvent. As pointed out by Nuckolls et al.[94], the dimers' elongated shapes allow the facile synthesis of novel solids that pack these dumbbell-shaped composite metal-chalcogenide clusters with other dumbbell-shaped C$_{140}$ counterions to form stable anisotropic solids. Furthermore, the shape allows the generation of multiple assemblies with differing atomic arrangements of these ionic cluster solids formed from [Co$_6$Se$_8$(PEt$_3$)$_5$]$_2^+$ cations and C$_{140}^{2-}$ anions. We find the large cohesive energy of the cluster assembled material demonstrating a significant stabilization during the formation of the material by charge transfer from the metal-chalcogenide dimers to the fullerenes. Hence, the material is stabilized via ionic bonding.

4c.2. Results

Effect of Ligands on the magnetic properties of a Co$_6$Se$_8$(PEt$_3$)$_n$ (n=0-6) cluster and dimer formation

We present a brief review of the ligand effects on a Co$_6$Se$_8$ cluster's spin-magnetic moment. The ground-state structure of Co$_6$Se$_8$ cluster has a net spin magnetic moment of 10 μ_B. The average Co−Se bond is around 2.39 Å, and each Co-site carries a local spin magnetic moment of approximately 1.5 μ_B. The successive additions of PEt$_3$ ligands decrease the total magnetic moment monotonically until the magnetic moment is wholly quenched for the fully ligated cluster. The local

spin-moments reduce drastically after the ligation on the Co-sites, also seen in Figure 4.15. A detailed electronic structure investigation reveals that the ligand states bind with the d-states of the Co-sites that lead to a filling of minority states resulting in a decrease in the local moment, as shown in our previous work.[90] These results suggest that one way to create a magnetic cluster is to remove one or more ligands; however, such unligated species are likely to be transient. One strategy for stabilizing such magnetic clusters is to fuse two ligated metal-chalcogenide clusters. When two $Co_6Se_8(PEt_3)_5$ clusters combine through the unligated Co-sites with the Se-sites of another cluster, they form a composite superatomic dimer $[Co_6Se_8(PEt_3)_5]_2$, as shown in Figure 4.16. This dimer could result in a magnetic species with no exposed metal sites and enhanced stability. The ligated dimer is protected from exposure; however, the lack of a closed electronic shell and numerous phosphine ligands means that such dimers will likely be excellent charge donors and become cations when forming the cluster assembled solids. Figure 4.16 shows the dumbbell-shaped ground state structure of $[Co_6Se_8(PEt_3)_5]_2$ with a net spin moment of 2 μ_B. The dimer's Adiabatic Ionization Potential (AIP) is only 4.17 eV, slightly less than that of a K atom[95], showing its aptness as a donor. Since the cluster is expected to donate charge while forming an ionic solid, we also calculated the spin magnetic moment of the cationic species and found it to be 1 μ_B. The spin densities for both neutral and cationic dimers are localized at the interfacial Co-atoms of the fused clusters, as seen in the isosurfaces in Figure 4.16(b). Thus, we have a magnetic moment on the unligated Co-sites at the interface while still protecting the interfacial Co-atoms from the reactivity. To gain more insight into the nature of states contributing to the moment, we show in Figure 4.17 the one-electron levels in the neutral and cationic dimers. The ground state of the neutral cluster is marked by a pair of d-states a_1 and a_2 (D_{yz}/D_{xz} and D_z^2) in the majority spin states that are unoccupied in the minority spin states, as shown in Figure 4.17(a).
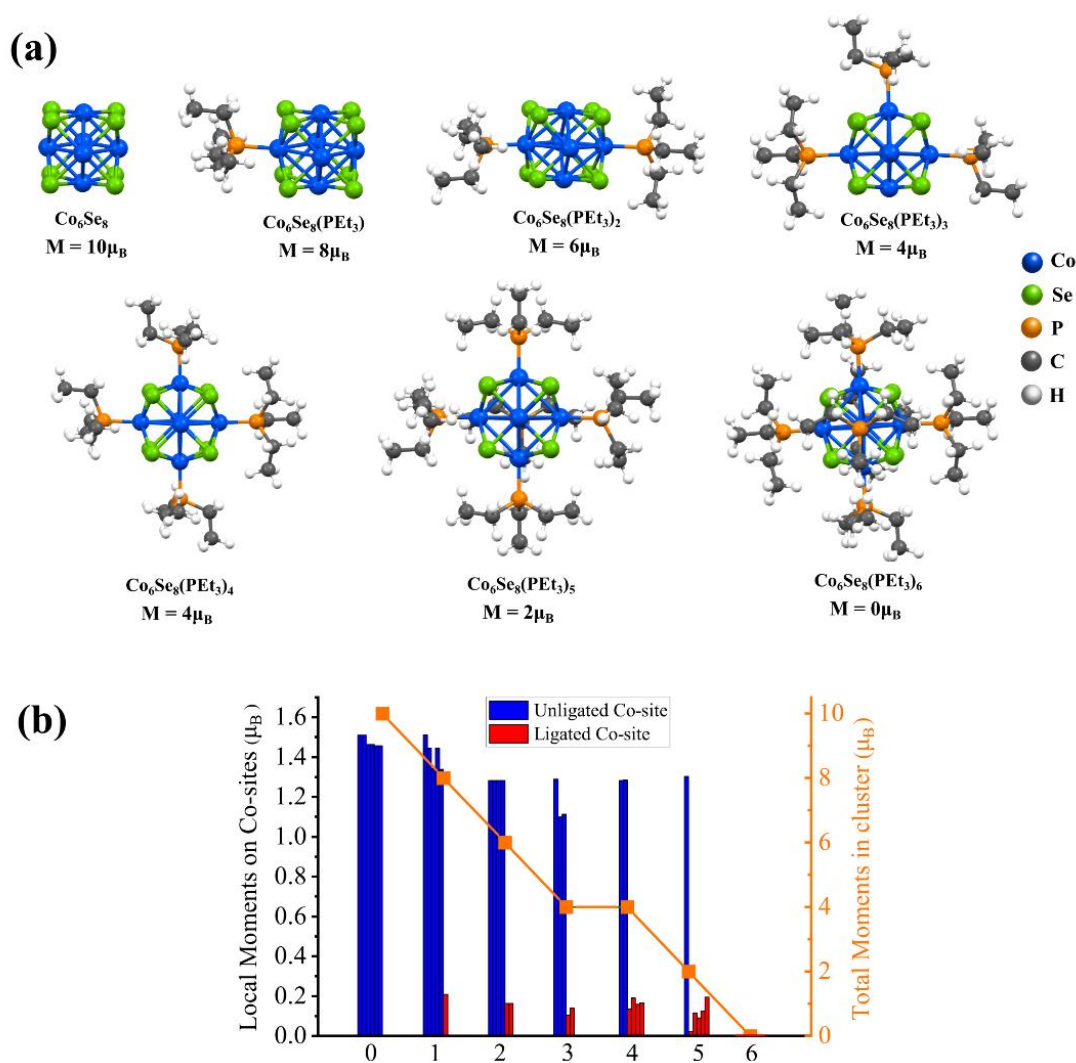
Figure 4.15 (a) Ground state structures of $Co_6Se_8(PEt_3)_n$ (n = 0-6). The net magnetic moments (μ_B) for each system are also provided. (b) A representative plot of the local magnetic moments of the unligated and ligated Co sites for $Co_6Se_8(PEt_3)_n$ (n = 0-6). The total magnetic moments of each clusters are also plotted in orange.

These states correspond to the d-states of the interfacial Co-atoms and are responsible for the spin magnetic moment of 2 μ_B. The HOMO level is in the majority spin, while the LUMO level is in the minority manifold. However, when the dimer becomes cationic, the HOMO level shifts to the minority spin channel, and the LUMO level shifts to the majority spin states, as shown in Figure 4.17(b).
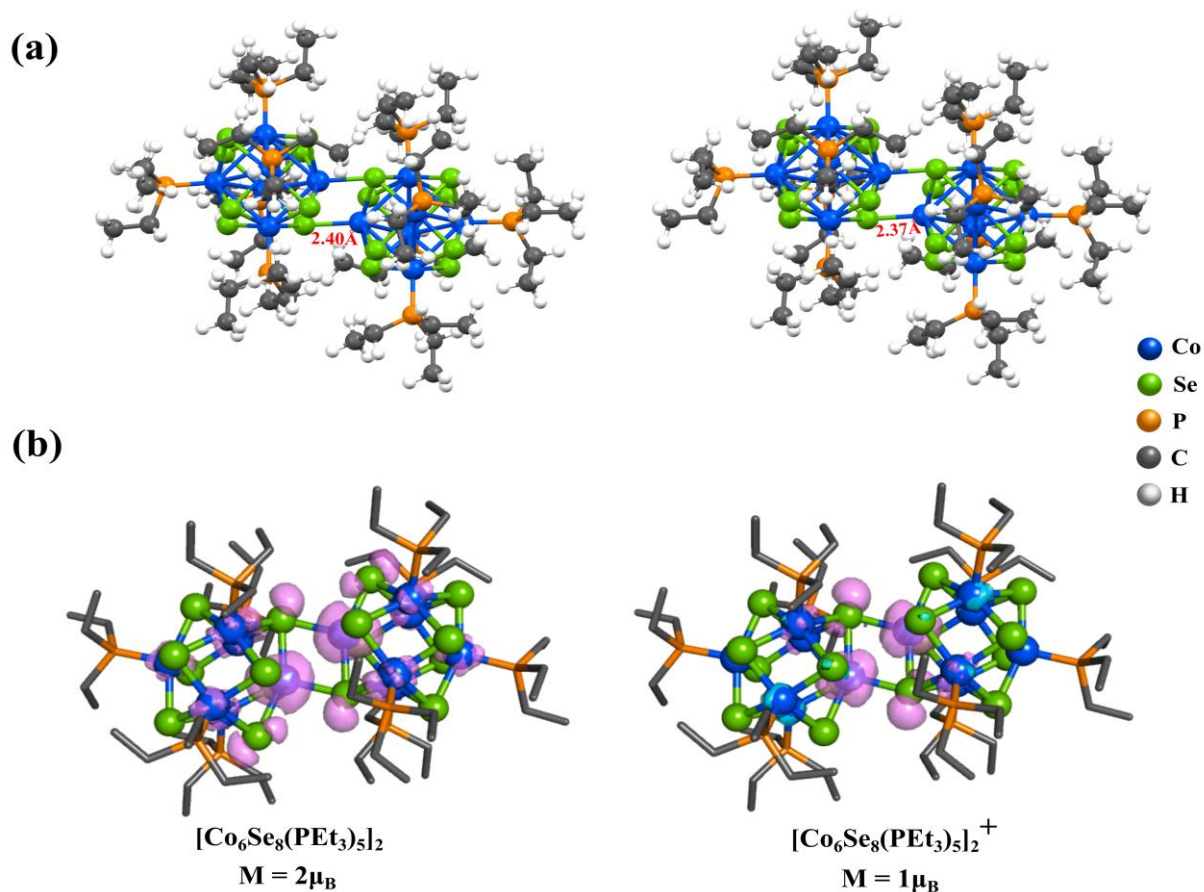
Figure 4.16 (a) Optimized ground state structure and (b) Spin density isosurface plot of the neutral and cationic $[Co_6Se_8(PEt_3)_5]_2$ dimer.

We also analyzed the electronic states to examine the stability of clusters. The neutral and cationic species are marked by HOMO-LUMO gaps of 0.35 and 0.30 eV, respectively. Additionally, we found that the magnetic moment of the dimer with +2 oxidation state is also 2 μ_B. It is interesting to note that both neutral and +2 state has a magnetic moment of 2 μ_B, while the cationic dimer has the spin magnetic moment of 1 μ_B.
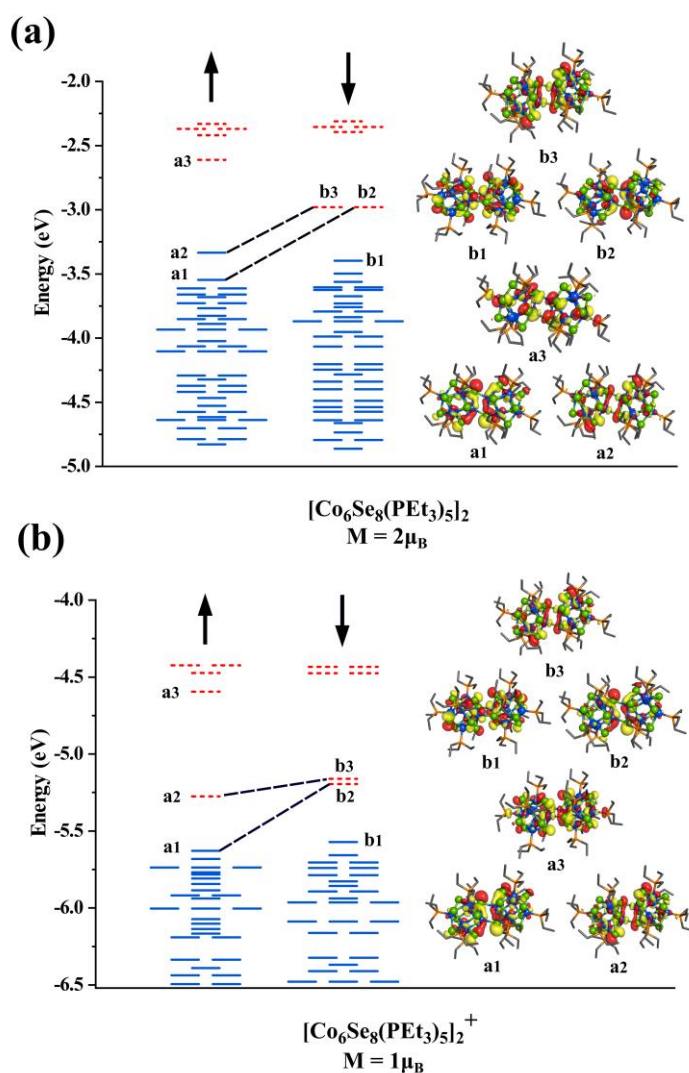
Figure 4.17 The one-electronic energy levels of (a) neutral and (b)cationic $[Co_6Se_8(PEt_3)_5]_2$ dimer. The isosurfaces of a few selected orbitals are also shown.

Since a pair of unfilled minority states characterize the neutral species, one may ask if filling those states would complete the electronic shell and lead to an electronically stable cluster. To explore this possibility, we investigated the electronic structure of a $[Co_6Se_8(PEt_3)_5]_2^{2-}$ cluster, which is

found to be non-magnetic with a larger HOMO-LUMO gap of 0.53 eV, indicative of an electronically stable species.

Cluster assembled solid

As mentioned earlier, Nuckolls et al.[94] have recently synthesized a cluster assembled solid by combining $[Co_6Se_8(PEt_3)_5]_2$ dimers with C_{140} motifs composed of two-linked C_{70} clusters with toluene solvent molecules.[94] Both $[Co_6Se_8(PEt_3)_5]_2$ and C_{140} are observed to have dumbbell-shaped structures. They have synthesized three different cluster-assembled solids made from $[Co_6Se_8(PEt_3)_5]_2$ and the C_{70} dimers(C_{140}), using different stoichiometry of toluene molecules. Initially, we start with investigating the redox properties of the cluster building blocks to understand the formation of this cluster assembled solid.
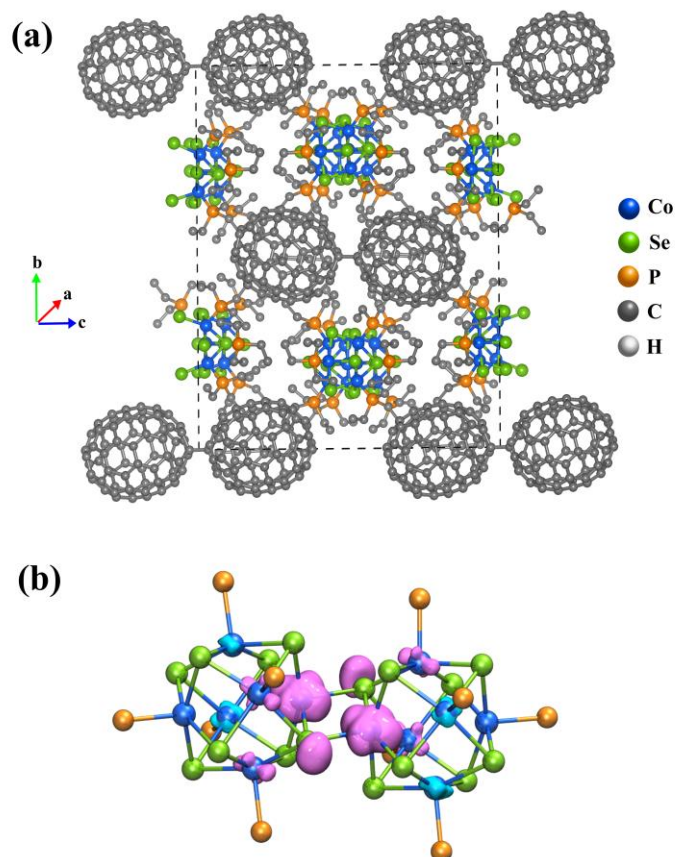
Figure 4.18 a) The optimized unit cell structure of $\{[Co_6Se_8(PEt_3)_5]_2(Toluene)_2C_{140}\}_2$ crystal.

b) The spin density isosurface of the dimer unit.

As the HOMO of the $[Co_6Se_8(PEt_3)_5]_2$ dimer is higher than the LUMO of the C_{70}, the electron transfer from the dimer to the C_{70} is energetically favorable. The radical C_{70}^- anions formed have HOMO-LUMO gaps of only 0.12 eV and are highly reactive. Hence, the C_{70}^- anions combine to form the dimer C_{140}^{2-}, that has a closed electronic shell and a large HOMO-LUMO gap of 0.73 eV. We next examined one of the crystal structures from experiment[94] to understand how the electronic structure of the metal chalcogenide-dimers evolves as they form the observed cluster-assembled solid. We studied the crystal structure of the solid with the stoichiometry of $\{[Co_6Se_8(PEt_3)_5]_2(Toluene)_2C_{140}\}_2$ in the unit cell, and the details of the calculations are noted in the Methods Section in Chapter 2. Figure 4.18 shows the unit cell and an isosurface of the electron spin density, which exhibits that spin density is localized on the interface between the fused clusters, as seen in Figure 4.18(b). The magnetic moment on each dimer is found to be 1 μ_B; however, the coupling between the four dimers in the unit cell is antiferromagnetic. This antiferromagnetic arrangement is only 0.03 eV lower than the ferromagnetic state, displaying the magnetic moment of 1 μ_B per dimer or 4 μ_B per unit cell. The schematic of the antiferromagnetic and ferromagnetic couplings between the dimers in the solid is given in Appendix Figure A1. Besides the energies being very close for the antiferromagnetic and ferromagnetic couplings, the bandgap energies are also almost equal with the values of 0.24 eV for each. We know that the spin magnetic moments of the neutral and cationic dimers are 2 μ_B and 1 μ_B, respectively, from our free cluster calculations. Hence, the dimers in the solid with 1 μ_B can be best described as cations $[Co_6Se_8(PEt_3)_5]_2^+$. To confirm this, we did a Bader analysis of the charge density and found a charge transfer of 0.81 e$^-$ from each $[Co_6Se_8(PEt_3)_5]_2$-dimer units to the C_{140} units as seen in Table 4.2. It confirms that the dimers are in the cationic state, and the C_{140} are also best described as C_{140}^{2-}. These theoretical calculations verify the experimental inference of charge transfer between the dimers and the fullerene units.[94] The stabilization of the cluster assembly due to charge transfer is confirmed by an

energy analysis that gives the cohesive energy of the unit cell to be 26.68 eV. The cohesive energy is calculated by equation 1,

$$E_{cohesive} = E_{Solid} - 4\, E_{[Co_6Se_8(PEt_3)_5]_2} - 4\, E_{C_{70}} - 4\, E_{Tol} \hspace{2cm} (4.2)$$

E_{Solid}, $E_{[Co_6Se_8(PEt_3)_5]_2}$, $E_{C_{70}}$, and E_{Tol} represent the energies of solid, $[Co_6Se_8(PEt_3)_5]_2$, C_{70}, and toluene molecules, respectively in equation 4.2. To investigate further, we have calculated the removal energy of individual components in the solid. The removal energy is computed as the energy difference between the optimized $\{[Co_6Se_8(PEt_3)_5]_2(Toluene)_2C_{140}\}_2$ crystal and the optimized solid without the respective component. We found that the toluene's removal energy is 0.97 eV per molecule, and this comes to 3.88 eV for the four molecules in the unit cell. For comparison, the removal energies of the $(C_{70})_2$ and $[Co_6Se_8(PEt_3)_5]_2$ are found to be 9.66 and 7.72 eV, respectively. These large removal energies confirm that there is ionic interaction holding the material together. An alternative way of looking at this is that the cohesive energy of the cluster assembled material per electron transfer from the dimer to the C_{70} is 6.67 eV, as there are 4 electron transfers per unit cell. For comparison, the cohesive energy for NaCl is ~8.19 eV per electron transfer[96,97], so the value is in the range expected for an ionic solid. The 6.67 eV cohesive energy combines several factors; in addition to the electron transfer, the bonding that forms the $(C_{70})_2$ by combining two C_{70} is also included, as our reference energy is isolated C_{70}. For free clusters, this bond energy is approximately 1.11 eV for combining two C_{70}^- into $(C_{70})_2^{2-}$. The result of this dimer formation is a rough estimate since the stability of double anions in free space is much lower than in a solution or in a solid. The cohesive energy of 6.67 eV per electron transfer demonstrates that the present cluster assembled material is not a molecular solid but rather a material held together via ionic bonding. The projected density of states (PDOS) of metal chalcogenide dimer, fullerene, and toluene within the solid is shown in Figure 4.19. The material's bandgap energy is calculated to be 0.24 eV, with the valence band edge composed of the states on the metal-chalcogenide dimer. In contrast, the conduction band edge is mostly localized on the fullerenes (C_{140}). The gap on the

metal-chalcogenide dimers is found to be 0.32 eV. The optical bandgap from the experiment is

reported to be 0.55 eV, which is higher than the calculated value. Our calculated value is expected

Table 4.2 The charge transfer between fused clusters, C_{140} units, and toluene molecules.

Units	Charges	Total number of units	Total-Charge
Cluster	0.8056	4	3.2224
C_{140}	-1.6174	2	-3.2348
Toluene	0.00297	4	0.0119

to be lower than the experimentally observed value since the valence band edge is found on the

metal-chalcogenide while the edge of the conduction band is on the fullerenes so that the band edge

excitations may be relatively weak.
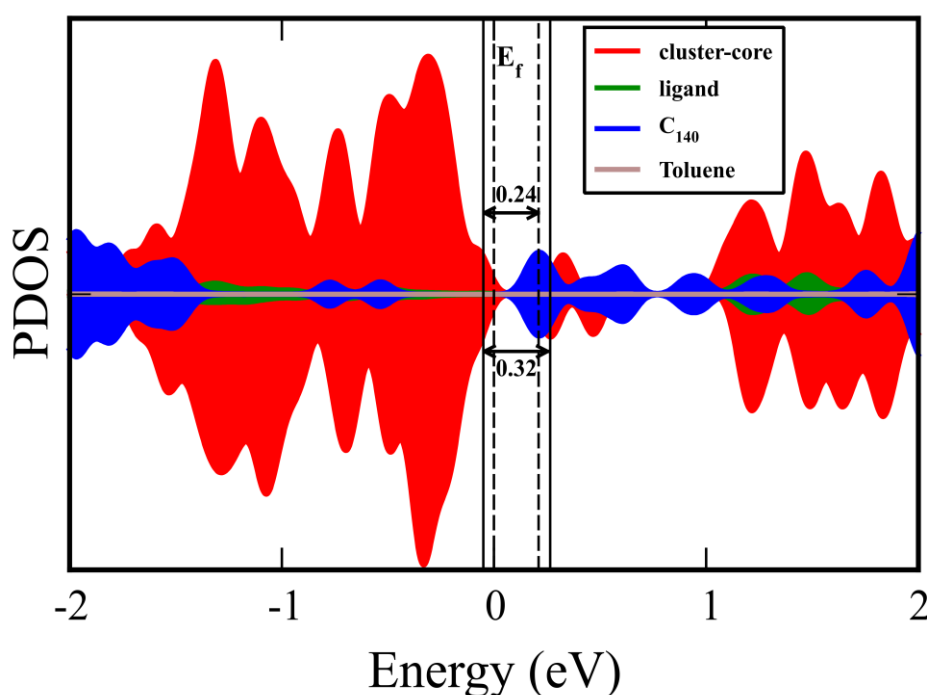
Figure 4.19 The projected density of state (PDOS) plot including the various components

of $\{[Co_{12}Se_{16}(PEt_3)_{10}]_2(Toluene)_2C_{140}\}_2$ solid.

Furthermore, the density functional theory also tends to underestimate the bandgap energy.[98–101]

We next want to understand how the electronic structure changes as we move through the fused

cluster dimer and are especially interested in the interfacial region where the two clusters are joined.

We plotted the local density of states of different regions of the dimer in Figure 4.20. The regions

correspond to different cross-sections of the fused clusters as we move from one terminal end, the 1st and 2nd regions, through the interface, the 3rd region, and on to the other terminal end of the cluster
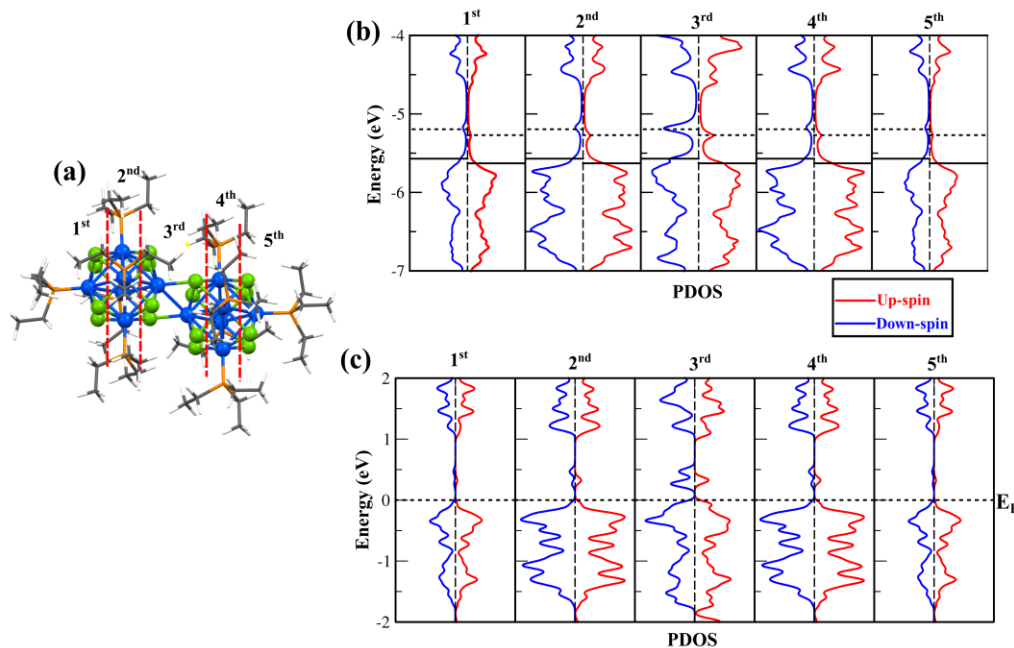
Figure 4.20 a) The splitting of dimer into different regions, b) local density of states of different sections of the cationic metal-chalcogenide dimer in isolated system and c) within the solid

The 1st ${[Co_6Se_8(PEt_3)_5]_2(Toluene)_2C_{140}}_2$.   in Figure 4.20(a). Figure 4.20(b) provides the local density of states of free cationic dimer $[Co_6Se_8(PEt_3)_5]_2^+$, and Figure 4.20(c) presents the local density of states of the metal-chalcogenide dimer in the cluster assembled solid. In both the free cluster and the solid, we see that the spin is quenched in every region except in the 3rd region that lies at the junction between the fused clusters. In the 3rd region, two unfilled minority states and one unfilled majority impurity state are found, consistent with a spin of 1 μ_B per cluster, offering additional proof that the spin is localized only at the interfacial Co-atoms. Hence, we have stabilized a ligand-protected cluster with a finite magnetic moment at the junction by fusing two clusters. Besides, we have reconfirmed that the interfacial magnetic moments of the metal-chalcogenide dimers are preserved even after the solid assembly. Next, we consider the effect of adding or removing electrons on the magnetic state of such metal-chalcogenide dimers. The metal-chalcogenide dimers in the solid have +1 charge states with a

magnetic moment of 1 μ_B. However, the neutral and +2 states of metal-chalcogenide dimers have a magnetic moment of 2 μ_B. Hence, if an electron can be added to or taken out from the dimers in the solid, then the magnetic moment of the solid can be increased. Fortunately, the controlled doping of impurities in the crystal lattice is possible through chemical synthesis.[30] Thus, the addition of electron-donating or electron-withdrawing species to the material might enhance the magnetic moment, offering a cluster assembled material with tunable magnetic properties.[18,102] It can be used as a method to enhance the magnetic moment in the ligated cluster assembled materials. We would like to add that in recent experiments, the significant electron transport was observed for only one of the three synthesized cluster assembled materials- $\{[Co_6Se_8(PEt_3)_5]_{1.44}(Toluene)_2C_{140}\}_2$, where the distance between the C_{140} chains was only 3.8 Å (the shortest distance between three cluster assembled materials). It was proposed that the conduction in that assembly was through fullerenes. However, it should be possible to induce conduction pathways through chalcogenide clusters by appropriate doping. One strategy to induce conductivity through the metal-chalcogen clusters would be to use bidentate aromatic ligands that could connect different clusters or use smaller ligands such as PMe_3 to decrease the distance between the clusters. The second strategy could be to use 4d or 5d transition metals as these clusters may be more delocalized than the 3d clusters, resulting in better conduction. However, this may also lead to a change in the spin on the cluster interface. Hence, under circumstances where the conduction is through the metal-chalcogen clusters, the currents will be spin-polarized.

4c.3. Conclusions

To summarize, we have shown that by linking two $Co_6Se_8(PEt_3)_5$ clusters, it is possible to form a composite dimer $[Co_6Se_8(PEt_3)_5]_2$ that is magnetic. The spin magnetic moment is primarily localized at the interfacial Co-sites of the fused into a dimer. Furthermore, the dumb-bell-shaped dimer is marked by low ionization energy of 4.17 eV, which can interact with the similar shaped C_{140} composed of two C_{70} units, characterized

by a high electron affinity to form a stable ionic solid. Additionally, the theoretical calculations confirm that the $[Co_6Se_8(PEt_3)_5]_2$ dimer loses electrons to C_{140} in the solid, leaving each metal-chalcogenide dimer as cations supporting the experimental work done by Nuckolls and co-workers.[94] The neutral dimers have a spin moment of 2 μ_B per cluster, while the cationic dimers have spin moments of 1 μ_B. When an electron passes through the metal-chalcogenide dimer, the transient neutrality of the cationic species will favor the higher magnetic state of the neutral dimer. Thus, the cluster-dimer is expected to show an intriguing magnetic characteristic when an electron is added to the system. Suppose the electron is induced through the impurities to the cluster assembled materials. In that case, it can be used as a strategy to enhance the magnetic moment. It might also lead to the spin-polarized current, a helpful situation for spintronic-related applications.

References

1 E. A. Doud, A. Voevodin, T. J. Hochuli, A. M. Champsaur, C. Nuckolls and X. Roy, *Nat Rev Mater*, 2020, **5**, 371–387.

2 W. Shockley and H. J. Queisser, *Journal of Applied Physics*, 1961, **32**, 510–519.

3 L. M. Terman, *Solid-State Electronics*, 1962, **5**, 285–299.

4 S. J. Jiao, Z. Z. Zhang, Y. M. Lu, D. Z. Shen, B. Yao, J. Y. Zhang, B. H. Li, D. X. Zhao, X. W. Fan and Z. K. Tang, *Appl. Phys. Lett.*, 2006, **88**, 031911.

5 M.-Y. Li, Y. Shi, C.-C. Cheng, L.-S. Lu, Y.-C. Lin, H.-L. Tang, M.-L. Tsai, C.-W. Chu, K.-H. Wei, J.-H. He, W.-H. Chang, K. Suenaga and L.-J. Li, *Science*, 2015, **349**, 524–528.

6 Q. Kong, W. Lee, M. Lai, C. G. Bischak, G. Gao, A. B. Wong, T. Lei, Y. Yu, L.-W. Wang, N. S. Ginsberg and P. Yang, *PNAS*, 2018, **115**, 8889–8894.

7 N. Yaacobi-Gross, M. Soreni-Harari, M. Zimin, S. Kababya, A. Schmidt and N. Tessler, *Nature Materials*, 2011, **10**, 974–979.

8 W. W. Gärtner, *Phys. Rev.*, 1959, **116**, 84–87.

9   A. S. Grove and D. J. Fitzgerald, *Solid-State Electronics*, 1966, **9**, 783–806.

10 S. Mandal, A. C. Reber, M. Qian, R. Liu, H. M. Saavedra, S. Sen, P. S. Weiss, S. N. Khanna and A. Sen, *Dalton Trans.*, 2012, **41**, 12365–12377.

11 A. M. Champsaur, T. J. Hochuli, D. W. Paley, C. Nuckolls and M. L. Steigerwald, *Nano Lett.*, 2018, **18**, 4564–4569.

12 S. A. Claridge, A. W. Castleman, S. N. Khanna, C. B. Murray, A. Sen and P. S. Weiss, *ACS Nano*, 2009, **3**, 244–255.

13 S. Mandal, A. C. Reber, M. Qian, P. S. Weiss, S. N. Khanna and A. Sen, *Acc. Chem. Res.*, 2013, **46**, 2385–2395.

14 Y. Shichibu, Y. Negishi, T. Watanabe, N. K. Chaki, H. Kawaguchi and T. Tsukuda, *J. Phys. Chem. C*, 2007, **111**, 7845–7847.

15 X. Roy, C.-H. Lee, A. C. Crowther, C. L. Schenck, T. Besara, R. A. Lalancette, T. Siegrist, P. W. Stephens, L. E. Brus, P. Kim, M. L. Steigerwald and C. Nuckolls, *Science*, 2013, **341**, 157–160.

16 B. Choi, J. Yu, D. W. Paley, M. T. Trinh, M. V. Paley, J. M. Karch, A. C. Crowther, C.-H. Lee, R. A. Lalancette, X. Zhu, P. Kim, M. L. Steigerwald, C. Nuckolls and X. Roy, *Nano Lett.*, 2016, **16**, 1445–1449.

17 B. Choi, K. Lee, A. Voevodin, J. Wang, M. L. Steigerwald, P. Batail, X. Zhu and X. Roy, *J. Am. Chem. Soc.*, 2018, **140**, 9369–9373.

18 E. S. O'Brien, M. T. Trinh, R. L. Kann, J. Chen, G. A. Elbaz, A. Masurkar, T. L. Atallah, M. V. Paley, N. Patel, D. W. Paley, I. Kymissis, A. C. Crowther, A. J. Millis, D. R. Reichman, X.-Y. Zhu and X. Roy, *Nature Chemistry*, 2017, **9**, 1170.

19 W.-L. Ong, E. S. O'Brien, P. S. M. Dougherty, D. W. Paley, C. F. H. Iii, A. J. H. McGaughey, J. A. Malen and X. Roy, *Nature Materials*, 2017, **16**, 83.

20 A. Pinkard, A. M. Champsaur and X. Roy, *Acc. Chem. Res.*, 2018, **51**, 919–929.

21 V. Chauhan, A. C. Reber and S. N. Khanna, *J. Phys. Chem. A*, 2016, **120**, 6644–6649.

22 V. Chauhan, A. C. Reber and S. N. Khanna, *J. Am. Chem. Soc.*, 2017, **139**, 1871–1877.

23 A. C. Reber and S. N. Khanna, *npj Computational Materials*, 2018, **4**, 33.

24 V. Chauhan and S. N. Khanna, *J. Phys. Chem. A*, 2018, **122**, 6014–6020.

25 A. C. Reber, D. Bista, V. Chauhan and S. N. Khanna, *J. Phys. Chem. C*, 2019, **123**, 8983–8989.

26 G. Liu, A. Pinkard, S. M. Ciborowski, V. Chauhan, Z. Zhu, A. P. Aydt, S. N. Khanna, X. Roy and K. H. Bowen, *Chem. Sci.*, 2019, **10**, 1760–1766.

27 A. C. Reber and S. N. Khanna, *Eur. Phys. J. D*, 2018, **72**, 199.

28 T. G. Gray, C. M. Rudzinski, D. G. Nocera and R. H. Holm, *Inorg. Chem.*, 1999, **38**, 5932–5933.

29 M. P. Shores, L. G. Beauvais and J. R. Long, *Inorg. Chem.*, 1999, **38**, 1648–1649.

30 L. F. Szczepura, D. L. Cedeño, D. B. Johnson, R. McDonald, S. A. Knott, K. M. Jeans and J. L. Durham, *Inorg. Chem.*, 2010, **49**, 11386–11394.

31 X. Zhong, K. Lee, B. Choi, D. Meggiolaro, F. Liu, C. Nuckolls, A. Pasupathy, F. De Angelis, P. Batail, X. Roy and X. Zhu, *Nano Lett.*, 2018, **18**, 1483–1488.

32 S. N. Khanna and P. Jena, *Phys. Rev. B*, 1995, **51**, 13705–13716.

33 A. C. Reber and S. N. Khanna, *Acc. Chem. Res.*, 2017, **50**, 255–263.

34 J. L. Shott, M. B. Freeman, N.-A. Saleh, D. S. Jones, D. W. Paley and C. Bejger, *Inorg. Chem.*, 2017, **56**, 10984–10990.

35 B. M. Boardman, J. R. Widawsky, Y. S. Park, C. L. Schenck, L. Venkataraman, M. L. Steigerwald and C. Nuckolls, *J. Am. Chem. Soc.*, 2011, **133**, 8455–8457.

36 B. J. Reeves, D. M. Shircliff, J. L. Shott and B. M. Boardman, *Dalton Trans.*, 2015, **44**, 718–724.

37 C. A. Tolman, *J. Am. Chem. Soc.*, 1970, **92**, 2953–2956.

38 H. Metiu, S. Chrétien, Z. Hu, B. Li and X. Sun, *J. Phys. Chem. C*, 2012, **116**, 10439–10450.

39 A. C. Reber and S. N. Khanna, *J. Phys. Chem. C*, 2014, **118**, 20306–20313.

40 Y. Yang, C. E Castano, B. Frank Gupton, A. C. Reber and S. N. Khanna, *Nanoscale*, 2016, **8**, 19564–19572.

41 Y. Yang, A. C. Reber, S. E. Gilliland, C. E. Castano, B. F. Gupton and S. N. Khanna, *Journal of Catalysis*, 2018, **360**, 20–26.

42 F. Wang and T. Ziegler, *J. Chem. Phys.*, 2005, **123**, 154102.

43 M. O'Neil, J. Marohn and G. McLendon, *J. Phys. Chem.*, 1990, **94**, 4356–4363.

44 Z. Zhang and J. T. Yates, *J. Phys. Chem. C*, 2010, **114**, 3098–3101.

45 C. Girard, C. Joachim, C. Chavy and P. Sautet, *Surface Science*, 1993, **282**, 400–410.

46 J. F. Corrigan, O. Fuhr and D. Fenske, *Advanced Materials*, 2009, **21**, 1867–1871.

47 C. E. Anson, A. Eichhöfer, I. Issac, D. Fenske, O. Fuhr, P. Sevillano, C. Persau, D. Stalke and J. Zhang, *Angewandte chemie international edition*, 2008, **47**, 1326–1331.

48 C. A. Goddard, J. R. Long and R. H. Holm, *Inorganic chemistry*, 1996, **35**, 4347–4354.

49 A. M. Champsaur, J. Yu, X. Roy, D. W. Paley, M. L. Steigerwald, C. Nuckolls and C. M. Bejger, *ACS Cent. Sci.*, 2017, **3**, 1050–1055.

50 A. Pinkard, A. M. Champsaur and X. Roy, *Accounts of chemical research*, 2018, **51**, 919–929.

51 X. Roy, C.-H. Lee, A. C. Crowther, C. L. Schenck, T. Besara, R. A. Lalancette, T. Siegrist, P. W. Stephens, L. E. Brus and P. Kim, *Science*, 2013, **341**, 157–160.

52 N. A. Gadjieva, A. M. Champsaur, M. L. Steigerwald, X. Roy and C. Nuckolls, *European Journal of Inorganic Chemistry*.

53 C.-H. Lee, L. Liu, C. Bejger, A. Turkiewicz, T. Goko, C. J. Arguello, B. A. Frandsen, S. C. Cheung, T. Medina, T. J. S. Munsie, R. D'Ortenzio, G. M. Luke, T. Besara, R. A. Lalancette, T. Siegrist, P. W. Stephens, A. C. Crowther, L. E. Brus, Y. Matsuo, E. Nakamura, Y. J. Uemura, P. Kim, C. Nuckolls, M. L. Steigerwald and X. Roy, *J. Am. Chem. Soc.*, 2014, **136**, 16926–16931.

54 C. H. Lee, L. Liu, C. Bejger, A. Turkiewicz, T. Goko, C. J. Arguello, B. A. Frandsen, S. C. Cheung, T. Medina and T. J. Munsie, *Journal of the American Chemical Society*, 2014, **136**, 16926–16931.

55 J. Yang, F. Wang, J. C. Russell, T. J. Hochuli, X. Roy, M. L. Steigerwald, X. Zhu, D. W. Paley and C. Nuckolls, *J. Am. Chem. Soc.*, 2020, **142**, 11993–11998.

56 Q. Li, F. Liu, J. C. Russell, X. Roy and X. Zhu, *J. Chem. Phys.*, 2020, **152**, 171101.

57 K. Lee, S. F. Maehrlein, X. Zhong, D. Meggiolaro, J. C. Russell, D. A. Reed, B. Choi, F. D. Angelis, X. Roy and X. Zhu, *Advanced Materials*, 2019, **31**, 1903209.

58 T. A. Rouault and W.-H. Tong, *Nature Reviews Molecular Cell Biology*, 2005, **6**, 345–351.

59 J.-M. Mouesca and B. Lamotte, *Coordination chemistry reviews*, 1998, **178**, 1573–1614.

60 H. Beinert, R. H. Holm and E. Münck, *Science*, 1997, **277**, 653–659.

61 C. Felser, G. H. Fecher and B. Balke, *Angewandte Chemie International Edition*, 2007, **46**, 668–699.

62 D. D. Awschalom and M. E. Flatté, *Nature physics*, 2007, **3**, 153–159.

63 H. Ohno, *Science*, 2001, **291**, 840–841.

64 A. C. Reber, D. Bista, V. Chauhan and S. N. Khanna, *The Journal of Physical Chemistry C*, 2019, **123**, 8983–8989.

65 V. Chauhan, A. C. Reber and S. N. Khanna, *J. Phys. Chem. A*, 2016, **120**, 6644–6649.

66 A. C. Reber and S. N. Khanna, *npj Computational Materials*, 2018, **4**, 33.

67 V. Chauhan, A. C. Reber and S. N. Khanna, *J. Am. Chem. Soc.*, 2017, **139**, 1871–1877.

68 G. Liu, V. Chauhan, A. P. Aydt, S. M. Ciborowski, A. Pinkard, Z. Zhu, X. Roy, S. N. Khanna and K. H. Bowen, *J. Phys. Chem. C*, 2019, **123**, 25121–25127.

69 V. Chauhan, A. C. Reber and S. N. Khanna, *Nature communications*, 2018, **9**, 1–7.

70 A. C. Reber, V. Chauhan, D. Bista and S. N. Khanna, *Nanoscale*, 2020, **12**, 4736–4742.

71 D. Bista, V. Chauhan, T. Sengupta, A. C. Reber and S. N. Khanna, *Nanoscale*.

72 H. He, R. Pandey, J. U. Reveles, S. N. Khanna and S. P. Karna, *Applied Physics Letters*, 2009, **95**, 192104.

73 D. A. van Leeuwen, J. M. van Ruitenbeek, L. J. de Jongh, A. Ceriotti, G. Pacchioni, O. D. Häberlen and N. Rösch, *Phys. Rev. Lett.*, 1994, **73**, 1432–1435.

74 S. T. Akin, V. Zamudio-Bayer, K. Duanmu, G. Leistner, K. Hirsch, C. Bülow, A. Ławicki, A. Terasaki, B. von Issendorff, D. G. Truhlar, J. T. Lau and M. A. Duncan, *J. Phys. Chem. Lett.*, 2016, **7**, 4568–4575.

75 V. Chauhan, A. C. Reber and S. N. Khanna, *Physical Chemistry Chemical Physics*, 2017, **19**, 31940.

76 A. C. Reber, V. Chauhan and S. N. Khanna, *The Journal of Chemical Physics*, 2017, **146**, 024302.

77 J. Yu, C.-H. Lee, D. Bouilly, M. Han, P. Kim, M. L. Steigerwald, X. Roy and C. Nuckolls, *Nano Lett.*, 2016, **16**, 3385–3389.

78 F. Cecconi, C. A. Ghilardi, S. Midollini, A. Orlandini and P. Zanello, *Journal of the Chemical Society, Dalton Transactions*, 1987, 831–835.

79 G. U. Gamboa, A. C. Reber and S. N. Khanna, *New J. Chem.*, 2013, **37**, 3928–3935.

80 J. D. D. Martin and J. W. Hepburn, *The Journal of chemical physics*, 1998, **109**, 8139–8142.

81 F. L. Hirshfeld, *Theoretica chimica acta*, 1977, **44**, 129–138.

82 P. Atkins and T. Overton, *Shriver and Atkins' inorganic chemistry*, Oxford University Press, USA, 2010.

83 R. H. Crabtree, *The organometallic chemistry of the transition metals*, John Wiley & Sons, 2009.

84 B. M. Boardman, J. R. Widawsky, Y. S. Park, C. L. Schenck, L. Venkataraman, M. L. Steigerwald and C. Nuckolls, *J. Am. Chem. Soc.*, 2011, **133**, 8455–8457.

85 E. J. Telford, J. C. Russell, J. R. Swann, B. Fowler, X. Wang, K. Lee, A. Zangiabadi, K. Watanabe, T. Taniguchi, C. Nuckolls, P. Batail, X. Zhu, J. A. Malen, C. R. Dean and X. Roy, *Nano Lett.*, 2020, **20**, 1718–1724.

86 S. A. Claridge, A. W. Castleman, S. N. Khanna, C. B. Murray, A. Sen and P. S. Weiss, *ACS Nano*, 2009, **3**, 244–255.

87 S. Mandal, A. C. Reber, M. Qian, P. S. Weiss, S. N. Khanna and A. Sen, *Acc. Chem. Res.*, 2013, **46**, 2385–2395.

88 S. Serrano-Guisan, G. di Domenicantonio, M. Abid, J.-P. Abid, M. Hillenkamp, L. Gravier, J.-P. Ansermet and C. Félix, *Nat Mater*, 2006, **5**, 730–734.

89 A. Turkiewicz, D. W. Paley, T. Besara, G. Elbaz, A. Pinkard, T. Siegrist and X. Roy, *J. Am. Chem. Soc.*, 2014, **136**, 15873–15876.

90 G. Liu, V. Chauhan, A. P. Aydt, S. M. Ciborowski, A. Pinkard, Z. Zhu, X. Roy, S. N. Khanna and K. H. Bowen, *The Journal of Physical Chemistry C*, 2019, **123**, 25121–25127.

91 A. C. Reber, V. Chauhan, D. Bista and S. N. Khanna, *Nanoscale*, 2020, **12**, 4736–4742.

92 D. Bista, V. Chauhan, T. Sengupta, A. C. Reber and S. N. Khanna, *Nanoscale*, 2020, **12**, 12046–12056.

93 D. Bista, T. Sengupta, A. C. Reber and S. N. Khanna, *J. Phys. Chem. A*, , DOI:10.1021/acs.jpca.0c10262.

94 J. Yang, F. Wang, J. C. Russell, T. J. Hochuli, X. Roy, M. L. Steigerwald, X. Zhu, D. W. Paley and C. Nuckolls, *Journal of the American Chemical Society*, 2020, **142**, 11993–11998.

95 A. Kramida, Y. Ralchenko and J. Reader, *NIST Atomic Spectra Database (Ver. 5.7. 1); National Institute of Standards and Technology: Gaithersburg, MD, USA, 2019*, .

96 M. P. Marder, *Condensed matter physics*, John Wiley & Sons, 2010.

97 S. Nagasaka and T. Kojima, *Journal of the Physical Society of Japan*, 1987, **56**, 408–414.

98 J. P. Perdew, *International Journal of Quantum Chemistry*, 1985, **28**, 497–523.

99 J. M. Crowley, J. Tahir-Kheli and W. A. Goddard III, *The journal of physical chemistry letters*, 2016, **7**, 1198–1203.

100 H. Xiao, J. Tahir-Kheli and W. A. Goddard III, *The Journal of Physical Chemistry Letters*, 2011, **2**, 212–217.

101 H. R. Banjade, J. Pan and Q. Yan, *Physical Review Materials*, 2021, **5**, 014005.

102 S. N. Khanna and A. C. Reber, *Nature Chemistry*, 2017, **9**, 1151–1152.

Chapter 5

A ligand-induced homojunction between aluminum-based superatomic clusters

This chapter is somewhat like an extension of the previous chapter on the fused dimer. We wanted to broaden that the dimer formation is not only limited to the metal-chalcogenide clusters but can also be extended to the simple metallic clusters, as we know that simple metal clusters are fairly established from the research of the past few decades. However, the direct fusion of two simple metallic clusters (aluminum-based clusters) leads to coalescence, and an organometallic linker is needed to link two simple metal clusters. Once the dimers are formed, the electronic levels in the dimer can be controlled by using organic ligands and the external electric field. Furthermore, the dimer consisting of simple metal clusters showed potential for photovoltaics application.

This chapter has been reproduced from the article which I co-authored. It has been slightly adapted for readability in the context of my dissertation but has not been changed in any way affecting the data, meaning, or interpretation and adapted from *Nanoscale* 2020, **12**, 12046-12056. Copyright (2020) Royal Chemical Society.

Introduction

A superatomic cluster formed by joining two metallic clusters through an organometallic bridge can behave like a semiconductor. Moreover, the addition of ligands can induce a significant shift between the conduction and valence band edges across the inter-cluster interface. The N-ethyl-2-pyrrolidone ligands induce the band alignment, and the location of the ligands strongly affects the direction of the dipole moment, including the case where the dipole moment is parallel to the inter-cluster interface. This provides an alternative strategy for constructing nanometer-scale electronic

interfaces. The semiconducting features in the PAl$_{12}$ clusters emerge from the grouping of the quantum states in a confined nearly free electron gas that creates a substantial energy gap. An organometallic Ge(CH$_3$)$_2$(CH$_2$)$_2$ bridge links the clusters while maintaining the cluster's electronic shell structure. The amount of band shifting between the bridged clusters can be changed by controlling the number of ligands. Attaching multiple ligands can result in the valence band edge of one cluster being aligned with the conduction band edge of the other bridged cluster. Similarly, the band shift across two linked metallic clusters can also be modulated by the external homogeneous electric field. Furthermore, the singly ligated bridged superatomic molecule exhibits promising features to separate the electron-hole pairs for photovoltaic applications.

Band alignment at the diode interface takes place by stacking two semiconductor materials in bulk: a p−type semiconductor carrying an excess of holes and an n−type semiconductor with an excess of electrons.[1–4] The difference in their chemical potentials causes diffusion of charge carriers that generate an internal electric field.[5–10] Consequently, an in-built potential accompanied by an internal electric field at the interface results in a directional electrical current under an applied external bias voltage. Several kinds of p−n junctions in two dimensions have been proposed; for example, two 2D materials joined at the same plane provide the lateral junction while face-to-face stacking of materials leads to a vertical junction.[11–13] An attractive alternative way is to use electronics based on single molecules or clusters. Such systems exhibit valuable and unusual properties such as current rectification, photovoltaics, electronic switching, and negative differential resistance (NDR).[14–25] The majority of such research has focused on molecular rather than cluster-based materials. This work investigates the possibilities of connecting simple metal clusters that attain closed electronic shells and test the hypothesis that significant band alignment in these systems may occur through ligand attachments and the application of external fields.

In this study, we link two metallic clusters with the open-electronic shell using an organometallic linker. Simple metallic clusters can have large HOMO-LUMO gaps because the quantum states in small symmetric clusters are bunched into electronic shells due to the quantum confinement.[26] The quantum confinement leads to quantum states with orbital character 1S, 1P, 1D… resembling the s, p, d.. states in atoms, where the uppercase letters are used to denote states in clusters while the lower case letters are used for atoms.[26–29] Research over the past thirty years has shown that the shell structure controls electronic, magnetic, optical, and chemical behavior.[30–36] Extensive work has shown that the electronic structure of aluminum clusters can be fairly rationalized in terms of a confined free electron gas.[37–39] Aluminum is trivalent; hence, the PAl_{12} cluster has 41 valence electrons corresponding to a closed shell structure of $1S^2$, $1P^6$, $1D^{10}$, $2S^2$, $1F^{14}$, $2P^6$ with an extra electron past the filled shell. Attachment of a bridging molecule to the PAl_{12} cluster results in a covalent bond, which reduces the effective electron count to 40 valence electrons in the cluster, maintaining a closed electronic shell with a large HOMO-LUMO (HL) gap. Two PAl_{12} clusters are combined by a $Ge(CH_2)_2(CH_3)_2$ linker, representing an unsaturated version of a tetra-methyl germanium $Ge(CH_3)_4$, to form a bridged superatomic cluster, $PAl_{12}[CH_2CH_3GeCH_3CH_2]PAl_{12}$. We further show that such a bridged metallic cluster marked by a large gap can emulate semiconducting features arising from quantum confinement.

Generally, the chemical potentials of clusters are governed by the position of the HOMO and LUMO levels that in turn affect the electronic characteristics like the ionization energy and electron affinity. Recently, we have shown that the position of HOMO or LUMO levels in a variety of metal clusters can be tuned by using charge transfer ligands with electron-donating or accepting properties such as phosphine (PEt_3, PMe_3), CO, CN as they bond and form surface dipoles.[40–48] We have also found that fused metal-chalcogenide clusters with unbalanced ligands may create

intense internal electric fields ideal for separating electron-hole pairs in photon harvesting.[49] In this work, we have induced a diode-like shift in the conduction and valence band edges on both sides of the bridged superatomic molecule by attaching N-ethyl-2-pyrrolidone (EP=$C_6H_{11}NO$) ligands on one of the PAl_{12} clusters. We have previously shown that EP ligands raise the chemical potential of the cluster, making it an effective donor without changing the electronic shell structure.[50] The proposed bridged superatomic molecule shows pronounced band alignment. The valence band edge of the donor cluster (ligated cluster) becomes aligned with the conduction band edge of the non-ligated cluster. A unique feature of this arrangement is that the placement of the ligands primarily determines the direction of the dipole moment so that the net dipole moment may be parallel to the inter-cluster interface. Independent of the placement of the ligands, a significant shift in the band energies on both sides of the interface occurs. Finally, an examination of the optical spectra of our proposed bridged superatomic molecule reveals that the electrons and holes on each side of the inter-cluster interface are well-separated.

Results and discussion

Controlling the HOMO and LUMO via Ligands

Our discussion starts with a brief review of modulation of the position of energy levels invoked by ligands. To show that the effect is general, we have investigated the impact of the EP ligand on the electronic states of Al_{13} and PAl_{12} clusters. Metallic clusters with 40 valence electrons are found to have a closed electronic shell. Hence, the Al_{13} cluster, with 39 valence electrons, can be considered a halogen, while the PAl_{12} cluster, with 41 valence electrons, behaves like an alkali. Figure 5.1 shows the optimized ground-state structures of bare, and the EP ligated Al_{13} and PAl_{12} clusters and their corresponding one-electron energy. We find that the effective valence electron count or the electronic configuration of Al_{13} and PAl_{12} is not altered by attaching an EP ligand.

For example, Al_{13} and Al_{13}(EP) are both one electron short of a closed electronic shell. The last unfilled orbitals are 2P states (43 MO^β and 20 MO^β), leading to an open-shell electronic configuration $1S^2$, $1P^6$, $1D^{10}$, $2S^2$, $1F^{14}$, $2P^5$. A similar phenomenon is observed in PAl_{12} and PAl_{12}(EP), both having one extra electron past the closed electronic shell, with the last filled orbitals in both clusters being $1G^1$. However, upon ligation, there is a pronounced upward shift in the entire electronic spectrum of Al_{13} and PAl_{12}, where the HOMO level of Al_{13} is raised by 0.63 eV while in the PAl_{12} the HOMO level is increased by 0.59 eV. The raising of the electronic
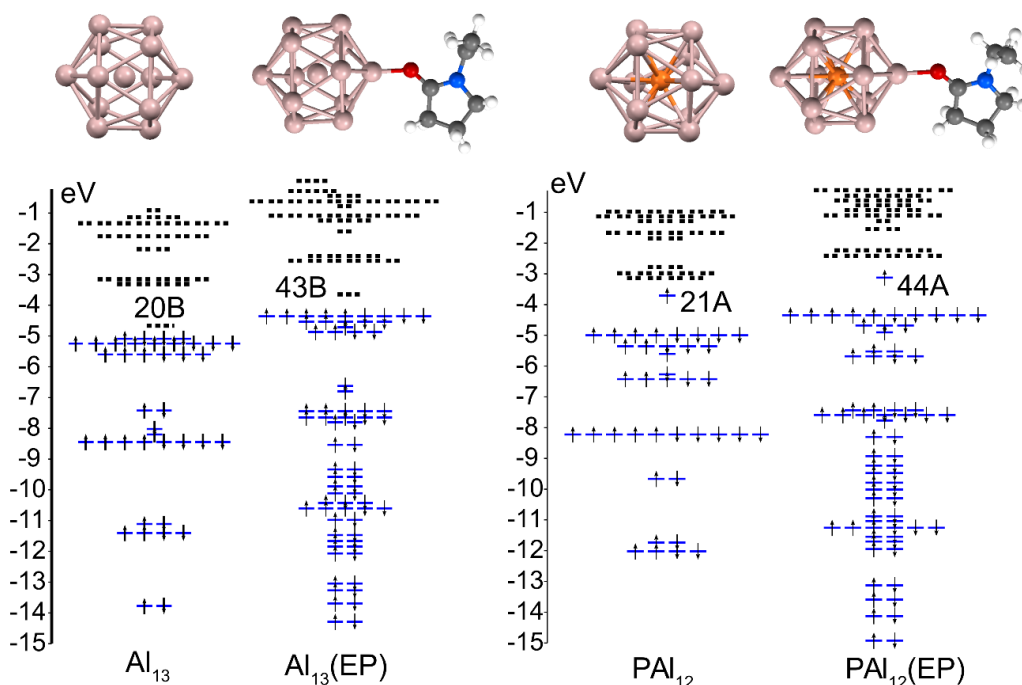
Figure 5.1 One-electron energy levels of bare and EP ligated Al_{13} and PAl_{12} clusters. Solid and dashed lines represent the occupied and unoccupied energy levels, respectively. The arrows represent the occupation of up and down spin states.

spectrum can be partly understood from the increased charge density in the core due to the electron-donating nature of the EP ligand. A Hirshfeld charge analysis confirms a gross charge of -0.369 e⁻ and -0.349 e⁻ on Al_{13} and PAl_{12} clusters, respectively, in the presence of EP ligand. The ligated

114

clusters show the decrease in adiabatic ionization energy (AIE) relative to the bare clusters as the HOMO levels of the ligated clusters are raised in energy. One of the entities of our interest in the current work is the dipole moment of the ligated clusters due to local charge transfer. Al_{13}(EP) and PAl_{12}(EP) have dipole moments of 14.16 and 13.91 Debye, respectively pointing from cluster to the EP ligand, which confirms the donor nature of the ligand.

Superatomic clusters and Ge Bridge ($CH_3CH_3GeCH_3CH_3$) molecule

To examine our hypothesis that ligands may induce significant band alignment between two bridged metallic superatoms. Two metallic superatom clusters coalesced when they are linked directly, unlike the metal chalcogenides clusters. Hence, we first need to identify a way for linking two metallic superatom clusters. An organometallic linker, tetramethyl germanium ($Ge(CH_3)_4$) offered the possibility to connect two metallic superatomic clusters. This organometallic species has insulator-like properties, a very high HL gap of 6.23 eV and an adiabatic IE of 8.75 eV. It is observed that the removal of one H atom from a CH_3 group leaves an unsaturated carbon, which binds the linker to the clusters through σ-bonding. The notation is made simpler by denoting $-CH_2CH_3GeCH_3CH_3$ linker as Ge^1_B, while Ge^2_B means the linker $-CH_2CH_3GeCH_3CH_2-$. The subscript 'B' represents that the Ge-linker is acting as a bridge between two clusters. Three metallic clusters, namely, MAl_{12}, (M = C, P, and Al) are chosen as possible motifs to form the bridged superatomic molecule with Ge-linker. The $CAl_{12}Ge^1_B$ cluster turns out to be an open-shell system with a small HOMO-LUMO gap of 0.51 eV. $Al_{13}Ge^1_B$ is found to be a closed-shell system with a relatively high HOMO-LUMO gap of 1.45 eV. However, Al_{13} does not retain its icosahedron structure in the ground state of $Al_{13}Ge^1_B$. On the other hand, attaching Ge^1_B to the PAl_{12} cluster also results in a closed shell system with the highest HOMO-LUMO gap of 1.65 eV showing

enhanced chemical stability among all the $MAl_{12}Ge^1_B$. Hence, the PAl_{12} cluster is favored as a suitable motif for building the bridged superatomic molecule. The binding energy (BE) is calculated using the following equation:

$$BE = E[PAl_{12}] + E[Ge^1_B] - E[PAl_{12}Ge^1_B] \qquad (5.1)$$

where, E is the total energy of the respective system. We have found that Ge^1_B strongly binds with the PAl_{12} cluster with a BE of 2.85 eV. The PAl_{12} cluster has 41 valence electrons, and the higher value of BE between the PAl_{12} cluster and Ge^1_B is attributed to the polar-covalent Al-C bonding that localizes one electron from the PAl_{12} valence pool. Hence, PAl_{12} attains a filled valence shell of 40 electrons leading to its electronic shell closure and a high HOMO-LUMO gap of 1.65 eV when bonding to the Ge-linker.

Ge^2_B Bridged superatomic molecule $PAl_{12}[Ge^2_B]PAl_{12}$

We then designed a bridged superatomic molecule in which two identical PAl_{12} superatoms are linked through an organometallic linker, Ge^2_B. Figure 5.2 shows the optimized ground state structure of $PAl_{12}[Ge^2_B]PAl_{12}$. The bridged superatomic molecule turns out to have a large HOMO-LUMO gap of 1.53 eV. To see whether its electronic structure can be described by nearly free electrons gas, we have analyzed the molecular orbitals of $PAl_{12}[Ge^2_B]PAl_{12}$. Figure 5.2 reveals a unique feature of the electronic structure of $PAl_{12}[Ge^2_B]PAl_{12}$ in which each PAl_{12} cluster maintains its closed electronic shell structure with 40 valence electrons. It is important to highlight that this feature can be attributed to the presence of Ge-linker. The bridged superatomic molecule has a relatively high AIE of 5.66 eV and a relatively low AEA of 2.16 eV.
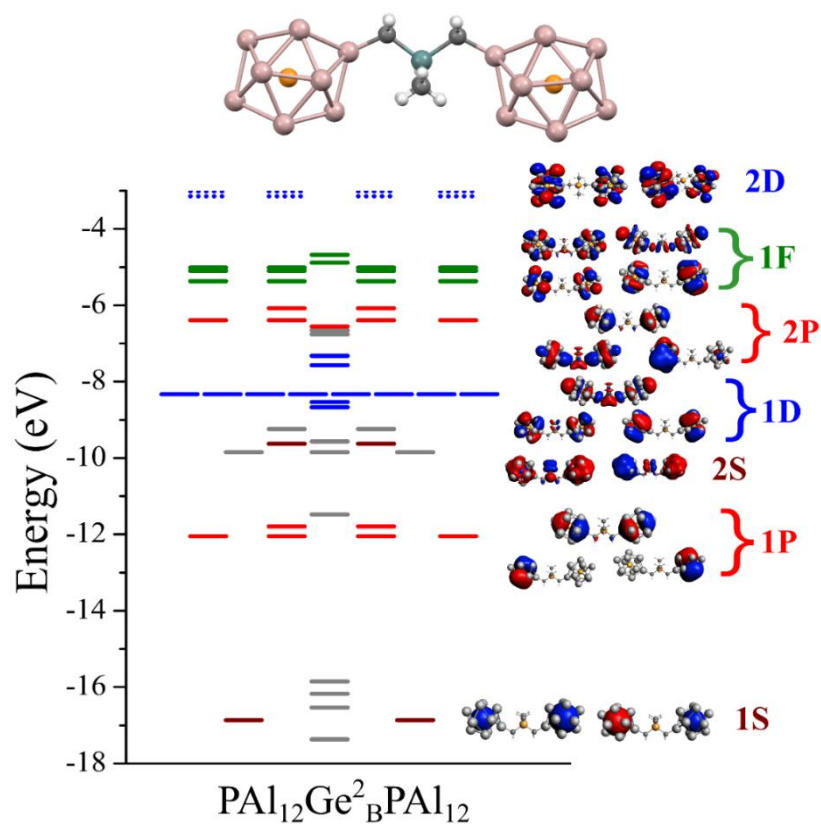
Figure 5.2 Optimized ground-state structure and electronic structure of bridged superatomic molecule $PAl_{12}[Ge^2_B]PAl_{12}$. Solid and dashed lines represent the occupied and unoccupied energy levels, respectively. The color-coding indicates the type of delocalized orbitals, and gray indicates orbitals localized on the Ge linker. Only a few delocalized molecular orbitals of P, D, and F characters are shown for clarity.

In Figure 5.3, we show the projected density of states of the bridged superatomic molecule corresponding to PAl_{12}, Ge^2_B, and PAl_{12} components and the one-electron energy levels of the bridged superatomic molecule. Interestingly, the HOMO of the bridged molecule is found to be -4.68 eV, and a HOMO-LUMO gap of 1.53 eV marks each PAl12 cluster. The HOMO level is significantly lower than the bare PAl_{12} (-3.72 eV), confirming that the bridged superatomic molecule no longer has alkali-like superatomic behavior of the bare PAl_{12} cluster.
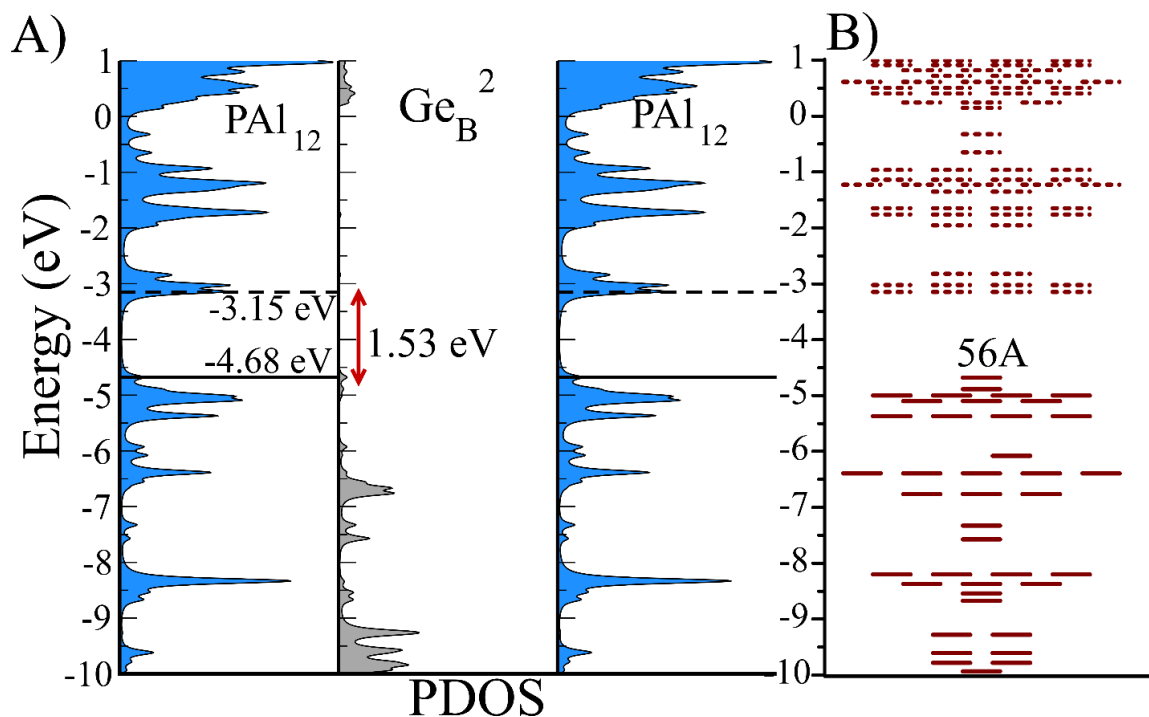
Figure 5.3 A) Partial density of states (PDOS) and B) One-Electron energy levels of PAl$_{12}$[Ge^2$_B$]PAl$_{12}$ molecule. Solid and dotted lines represent occupied and unoccupied levels, respectively.

Effect of EP ligand on the Electronic Structure of the Superatomic Molecule

As we have discussed earlier that the addition of ligands can modulate the chemical potential of the clusters, we next examine whether that can also induce an internal electric field in our bridged superatomic molecule. We start with binding an EP ligand to one of the PAl$_{12}$ clusters to form (EP)PAl$_{12}$Ge^2$_B$PAl$_{12}$ molecule. The relative energy and structures of *ortho*, *meta*, and *para* (EP)PAl$_{12}$Ge^2$_B$PAl$_{12}$ showed that the *ortho*–isomer is found to be the most stable while *meta*– and *para*–isomers are 0.06 and 0.65 eV higher in energy, respectively. The most stable configuration has the EP ligand pointing parallel to the inter-cluster interface. The para is relatively unstable because the binding of the organometallic linker has induced a charge donating active site on the opposite side of the cluster that reduces the binding of the charge donating EP ligand.[54,55]

118
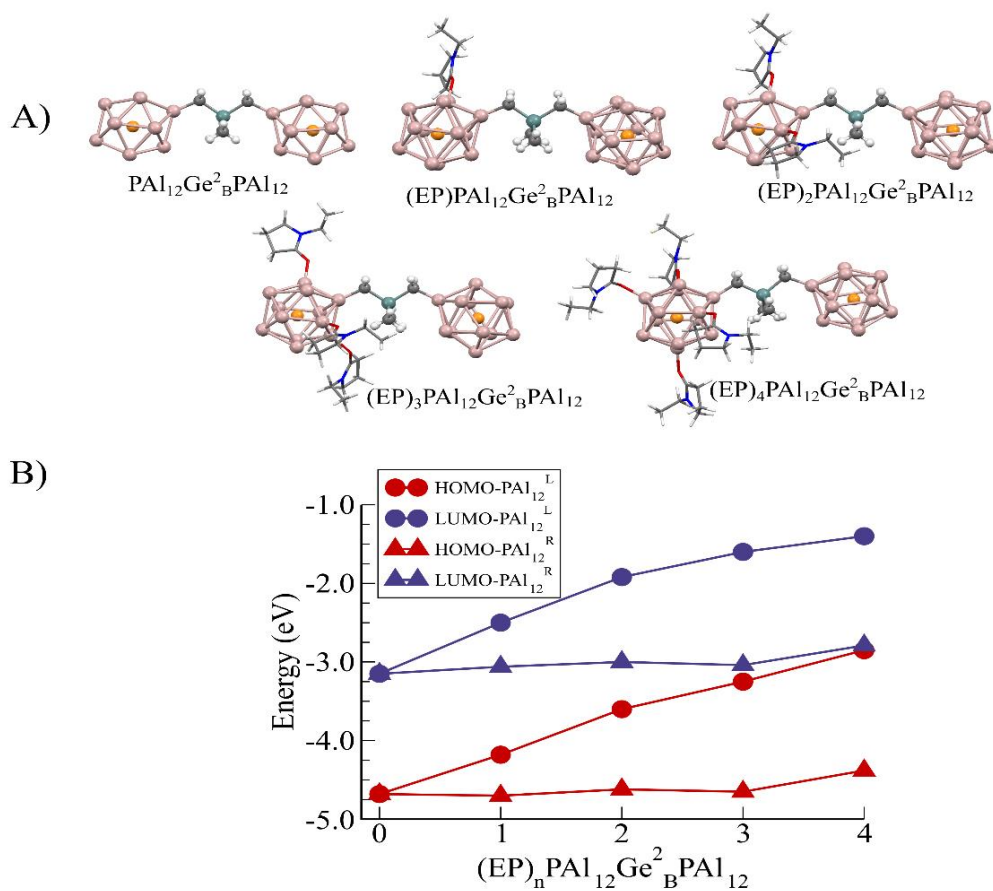
Figure 5.4 A) Ground state structures of $(EP)_nPAl_{12}[Ge^2_B]PAl_{12}$ for n = 0-4 and B) HOMO-LUMO levels in left $(PAl_{12}{}^L)$ and right $(PAl_{12}{}^R)$ clusters of $(EP)_nPAl_{12}Ge^2_BPAl_{12}$ for n = 0-4 respectively.

We subsequently added two, three, and four EP ligands to form ligated $(EP)_nPAl_{12}Ge^2_BPAl_{12}$ molecules, as shown in Figure 5.4A). The binding energies of the successive EP ligands are 0.91, 0.79, 0.56, and 0.32 eV, respectively. The EP ligands bind to the aluminum sites of PAl_{12} clusters through their oxygen atoms. While the binding energies are modest, there can be a significant effect on the electronic structure of the bridged superatomic clusters. The addition of ligands changes the position of the HOMO, indicating a shift in the chemical potential. Figure 5.4B) shows that the successive addition of four EP ligands raises the HOMO by 0.50, 0.58, 0.35, and 0.40 eV, respectively, from the previous size resulting in a total change of 1.83 eV. The electronic properties

119

of the $(EP)_nPAl_{12}Ge^2_BPAl_{12}$, for n=1-4, are given in Table 1. The rise in the HOMO is exclusively due to the orbitals that are located on the ligated cluster. The rise in HOMO leads to a monotonic decrease in the AIE, which decreases from 5.66 eV to 3.70 eV in going from zero to four ligands on the left PAl_{12} cluster ($PAl_{12}{}^L$). This is because higher is the HOMO, more easily a species can be ionized. However, the change in the AEA is not entirely monotonical, as shown in Table 5.1.

The superatomic molecule with one ligand, $(EP)PAl_{12}Ge^2_BPAl_{12}$, is found to have a large dipole moment of 14.32 Debye; however, all this dipole is pointed from the cluster to the EP ligand, perpendicular to the molecular axis and parallel to the inter-cluster interface. In a standard p-n junction, the n-type side is positively charged, and the p-type side is negatively charged causing an internal dipole to point from p-type to n-type. Therefore, one would expect the dipole to be pointed towards the ligated cluster. However, as seen in Table 5.1, the dipole along the supermolecular axis is merely -1.27 Debye, which represents the dipole pointing towards the ligated cluster. The strong electron-donating nature of EP is so dominating that almost all the dipole moment in $(EP)PAl_{12}Ge^2_BPAl_{12}$ points from the cluster to the EP ligand. Figure 5.5 shows the magnitude and direction of dipole moment vectors in $(EP)_nPAl_{12}Ge^2_BPAl_{12}$ for n = 1-4. In the case with 2 and 3 EP ligands, the z-component of the dipole moment points back towards the "p-type" non-ligated cluster that should be negatively charged. The addition of the fourth EP ligand makes dipole moment perpendicular to the inter-cluster interface, dipole pointing from the non-ligated to the ligated side with a value of 8.55 Debye, out of a total dipole moment of 8.78 Debye. To determine if charge transfer is occurring across the cluster-cluster interface, we investigated the charging across the cluster as a function of the number of EP ligands.
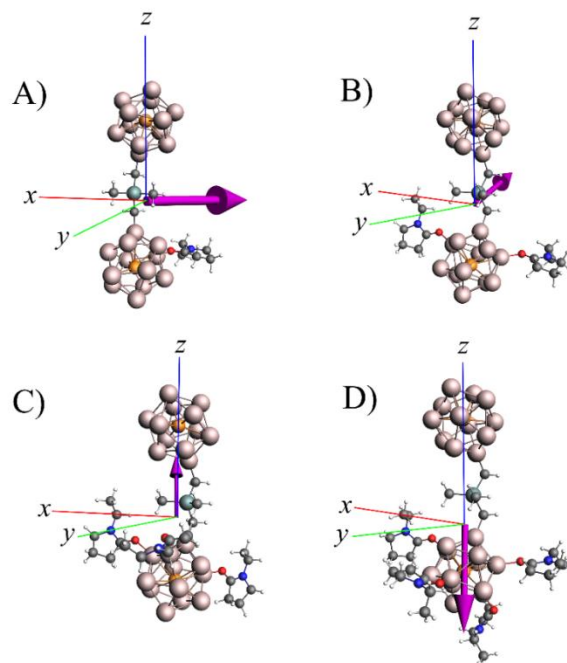
Figure 5.5 The dipole moment vector in $(EP)_n PAl_{12}[Ge^2_B]PAl_{12}$ for n=1-4. The pink arrow represents the magnitude and direction of the total dipole moment vector. The origin of the cartesian-axes is taken at the center of mass of each system.

We found that the net charge on the ligated side of the cluster monotonically increases from +0.18 e⁻, and reaches to +0.23 e⁻, +0.26 e⁻, +0.29 e⁻, and +0.32 e⁻, as the EP ligands are successively added. This confirms that the cluster units are behaving like a p−n junction; however, the direction of the net dipole is driven by the coordination of the ligand. Another exciting feature of the ligated bridged superatomic molecule is the HOMO-LUMO gap that decreases from 1.53 eV for the non-ligated system to 0.06 eV for the molecule with 4 ligands. As shown earlier, the addition of ligands changes the positions of HOMO and LUMO without significantly affecting the HOMO-LUMO gap[43]; however, our current result indicates a monotonic decrease in the HOMO-LUMO gap with the gap almost disappearing when 4 ligands are attached to one side of the bridged superatomic molecule. Is there a contradiction?

Table 5.1 The electronic properties of $(EP)_nPAl_{12}Ge^2_BPAl_{12}$, for n=1-4. The total dipole moment and their x-, y-, and z- components are also given in Debye.

$(EP)_nPAl_{12}Ge^2_BPAl_{12}$	HOMO-LUMO Gap	AIP	AEA		Dipole Moment	D_x	D_y	D_z
	(eV)				(Debye)			
0	1.53	5.66	2.16		0.97	0.03	-0.97	0.00
1	1.13	5.21	2.43		14.37	-7.61	-12.13	-1.27
2	0.60	4.70	1.96		8.82	2.34	-8.28	1.93
3	0.21	4.19	2.13		5.62	0.91	-2.05	5.16
4	0.06	3.70	2.00		8.78	-1.45	1.36	-8.55

To resolve this apparent paradox and characterize the molecule's nature, we now examine the electronic structure in more detail. We projected the density of states (DOS) of the ligand, the left cluster (PAl_{12}^L), bridge (Ge^2_B), and the cluster on the right side (PAl_{12}^R). For the symmetric superatomic molecule without ligands, the PDOS on the left and right PAl_{12} is marked by a gap of 1.53 eV, as discussed earlier. appreciable change in the HOMO-LUMO gap of the orbitals on that cluster (PAl_{12}^L). However, the LUMO of the PAl_{12}^R becomes the effective LUMO of the combined system. This leads to an apparent decrease in the HOMO-LUMO gap even though the PDOS on each side is marked by large HOMO-LUMO gaps. As seen in Figure 5.6, for one EP ligand, the HOMO shifts up by 0.52 eV, and LUMO shifts up by 0.56 eV. With the successive addition of EP ligands, the shift of the HOMO increases to 1.02 eV, 1.40 eV, and 1.53 eV, respectively.
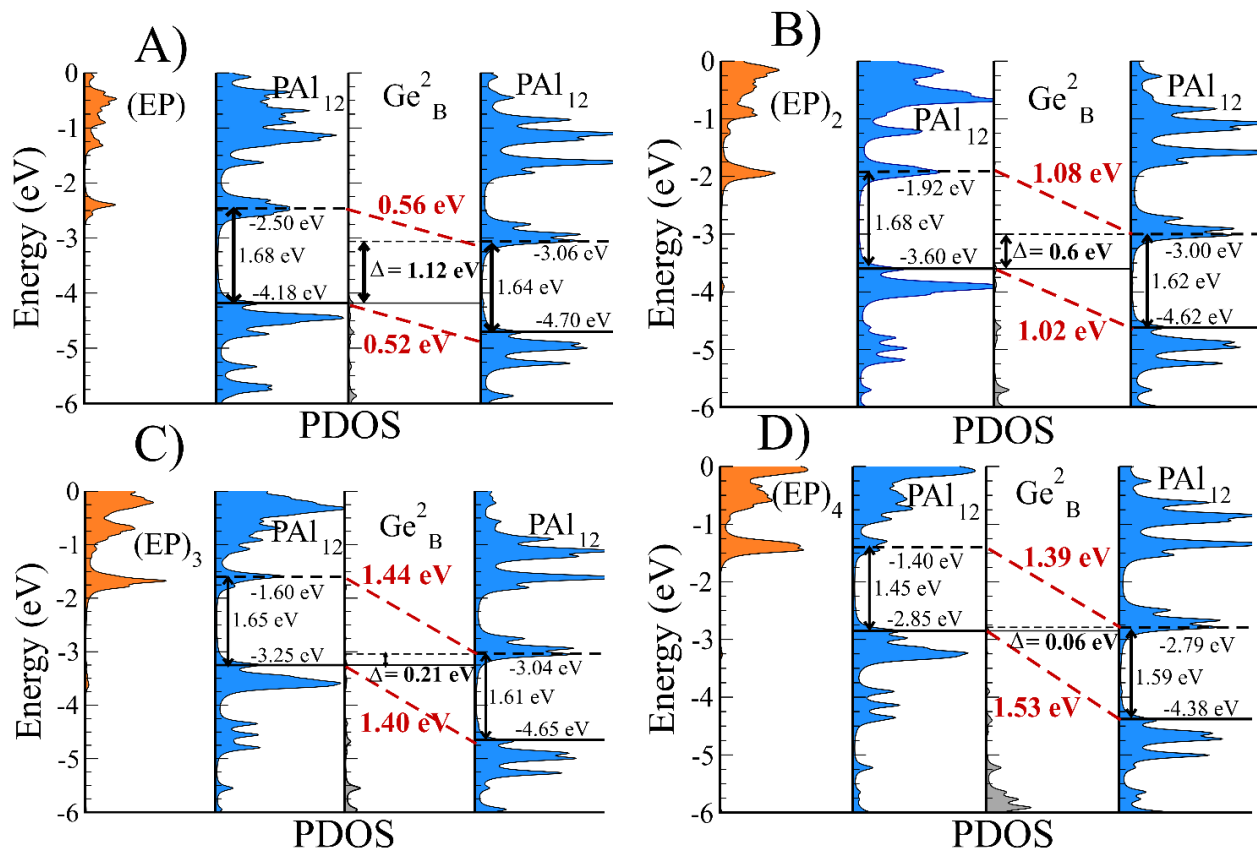
Figure 5.6 The density of states of the $(EP)_n PAl_{12}[Ge^2_B]PAl_{12}$ for n=1-4. The projected density of states of both sides of the cluster are plotted separately with the ligated cluster on the left, and the non-ligated on the right. The red dotted lines indicate the shift of the HOMO and LUMO levels across the intercluster interface. HOMO-LUMO gaps in eV are given by Δ.

This process results in an apparent decrease in the HOMO-LUMO gap as the HOMO and LUMO are located at different clusters. More importantly, the combination now shows the PDOS on the PAl_{12}^L is raised compared to the PAl_{12}^R, the hallmark of the p-n junction. One remarkable feature of the ligated bridged superatomic molecule with 3 and 4 EP ligands is that the HOMO of the ligated cluster becomes nearly aligned with the LUMO of the non-ligated cluster.

Electric Field Effects

To better understand the band alignment that is occurring across the inter-cluster interface, we have applied an external homogeneous electric field perpendicular to this interface. The z-axis of the superatomic molecule is aligned perpendicular to the interface, with the origin of the cartesian coordinate placed at the center of mass of the whole molecule. The uniform external field is applied from the center of mass of the superatomic molecule along +/- z-axes. This allows us to compare the effective band alignment induced by the ligands to the band alignment caused by the voltage drop due to the external homogeneous electric field. The shift is symmetric over both directions of the applied field for $PAl_{12}[Ge^2{}_B]PAl_{12}$, as shown in Figure 5.7A. An electric field of -0.0036 a.u. (Hartree/e Bohr) results in a full band alignment in which the HOMO of $PAl_{12}{}^L$ aligns with the LUMO of the $PAl_{12}{}^R$. Likewise, 0.0036 a.u. aligns HOMO of the $PAl_{12}{}^R$ to the LUMO of the $PAl_{12}{}^L$. This corresponds to a voltage drop of about 3.2 V across the two PAl_{12} clusters to fully align the HOMO and LUMO. In the case of the ligated superatomic molecule, $(EP)PAl_{12}[Ge^2{}_B]PAl_{12}$, we see that the bands are not aligned at the zero electric fields. An approximate electric field of 0.001 a.u. needs to be applied to align the HOMO of the left and right clusters. As shown in Figure 7B), it requires an electric field of -0.0026 a.u, which corresponds to 2.3 V, to align HOMO of $PAl_{12}{}^L$ with LUMO of $PAl_{12}{}^R$. Hence, the effective voltage shift across the cluster due to the addition of a single EP ligand is about 0.9 V. Similarly, the HOMO of $PAl_{12}{}^R$ can be also aligned with the LUMO of the ligated $PAl_{12}{}^L$ cluster. However, a larger (almost twice) electric field of +0.005 a.u, which correspond to voltages of 4.4 V, is required. These results confirm that the addition of the EP ligand produces an asymmetric bias in the response of the band alignment when a voltage is placed across the bridged superatomic molecule.
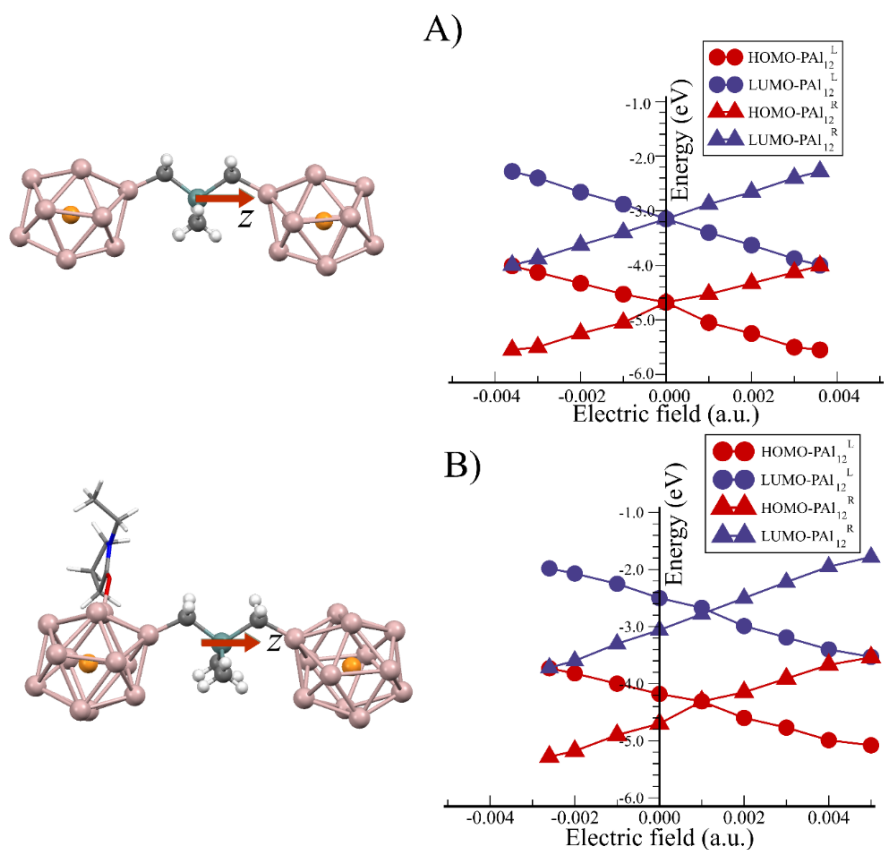
Figure 5.7 **A**) The energies of the HOMO and LUMO on the left and right cluster in $PAl_{12}(Ge^2{}_B)PAl_{12}$ as a function of an electric field along the shown z-axis. B) The energies of the HOMO and LUMO on the $PAl_{12}{}^L$ and $PAl_{12}{}^R$ clusters in $(EP)PAl_{12}(Ge^2{}_B)PAl_{12}$ as a function of an electric field along the shown z-axis.

Optical Absorption of $(EP)PAl_{12}Ge^2{}_BPAl_{12}$

We now examine the potential of the bridged superatomic molecule to separate the electron-hole pairs for photovoltaic applications. Our earlier studies suggest that for a fused cluster to qualify for photovoltaics, the system should have the following three attributes: (i) a large dipole moment to separate electron-hole pairs, (ii) The holes and electrons should be localized at different regions

of the superatomic unit, and (iii) The optical gap must be greater than the HOMO-LUMO gap of the system, which would show that the electron-hole recombination is unlikely.[49] The spin density of cationic and anionic states of $(EP)PAl_{12}Ge^2{}_BPAl_{12}$ exhibit that the electron and holes are located at different regions of the bridged superatomic molecule, as shown in Figure 5.8A). The absorption spectrum of the molecule using time-dependent density functional theory is also shown in Figure 5.8B). The lowest energy excitation is 1.127 eV; however, the effective optical gap is around 1.70 eV. Transitions near the HOMO-LUMO gap turn out to have negligible oscillator strengths. Figure 5.8C) displays the lowest four excitations: HOMO→LUMO, HOMO→LUMO+1, HOMO→LUMO+2, and HOMO→LUMO+3. All the HOMOs from where electron gets excited leaving behind holes are the superatomic states associated with ligated PAl_{12} part, and the corresponding states where excited electron stay are the states over the non-ligated PAl_{12} part of the molecule. These excitations are optically very weak, leading to a low probability of electron-hole recombination. The presence of a Ge linker as a bridge between two clusters is crucial for electron-hole separation in metallic clusters. This could be understood from the fact that electronic states directly fused two metallic clusters without bridging molecule span over the combined system due to its delocalized nature, minimizing the probability of the electron-hole separation. Furthermore, the addition of the EP ligand results in band alignment, that changes the alignment of the frontier orbitals of the bridged clusters. Hence, such a bridged metallic superatomic molecule provides an alternative route to create separated electron-hole pairs for light harvesting.
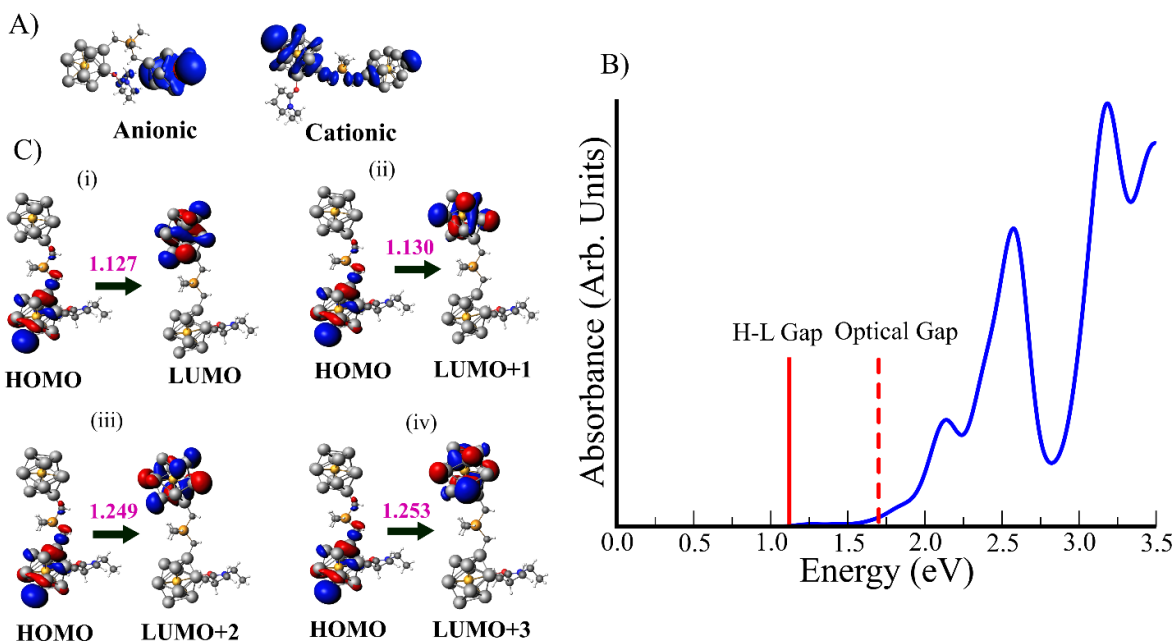
Figure 5.8 A) The spin density on the $(EP)PAl_{12}Ge^2_BPAl_{12}$ cluster to show the location of the electron and electron-hole. B) The optical absorption spectra and C) the orbitals corresponding to the low energy excitations that could cause electron-hole pair recombination. The excitation energies are given in eV and are represented in pink.

Conclusions

The present studies show how the quantum gaps in metallic clusters associated with the quantum confinement of a nearly free electron gas can form a well-defined band gap system. The bridged superatomic molecule, $PAl_{12}[Ge^2_B]PAl_{12}$, is a possible model for such a device made out of metallic clusters. The Ge organometallic linker prevents the coalescing of the metallic clusters. The PAl_{12} clusters have one more valence electron than a closed electronic shell, so by bonding with the linker, the cluster attains a closed electronic shell. Hence, the germanium linker separates

the individual clusters into two separate branches and provides electronic stability. Once the clusters are stable and well separated, we can add ligands to alter the electronic structure. One of the unique features of the current proposal is how the addition of charge transfer ligands may alter and tune the chemical potential of the individual clusters. The addition of the EP ligand raises the bands of the cluster, on which the ligand is bound, leading to a shift in the alignment of bands across the inter-cluster interface. The dipole moment in such a device is driven by the direction of the ligand-cluster bond, so the net dipole moment of the system can vary from parallel to perpendicular to the inter-cluster interface, depending on the direction of the bonding. The unit, $(EP)PAl_{12}[Ge^2_B]PAl_{12}$, is an intriguing system for photon harvesting because the band alignment within the cluster may prevent the recombination of electron-hole pairs. These results reveal an alternative strategy for engineering internal electric fields at the scale of a single nanometer.

References

1 Z. Zhang and J. T. Yates, Band Bending in Semiconductors: Chemical and Physical Consequences at Surfaces and Interfaces, *Chem. Rev.*, 2012, **112**, 5520–5551.

2 M. Alonso, R. Cimino and K. Horn, Surface photovoltage effects in photoemission from metal-GaP(110) interfaces: Importance for band bending evaluation, *Phys. Rev. Lett.*, 1990, **64**, 1947–1950.

3 M. Foussekis, J. D. McNamara, A. A. Baski and M. A. Reshchikov, Temperature-dependent Kelvin probe measurements of band bending in p-type GaN, *Appl. Phys. Lett.*, 2012, **101**, 082104.

4 A. C. Reber, S. N. Khanna, F. S. Roberts and S. L. Anderson, Effect of O2 and CO Exposure on the Photoelectron Spectroscopy of Size-Selected Pdn Clusters Supported on TiO2(110), *J. Phys. Chem. C*, 2016, **120**, 2126–2138.

5 W. Shockley and H. J. Queisser, Detailed Balance Limit of Efficiency of p-n Junction Solar Cells, *J. Appl. Phys.*, 1961, **32**, 510–519.

6 L. M. Terman, An investigation of surface states at a silicon/silicon oxide interface employing metal-oxide-silicon diodes, *Solid-State Electron.*, 1962, **5**, 285–299.

7 S. J. Jiao, Z. Z. Zhang, Y. M. Lu, D. Z. Shen, B. Yao, J. Y. Zhang, B. H. Li, D. X. Zhao, X. W. Fan and Z. K. Tang, ZnO p-n junction light-emitting diodes fabricated on sapphire substrates, *Appl. Phys. Lett.*, 2006, **88**, 031911.

8 N. Yaacobi-Gross, M. Soreni-Harari, M. Zimin, S. Kababya, A. Schmidt and N. Tessler, Molecular control of quantum-dot internal electric field and its application to CdSe-based solar cells, *Nat. Mater.*, 2011, **10**, 974–979.

9 M.-Y. Li, Y. Shi, C.-C. Cheng, L.-S. Lu, Y.-C. Lin, H.-L. Tang, M.-L. Tsai, C.-W. Chu, K.-H. Wei, J.-H. He, W.-H. Chang, K. Suenaga and L.-J. Li, Epitaxial growth of a monolayer WSe2-MoS2 lateral p-n junction with an atomically sharp interface, *Science*, 2015, **349**, 524–528.

10 Q. Kong, W. Lee, M. Lai, C. G. Bischak, G. Gao, A. B. Wong, T. Lei, Y. Yu, L.-W. Wang, N. S. Ginsberg and P. Yang, Phase-transition–induced p-n junction in single halide perovskite nanowire, *Proc. Natl. Acad. Sci.*, 2018, **115**, 8889–8894.

11 M.-Y. Li, C.-H. Chen, Y. Shi and L.-J. Li, Heterostructures based on two-dimensional layered materials and their potential applications, *Mater. Today*, 2016, **19**, 322–335.

12 Z. Zhang, P. Chen, X. Duan, K. Zang, J. Luo and X. Duan, Robust epitaxial growth of two-dimensional heterostructures, multiheterostructures, and superlattices, *Science*, 2017, **357**, 788–792.

13 M. Mahjouri-Samani, M.-W. Lin, K. Wang, A. R. Lupini, J. Lee, L. Basile, A. Boulesbaa, C. M. Rouleau, A. A. Puretzky, I. N. Ivanov, K. Xiao, M. Yoon and D. B. Geohegan, Patterned

arrays of lateral heterojunctions within monolayer two-dimensional semiconductors, *Nat. Commun.*, 2015, **6**, 1–6.

14 A. Aviram and M. A. Ratner, Molecular rectifiers, *Chem. Phys. Lett.*, 1974, **29**, 277–283.

15 P. Avouris, Molecular Electronics with Carbon Nanotubes, *Acc. Chem. Res.*, 2002, **35**, 1026–1034.

16 H. B. Akkerman, P. W. M. Blom, D. M. de Leeuw and B. de Boer, Towards molecular electronics with large-area molecular junctions, *Nature*, 2006, **441**, 69–72.

17 H. He, R. Pandey, J. U. Reveles, S. N. Khanna and S. P. Karna, Highly efficient (Cs[sub 8]V) superatom-based spin-polarizer, *Appl. Phys. Lett.*, 2009, **95**, 192104.

18 H. He, R. Pandey, G. Mallick and S. P. Karna, Asymmetric Currents in a Donor−Bridge−Acceptor Single Molecule: Revisit of the Aviram−Ratner Diode, *J. Phys. Chem. C*, 2009, **113**, 1575–1579.

19 X. Zhong, R. Pandey, A. R. Rocha and S. P. Karna, Can Single-Atom Change Affect Electron Transport Properties of Molecular Nanostructures such as C60 Fullerene?, *J. Phys. Chem. Lett.*, 2010, **1**, 1584–1589.

20 L. Zhu and S. N. Khanna, Quantum spin transport through magnetic superatom dimer (Cs8V-Cs8V), *J. Chem. Phys.*, 2012, **137**, 164311.

21 L. Zhu, M. Qian and S. N. Khanna, Unusually large spin polarization and magnetoresistance in a FeMg8–FeMg8 superatomic dimer, *J. Chem. Phys.*, 2013, **139**, 064306.

22 B. Fu, M. A. Mosquera, G. C. Schatz, M. A. Ratner and L.-Y. Hsu, Photoinduced Anomalous Coulomb Blockade and the Role of Triplet States in Electron Transport through an Irradiated Molecular Transistor, *Nano Lett.*, 2018, **18**, 5015–5023.

23 N. Xin, J. Guan, C. Zhou, X. Chen, C. Gu, Y. Li, M. A. Ratner, A. Nitzan, J. F. Stoddart and X. Guo, Concepts in the design and engineering of single-molecule electronic devices, *Nat. Rev. Phys.*, 2019, **1**, 211–230.

24 B. M. Boardman, J. R. Widawsky, Y. S. Park, C. L. Schenck, L. Venkataraman, M. L. Steigerwald and C. Nuckolls, Conductance of Single Cobalt Chalcogenide Cluster Junctions, *J. Am. Chem. Soc.*, 2011, **133**, 8455–8457.

25 G. Lovat, B. Choi, D. W. Paley, M. L. Steigerwald, L. Venkataraman and X. Roy, Room-temperature current blockade in atomically defined single-cluster junctions, *Nat. Nanotechnol.*, 2017, **12**, 1050–1054.

26 W. D. Knight, K. Clemenger, W. A. de Heer, W. A. Saunders, M. Y. Chou and M. L. Cohen, Electronic Shell Structure and Abundances of Sodium Clusters, *Phys. Rev. Lett.*, 1984, **52**, 2141–2143.

27 S. N. Khanna and P. Jena, Atomic clusters: Building blocks for a class of solids, *Phys. Rev. B*, 1995, **51**, 13705–13716.

28 D. E. Bergeron, A. W. Castleman, T. Morisato and S. N. Khanna, Formation of Al13I-: Evidence for the Superhalogen Character of Al13, *Science*, 2004, **304**, 84–87.

29 A. C. Reber and S. N. Khanna, Superatoms: Electronic and Geometric Effects on Reactivity, *Acc. Chem. Res.*, 2017, **50**, 255–263.

30 D. E. Bergeron, P. J. Roach, A. W. Castleman, N. O. Jones and S. N. Khanna, Al Cluster Superatoms as Halogens in Polyhalides and as Alkaline Earths in Iodide Salts, *Science*, 2005, **307**, 231–235.

31 M. Walter, J. Akola, O. Lopez-Acevedo, P. D. Jadzinsky, G. Calero, C. J. Ackerson, R. L. Whetten, H. Grönbeck and H. Häkkinen, A unified view of ligand-protected gold clusters as superatom complexes, *Proc. Natl. Acad. Sci.*, 2008, **105**, 9157–9162.

32 P. Andre Clayborne, O. Lopez-Acevedo, R. L. Whetten, H. Grönbeck and H. Häkkinen, Evidence of superatom electronic shells in ligand-stabilized aluminum clusters, *J. Chem. Phys.*, 2011, **135**, 094701.

33 C. M. Aikens, Electronic Structure of Ligand-Passivated Gold and Silver Nanoclusters, *J. Phys. Chem. Lett.*, 2011, **2**, 99–104.

34 A. C. Reber, S. N. Khanna, P. J. Roach, W. H. Woodward and A. W. Castleman, Spin Accommodation and Reactivity of Aluminum Based Clusters with O2, *J Am Chem Soc*, 2007, **129**, 16098–16101.

35 Z. Luo, G. U. Gamboa, J. C. Smith, A. C. Reber, J. U. Reveles, S. N. Khanna and A. W. Castleman, Spin Accommodation and Reactivity of Silver Clusters with Oxygen: The Enhanced Stability of Ag13–, *J. Am. Chem. Soc.*, 2012, **134**, 18973–18978.

36 W. H. Blades, A. C. Reber, S. N. Khanna, L. López-Sosa, P. Calaminici and A. M. Köster, Evolution of the Spin Magnetic Moments and Atomic Valence of Vanadium in VCux+, VAgx+, and VAux+ Clusters (x = 3–14), *J. Phys. Chem. A*, 2017, **121**, 2990–2999.

37 J. Akola, M. Manninen, H. Häkkinen, U. Landman, X. Li and L.-S. Wang, Aluminum cluster anions: Photoelectron spectroscopy and ab initio simulations, *Phys. Rev. B*, 2000, **62**, 13216–13228.

38 Z. Luo, C. J. Grover, A. C. Reber, S. N. Khanna and A. W. Castleman, Probing the Magic Numbers of Aluminum–Magnesium Cluster Anions and Their Reactivity toward Oxygen, *J. Am. Chem. Soc.*, 2013, **135**, 4307–4313.

39 J. C. Smith, A. C. Reber, S. N. Khanna and A. W. Castleman, Boron Substitution in Aluminum Cluster Anions: Magic Clusters and Reactivity with Oxygen, *J. Phys. Chem. A*, , DOI:10.1021/jp501934t.

40 T. C. Leung, C. L. Kao, W. S. Su, Y. J. Feng and C. T. Chan, Relationship between surface dipole, work function and charge transfer: Some exceptions to an established rule, *Phys. Rev. B*, 2003, **68**, 195408.

41 V. Chauhan, A. C. Reber and S. N. Khanna, Transforming Ni9Te6 from Electron Donor to Acceptor via Ligand Exchange, *J. Phys. Chem. A*, 2016, **120**, 6644–6649.

42 A. C. Reber, V. Chauhan and S. N. Khanna, Symmetry and magnetism in Ni9Te6 clusters ligated by CO or phosphine ligands, *J. Chem. Phys.*, 2017, **146**, 024302.

43 V. Chauhan, A. C. Reber and S. N. Khanna, Metal Chalcogenide Clusters with Closed Electronic Shells and the Electronic Properties of Alkalis and Halogens, *J. Am. Chem. Soc.*, 2017, **139**, 1871–1877.

44 V. Chauhan and S. N. Khanna, Strong Effect of Organic Ligands on the Electronic Structure of Metal-Chalcogenide Clusters, *J. Phys. Chem. A*, 2018, **122**, 6014–6020.

45 G. Liu, A. Pinkard, S. M. Ciborowski, V. Chauhan, Z. Zhu, A. P. Aydt, S. N. Khanna, X. Roy and K. H. Bowen, Tuning the electronic properties of hexanuclear cobalt sulfide superatoms via ligand substitution, *Chem. Sci.*, 2019, **10**, 1760–1766.

46 A. C. Reber and S. N. Khanna, Co 6 Se 8 (PEt 3) 6 superatoms as tunable chemical dopants for two-dimensional semiconductors, *Npj Comput. Mater.*, 2018, **4**, 33.

47 A. C. Reber, D. Bista, V. Chauhan and S. N. Khanna, Transforming Redox Properties of Clusters Using Phosphine Ligands, *J. Phys. Chem. C*, 2019, **123**, 8983–8989.

48 G. Liu, V. Chauhan, A. P. Aydt, S. M. Ciborowski, A. Pinkard, Z. Zhu, X. Roy, S. N. Khanna and K. H. Bowen, Ligand Effect on the Electronic Structure of Cobalt Sulfide Clusters: A Combined Experimental and Theoretical Study, *J. Phys. Chem. C*, 2019, **123**, 25121–25127.

49 A. C. Reber, V. Chauhan, D. Bista and S. N. Khanna, Superatomic molecules with internal electric fields for light harvesting, *Nanoscale*, 2020, **12**, 4736–4742.

50 V. Chauhan, A. C. Reber and S. N. Khanna, Strong lowering of ionization energy of metallic clusters by organic ligands without changing shell filling, *Nat. Commun.*, 2018, **9**, 1–7.

51 G. te Velde, F. M. Bickelhaupt, E. J. Baerends, C. Fonseca Guerra, S. J. A. van Gisbergen, J. G. Snijders and T. Ziegler, Chemistry with ADF, *J. Comput. Chem.*, 2001, **22**, 931–967.

52 J. P. Perdew, K. Burke and M. Ernzerhof, Generalized Gradient Approximation Made Simple, *Phys. Rev. Lett.*, 1996, **77**, 3865–3868.

53 E. van Lenthe, J. G. Snijders and E. J. Baerends, The zero-order regular approximation for relativistic effects: The effect of spin–orbit coupling in closed shell molecules, *J. Chem. Phys.*, 1996, **105**, 6505–6516.

54 Z. Luo, A. C. Reber, M. Jia, W. H. Blades, S. N. Khanna and A. W. Castleman, What determines if a ligand activates or passivates a superatom cluster?, *Chem Sci*, 2016, **7**, 3067–3074.

55 M. B. Abreu, C. Powell, A. C. Reber and S. N. Khanna, Ligand-Induced Active Sites: Reactivity of Iodine-Protected Aluminum Superatoms with Methanol, *J. Am. Chem. Soc.*, 2012, **134**, 20507–20512.

Chapter 6

Ligand Effects in Heterogeneous catalysis using Palladium clusters on supported defected graphene, reduced graphene oxide, and graphene acid

6.1 Background

The Cross-Coupling(C-C) reaction is a chemical phenomenon that couples two isolated hydrocarbon fragments using a suitable metal catalyst.[1–3] Serving as an essential tool for complex molecular synthesis, the metal-catalyzed C-C cross-coupling reaction has revolutionized the field of synthetic chemistry. As a result, the practical application of the reaction is omnipresent, including pharmaceutical, chemical industries, and green energy companies.[4,5] The reaction is routinely used to synthesize various materials from polymers, medicinal to natural products. In a simplified manner, the overall reaction can be represented as,

$$R_2 - N + R_1 - X \xrightarrow{[M]} R_2 - R_1 + N - X \qquad \textbf{(6.1)}$$
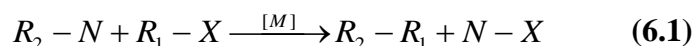
where the final product R_2-R_1 (R_2, R_1 = hydrocarbon fragments) of the reaction is synthesized by the reaction between an organometallic molecule (R_2-N) and an organic halide R_1-X in the presence of a metal catalyst M.[1–3] A general schematics of the whole catalytic cycle is shown in Figure 6.1. In standard conditions, the C-C bond formation process is energetically unfavorable; hence a suitable catalyst is required to achieve a reasonable reaction rate and a decent chemical yield. Thus, the synthesis and utilization of versatile and efficient catalysts are essential. Among the available options, the homogenous Pd(0) based catalysts are the most popular because they usually lead to high turnover frequencies (TOFs).[6] These catalysts were primarily developed in the early 1970−80s, which rightfully earned the 2010's Nobel prize in chemistry.[7]

[M] = Pd, Ni, Fe, Cu, Rh ... etc
[N] = B, Al, Li, Mg, Si, Sn, Zn, Zr ... etc
X = Br, I ... etc
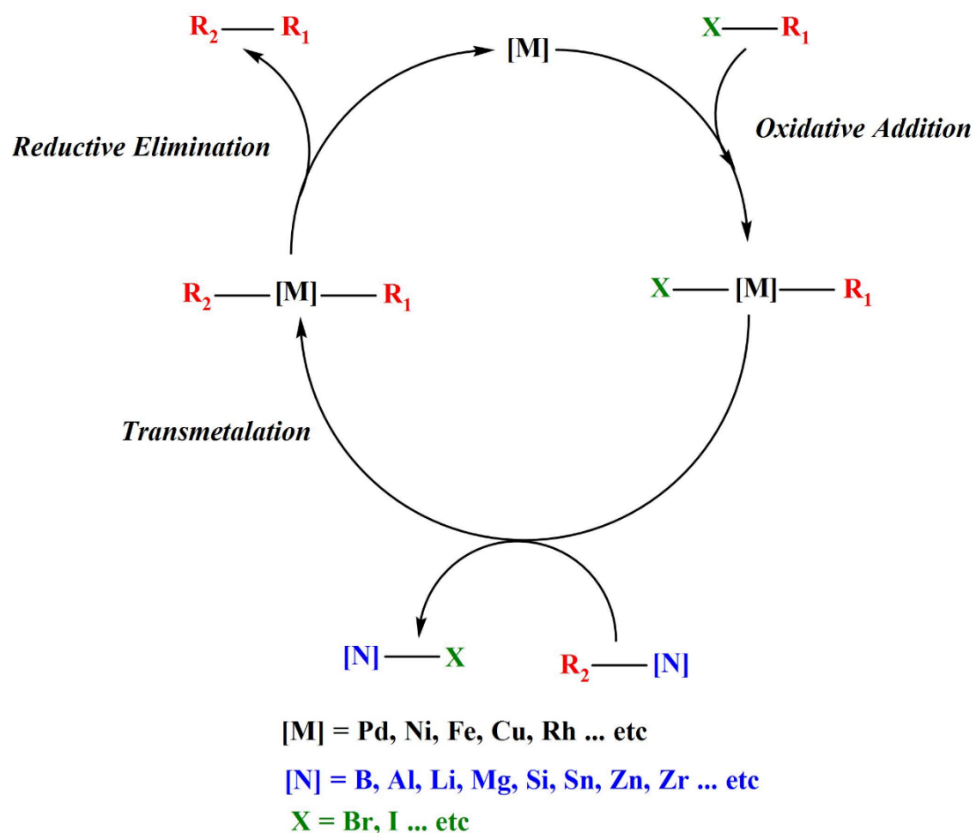
Figure 6.1 A generalized schematic of the cross-coupling reaction

The Suzuki−Miyaura[8,9] (or commonly known as Suzuki reaction) C−C cross-coupling reaction is a variation of the conventional coupling reaction in which an organo-boronic compound (aryl alkenyl, alkynyl, etc.) is treated with organo-halide under a basic condition and in the presence of a suitable palladium catalyst (Figure 6.2). An organometallic palladium (0) compound, e.g., $Pd(PPh_3)_2$, catalyzes the reaction. As shown in Figure 6.2, the overall catalytic cycle proceeds via three significant steps a) oxidative addition, b) transmetalation, and c) reductive elimination. In the oxidative addition step, the carbon-halogen (R_1-X) bond gets dissociated at the active site of the organometallic catalyst. In this step, the metal donates an electron pair to the empty antibonding orbital of the R_1-X bond resulting in the dissociation of the respective bond. Due to the donation

136

of the electron pair, the Pd (0) metal gets oxidized to Pd (II). Since the reaction is carried out in a

basic condition (e.g., aq NaOH), in the next step, the halide ion is first replaced by the OH⁻ ion,

followed by a Lewis acid-base adduct formation between the boron and the metal catalyst. In the

transmetalation step, the R_2 group is transferred to the Pd (II)
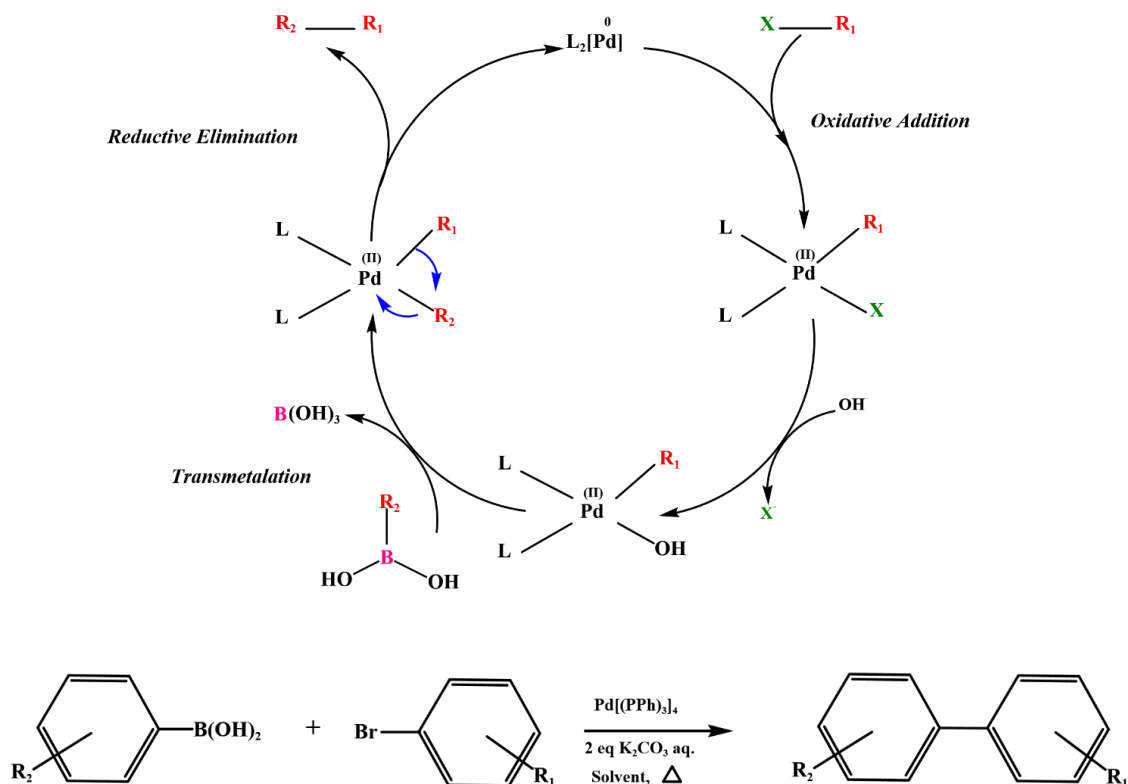
Figure 6.2 The catalytic cycle of the Suzuki cross-coupling reaction.

metal center from the boron atom via an intramolecular substitution. The boron atom leaves the

coordination sphere of the metal as boric acid (B(OH)$_3$). In the final step, i.e., reductive

elimination, the Pd (II) is reduced to Pd (0) via the formation of the coupled product (R_2−R_1), and

the catalyst is regenerated for the next cycle. The developments in synthetic chemistry have

increased the accessibility to molecules of greater chemical complexity through C-C couplings.

These reactions are typically performed under homogenous conditions, utilizing ligands to enhance activity and selectivity, and are widely used in synthetic chemistry. However, the process leads to residual metal contaminating the reaction product as the metal in the solution is used to catalyze the reaction.[10] This is mainly a significant problem where C-C reactions are extensively used. The palladium compounds being highly toxic and the inability to recycle the metal and the ligand result in a significant cost component in catalytic applications.[11] One way to overcome such limitations is to perform the catalysis by particles that can strongly bind to the supports that would prevent the leaching of the catalyst into the solutions. These have led to the utilization of palladium metal clusters with a wide range of traditional catalyst support systems utilizing various synthetic techniques.[10,12–15] The development of supported catalysts that could reduce or eliminate leaching and sintering while enabling the recyclability processes would be a massive stride in enhancing the performance and reducing the cost of the synthesis for various applications. Realizing the elements controlling the different reaction steps in the catalysis using the Pd_n cluster on the surface, including the function of support in lowering the reaction barriers, is the first step towards improving the catalysts. Moreover, such insight could also offer pathways to replace Palladium with less expensive and more effective metals.

Since the catalytic activity is directly proportional to the total available surface area, and smaller particle-like clusters show significantly higher catalytic activity than larger ones. The support also immobilizes the clusters as well as stabilizes them against coalescence. Additionally, the support aids in recovering the catalysts after the reaction is complete and helps in the separation of the product mixture. Thus, the recoverability and reusability of such heterogeneous catalysts are much higher than the conventional homogeneous catalyst, which also reduces the overall cost of the synthesis. The clusters can be kept pristine or coated with ligands. The ligands prevent smaller

clusters from coalescence and help to bind the cluster with the surface firmly. For catalytic purposes, oxides like silica (SiO_2), titania (TiO_2), alumina (Al_2O_3), etc., are usually chosen as the support. It is essential to mention that the support does not always play a passive role; the interaction between the support and the cluster can also activate clusters toward particular reactions.[16] Thus, the choice of support is essential to stabilize the clusters and enhance the catalytic performance of the nanoclusters with careful selection.

It was recently discovered that palladium particles supported on reduced graphene oxide could represent a high-performance heterogeneous catalyst. These studies concentrated on a template Suzuki reaction using 4-bromobenzoic acid and phenylboronic acid as reagents. The reaction follows a three-step pathway of oxidative addition, trans-metalation, and reductive elimination steps that could be recycled multiple times, thus overcoming the leaching and recyclability issues.[16] Yuan et al. synthesized Pd nanoparticles supported on graphene oxide by impregnating Pd precursor with graphene oxide followed by hydrazine and microwave heating co-reduction. Structural investigations using STM and other probes indicated that such a method generates vacancy defect sites/voids in the graphene sheet with the Pd_n clusters strongly binding to these vacancies/voids. It was remarkable that the resulting catalysts exhibited outstanding catalytic activity (Table 6.1) compared to other support systems with turnover frequencies (TOF) that were orders of magnitude higher than other catalysts.

Table 6.1: Comparison of TOF for different solid state supports for C-C reactions

Solid Support	Turn Over Frequency (TOF) (hr^{-1})
Defected Graphene	230,000
Graphite Oxide	39,000
Silica	25,000
Al_2O_3	9,600

Furthermore, only minor metal leaching was observed during Suzuki cross-coupling reactions (<300 ppb Pd in the reaction mixture). The catalysts could be retrieved and recycled multiple times without significant loss of catalytic activity. The enhanced catalytic activity and the strong binding of Pd clusters to the graphene support suggested that a unique interfacial interaction was occurring between Pd nanoclusters and defected graphene. The role of support as the theoretical investigations demonstrates that the resulting metal-ligand interaction promotes electron flow between the metal cluster and the defected graphene due to the conductive nature of the support facilitating any charge transfer to and from the reactants. Hence, such supports enhancing charge donation and acceptance imply that the graphene surface functions as a solid-state ligand. These findings indicate that further functionalization of the cluster or support can lead to better catalyst.[18]

Our group is working with an experimental collaboration to compare the catalytic efficiency of Pd_n clusters adsorbed on different graphene supports. In this present chapter, by using the density functional theory, we have investigated the effect of graphene functionalization toward Suzuki[8,9] cross-coupling reaction. The solid supports which are considered in this chapter are double vacant graphene (G), reduced graphene oxide (RGO), and graphene acid (GA). The primary focus of the research is to figure out which Pd_n cluster adsorbed graphene-based support works best for the catalytic enhancement of Suzuki C-C reactions. Furthermore, the reasoning behind such catalytic enhancement of the functionalized RGO and GA is also explored. As the related experiments are still going on, we will only present our side of the story. The work is organized as follows. First, we have identified and optimized the global minima of Pd_n clusters considering several possible spin multiplicities. We have chosen only the Pd_{13} cluster for the reaction pathway calculations as having a larger cluster size would provide a greater reactive site for catalytic activities. Additionally, the size of the Pd_{13} cluster is well suited according to the

experimental specifications. We have utilized cluster models for the three graphene-based supports, and the carbon atoms at the edges are saturated by using hydrogen atoms. A detailed discussion regarding the computational method is given in Chapter 3 of this thesis.

Furthermore, the calculated results also include the optimized structure of the pristine, single, and double carbon vacant graphene surface. Doping of Pd_{13} was more suitable on double carbon vacant graphene surface as the earlier investigations have shown that double vacant graphene support exhibited better binding with the Pd cluster.[19] Hence, the optimized structures of double vacant graphene (G), reduced graphene oxide (RGO), and graphene acid (GA) are identified and considered for adsorbing Pd_n clusters.

Then the reaction pathways for each support are computed. Finally, the comparison of catalytic activity between different supports is compared.

2. Results and Discussion

(a) The ground-state structure of palladium clusters
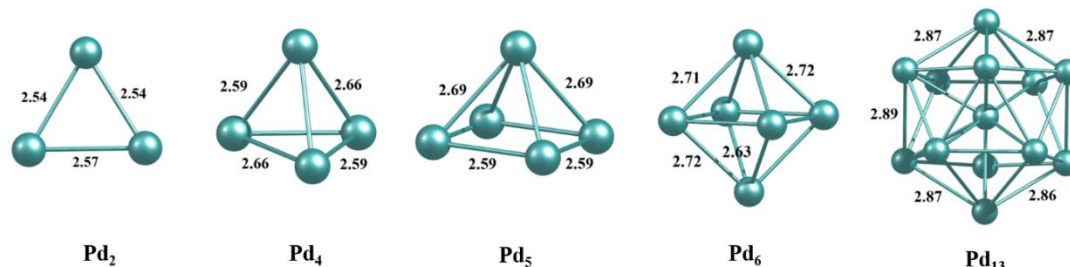
Figure 6.3. Optimized structure (ADF: PBE/TZ2P+ZORA) of the Pd_n (n=3−6, 13) clusters. Bond lengths are presented in Å unit.

The Pd_n cluster is widely used in catalysis as Pd has a very stable 0 and +2 oxidation state and can be easily switched back and forth between those oxidation states. Therefore, Pd_n clusters can act as a perfect 2-electrons donor in the oxidative addition step and an excellent 2e acceptor in the reductive elimination during cross-coupling reactions.[20] As for the nanoclusters, we have chosen

a series of small- to medium-sized palladium clusters. The selected clusters are Pd_3, Pd_4, Pd_5, Pd_6, and icosahedral Pd_{13}, respectively. The ground state for the transition metal clusters usually has high spin multiplicity. To detect the ground state structure, we have performed optimization employing different spin multiplicities within a range of 3 to 13. Their relative energies and binding energies (per atom) of the lowest energy structure are listed in Table 1. As seen from Table 6.2, the ground state spin multiplicities of Pd_3-Pd_6 are triplet, whereas the spin multiplicity of icosahedral Pd_{13} is nonet. The calculated binding energies (ΔE_b by equation (2)) are observed to increase with the size of the palladium cluster. Figure 6.3 includes the optimized structures of the clusters as obtained by ADF[21] (non-periodic) calculation. Based on the non-periodic calculations, it is observed that the ground state structure of Pd_3 is a triangle, and Pd_4 is a tetrahedron. On the other hand, the global minima of Pd_5 is a tetragonal pyramid, and Pd_6 is an octahedron, as shown in Figure 6.3.

$$\Delta E_b = \frac{n.E_{Pd} - E_{Pd_n}}{n} \qquad (6.2)$$

Where E_{Pd_n} is the energy of the cluster and E_{Pd} is the energy of the palladium atom.

Table 6.2 Relative Energies of Selected Pd_n Clusters at Different Spin Multiplicities (PBE/TZ2P)

Spin Multiplicity (2S+1)	Relative Energy (eV)				
	Pd_3	Pd_4	Pd_5	Pd_6	Pd_{13}
1	0.01	0.09	0.07	0.04	0.42
3	**0.00**	**0.00**	**0.00**	**0.00**	0.35
5	1.75	1.43	0.86	0.83	0.27
7	4.56	3.78	2.10	1.74	0.16
9	9.46	6.75	4.23	2.92	**0.00**
11	16.12	12.33	8.45	6.40	1.55
13	23.57	18.27	13.91	10.3	3.19
ΔE_b (eV)[*]	**1.10**	**1.50**	**1.61**	**1.75**	**2.07**

[*]Binding energies (ΔE_b) of the lowest energy structure are given.

(b) The optimized geometries of graphene-based supports

By using a cluster model, non-periodic calculations for pristine graphene are performed with a fragment of 112 carbon atoms. H atoms truncated the carbon atoms at the edges. Thus, the stoichiometric composition for the pristine graphene fragment is $C_{112}H_{26}$. The cluster model for the single ($C_{111}H_{26}$) and double ($C_{110}H_{26}$) vacant graphene is constructed by removing one and two C atoms from the center of the optimized $C_{112}H_{26}$ structure, as shown in Figure 6.4. It is also observed that upon introducing carbon defect (single or double), the HOMO−LUMO gap of the cluster models is reduced by ~0.35eV (Figure 6.4). Also, as expected, the C−C bond lengths are mainly altered surrounding the defect and near vicinity.
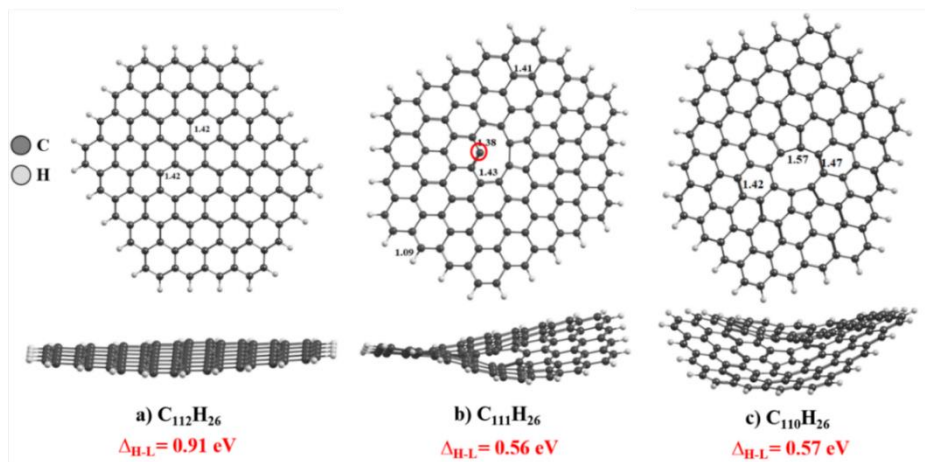
Figure 6.4. Optimized (ADF:PBE/TZ2P) geometries of a) pristine ($C_{112}H_{26}$) b) single C vacancy ($C_{111}H_{26}$) and (c) double C vacancy ($C_{110}H_{26}$) graphene sheets. The calculated HOMO−LUMO gaps ($\Delta_{H\text{-}L}$) and important bond lengths (Å) are also included.

However, the C−C bond length did not change (as with pristine graphene) in the regions further away from the defect. The optimized structure of doubly defected graphene was used as a template to generate and obtain the optimized structure of reduced graphene oxide (RGO) and Graphene acid (GA) by attaching hydroxyl (-OH), epoxy (-O-) groups (for RGO) and the carboxylic acid (-COOH) groups (for GA) at random locations on the sheet, respectively, as shown in Figure 6.5.

(a) RGO ($C_{110}H_{28}O_5$) (b) GA ($C_{115}H_{30}O_{10}$)

C
H
O
N

Δ_{H-L} = 0.35 eV
M = 0 μ_B

Δ_{H-L} = 0.081 eV
M = 2 μ_B
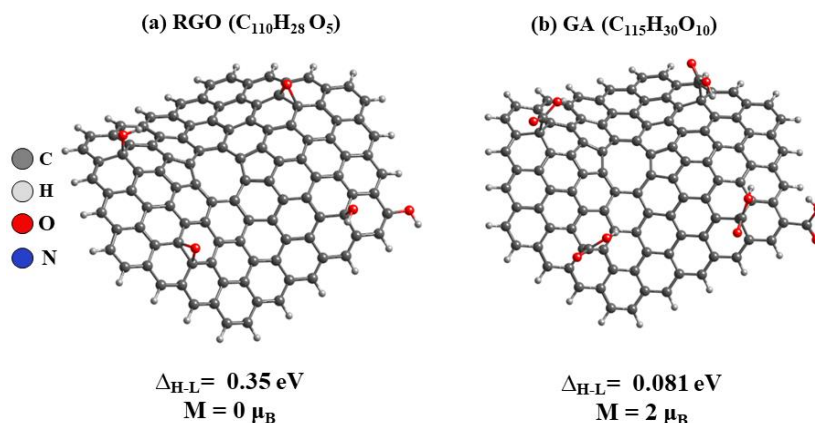
Figure 6.5 Optimized (ADF: PBE/TZ2P) geometries of (a) RGO ($C_{112}H_{28}O_5$) and (b) GA ($C_{115}H_{2306}$). Calculated HOMO−LUMO gaps (Δ_{H-L}) and and spin polarization (μ_B) are also included.

(c) Reaction pathway for the interacting/ non-interacting systems: Pd$_{13}$ on graphene-based supports

After obtaining the ground state geometries for Pd$_n$ and graphene supports, we calculated the reaction pathway for the Suzuki cross-coupling reaction on the Pd$_n$ cluster adsorbed surface. According to the experimental specifications, the Pd$_{13}$ cluster was the most suitable due to its larger size; hence, we considered it the cluster of choice for studying the reaction pathway. As for the model of chemical reaction, we have chosen the synthesis of biphenyl (Ph–Ph) via the Suzuki cross-coupling reaction between bromobenzene (Ph–Br) and phenylboronic acid (Ph–B(OH)$_2$). We have first adsorbed the Pd$_{13}$ cluster at the respective vacancy of each graphene-based support. After that, the bromobenzene molecule is adsorbed and optimized on the cluster surface to generate the pre-reaction complex. We have considered many different Ph–Br molecule orientations and the lowest energy conformer is considered for calculating the complete reaction pathway. Since, in RGO and GA, the functional groups (–OH, –O–, –COOH) distributed on the surface can also

144

interact with the cluster, we have computed two separate pathways. The first one is the non-interacting pathway in which the ligands do not interact with the adsorbed Pd_{13} cluster. Since defected graphene does not contain any functional group on the surface, the reaction pathway on supported double vacant graphene also falls under this category. In contrast, the other case is the reaction pathway of the interacting systems, i.e., when the functional groups interact with the Pd_{13} clusters, thereby influencing the activation barrier. In the following sections, we have presented a summary of our calculated results for both types of systems.

(i) Non-interacting systems
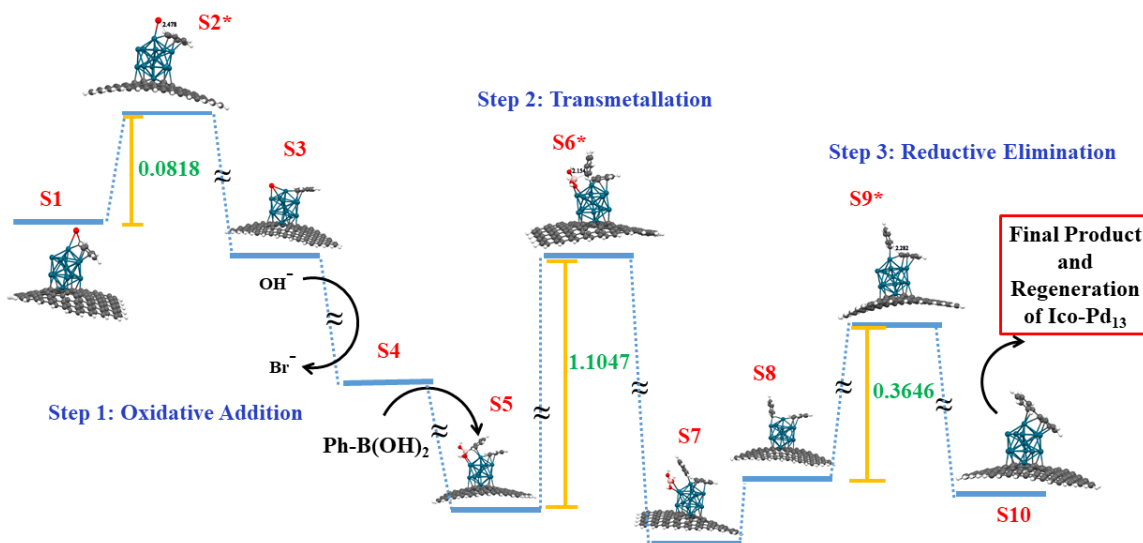
Figure 6.6 Reaction Pathway for the non-interacting system in case of Pd_{13} on defected Graphene Support.

As mentioned before, our first set of calculations involves computing the reaction pathway for the non-interacting systems, i.e., when the functional ligands (–OH, –O–, –COOH) do not interact with the Pd_{13} cluster on RGO or GA. The Pd_{13} cluster adsorbed on a double vacant graphene surface can also be regarded as a non-interacting system and hence also included herewith. Figures 6.6, 6.7, and 6.8 show the calculated reaction pathways alongside the structure of the respective

geometries and the energy barriers for a complete Suzuki cross-coupling reaction using the supported Pd_{13} cluster as the catalyst. The reaction pathway of the Suzuki Cross-Coupling reaction for the Pd_{13} cluster supported on defected graphene (G) is shown in Figure 6.6. The reaction barriers for oxidative addition, transmetallation, and reductive elimination steps for non-interacting systems are given in Table 3. The step with the highest activation barrier is regarded as the most critical rate-determining step for any catalytic cycle. Here, as seen from Table 3, the transmetallation step is the rate-determining for all three cases. The barrier for the transmetallation is observed to be similar for G and RGO, whereas the same is found to be slightly higher for GA. A similar phenomenon is observed for the oxidative addition step. The activation barrier of oxidative addition for graphene and RGO is very similar. In the case of graphene surface (0.0818 eV), it is marginally lower than RGO (0.092 eV). The barrier height of oxidative addition on GA is slightly higher than both G and RGO. The energy data for the reductive elimination is found to be quite interesting. In this step, The RGO shows a significantly lower barrier (0.299 eV) than the other two systems (Table 6.3). The GA offers the highest barriers in this step, similar to the oxidative addition and transmetallation steps.

Table 6.3 Comparison of energy barriers of the three important steps of C-C reactions for the non-interacting systems.

Surface	Oxidative Addition (eV)	Transmetallation (eV)	Reductive Elimination (eV)
Graphene (G)	0.0818	1.1047	0.3646
RGO	0.092	1.097	0.299
GA	0.114	1.126	0.396

A similar phenomenon is observed for the oxidative addition step. The activation barrier of oxidative addition for graphene and RGO is very similar. In the case of graphene surface (0.0818 eV), it is marginally lower than RGO (0.092 eV). The barrier height of oxidative addition on GA is slightly higher than both G and RGO. The energy data for the reductive elimination is found to be quite interesting. In this step, The RGO shows a significantly lower barrier (0.299 eV) than the other two systems (Table 6.3). The GA offers the highest barriers in this step, similar to the
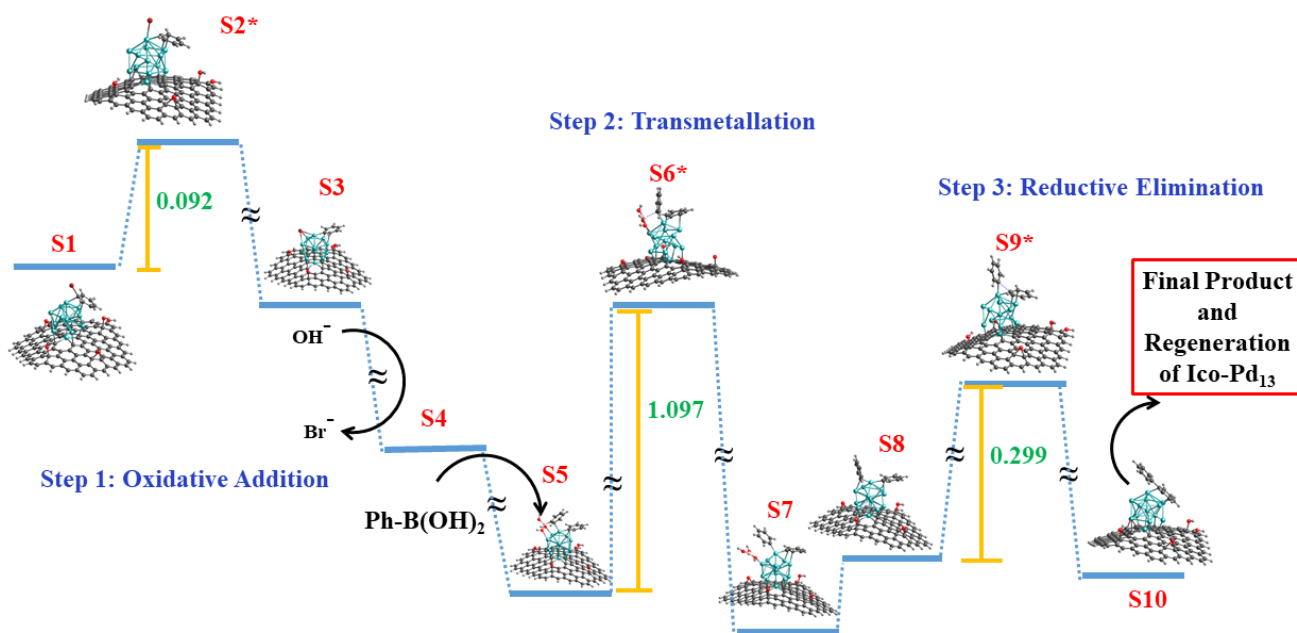
Figure 6.7 Reaction Pathway for the non-interacting system in case of Pd_{13} on RGO support.

oxidative addition and transmetallation steps. Thus, considering all three cases, it can be projected that GA's catalytic performance will be the worst for the non-interacting systems. In contrast, it can be expected that the graphene and RGO will show near similar catalytic efficiency. The performance of the RGO supported system appears marginally better than the graphene due to the lower barrier of the reductive elimination step.
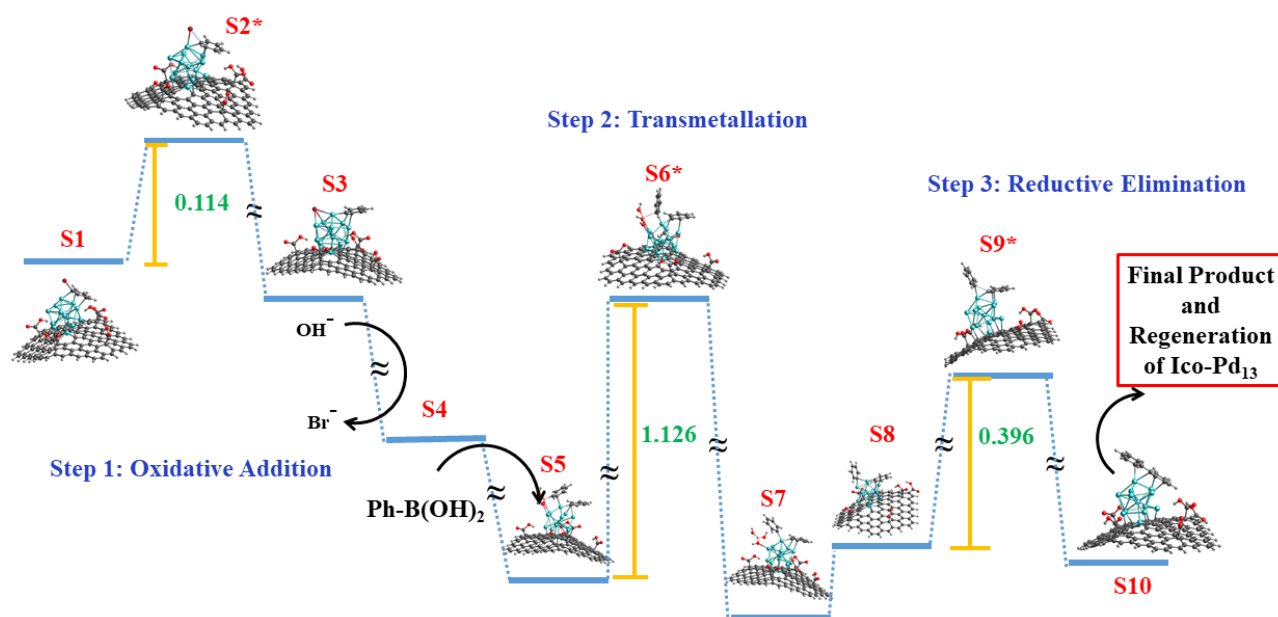
Figure 6.8 Reaction Pathway for the non-interacting system in case of Pd_{13} on GA Support.

(ii) Interacting systems

Since the donor-acceptor characteristics of a cluster can be easily altered by attaching ligand to the surface, it is expected that the cluster will behave differently when the functional group on the support interacts with the cluster. Thus, the catalytic performance, including the barrier heights, is also expected to be altered upon ligand interaction. Our calculation showed a similar observation. We have calculated the reaction pathways and the energy barriers for a complete Suzuki cross-coupling reaction using the Pd_{13} cluster for two interacting systems shown in Figures 6.9 and 6.10. The reaction barriers for oxidative addition, transmetallation, and reductive elimination steps for these two interacting systems are provided in Table 6.4. The transmetallation step with the highest energy barrier has remained the rate-determining step and was observed to be very close for both cases. However, GA shows a lower barrier for both the oxidative addition and reductive elimination steps compared to RGO. The oxidative addition

148

barrier is lowered by 0.04 eV, whereas the reductive elimination is lowered by 0.03 eV. Important to note the 0.074 eV barrier height, as obtained for GA, is the lowest barrier among all the reported ones in this chapter. Thus, from the computed results, it can be expected that if the functional groups on the surface interact with the cluster, GA will show the best catalytic performance among all.
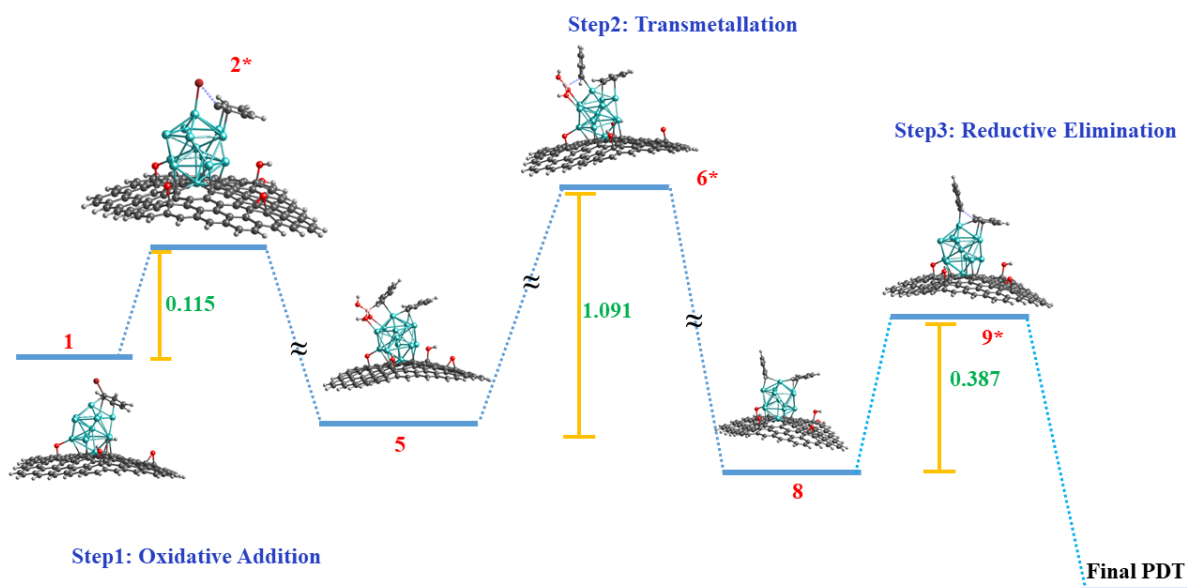
Figure 6.9 Reaction Pathway for the interacting system in case of Pd_{13} on RGO support.

Table 6.4 Comparison between energy barriers for different steps in Pd_{13} adsorbed on RGO and GA supports for interacting systems.

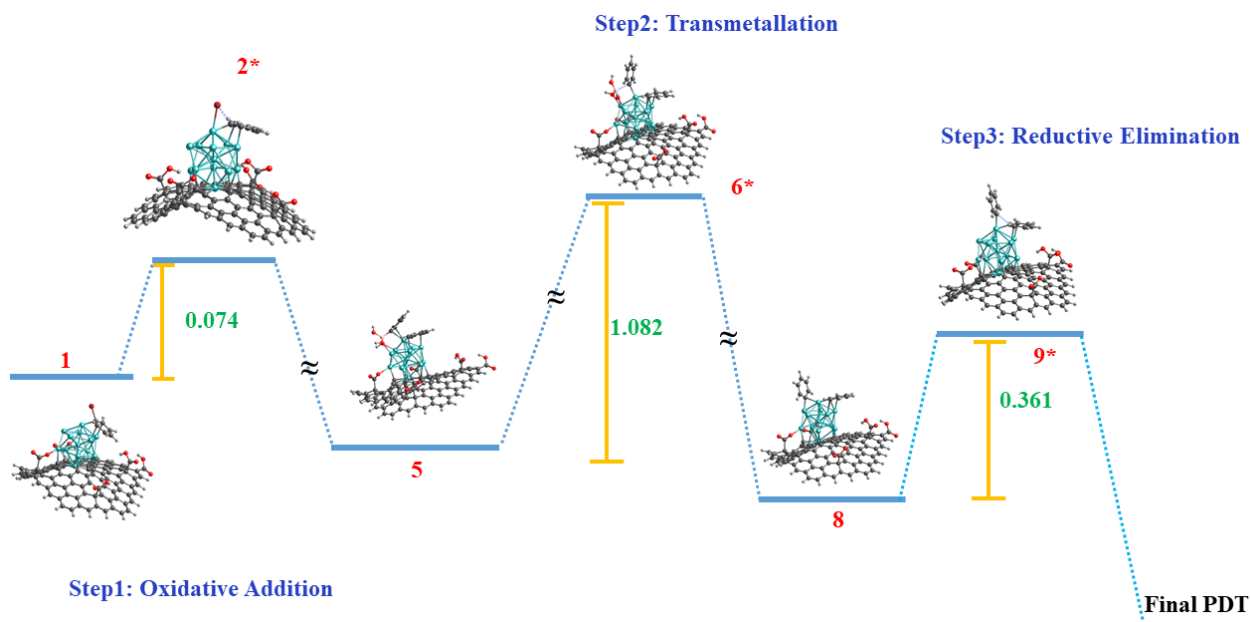| Surface	Oxidative Addition (eV)	Transmetallation (eV)	Reductive Elimination (eV)
RGO	0.115	1.091	0.387
GA	0.074	1.082	0.361

Figure 6.10 Reaction Pathway for the interacting system in case of Pd$_{13}$ on GA support.

3. Conclusion

The catalytic performance of the Suzuki C-C reactions for three different Pd$_{13}$ doped graphene surfaces is investigated through the first-principles calculations. Two distinct models are designed: a non-interacting system, where the ligands on the graphene surface do not interact with the adsorbed Pd$_{13}$ cluster, and an interacting system where the ligands on the surface interact with the Pd$_{13}$ cluster. The transmetallation step turned out to be the rate-determining step; however, the barrier height for this step is almost the same for all compared systems. However, the reaction barriers for oxidative addition and reductive elimination steps showed that the Pd$_{13}$ adsorbed RGO surface acts as the best catalyst for a non-interacting system. On the other hand, the Pd$_{13}$ doped GA surface demonstrated better catalytic enhancement in an interacting system.

Next, the search for cheaper and effective catalysts continued using other more inexpensive transition metal clusters such as Ni_{13}, Fe_{13}, etc., and adsorbing them on different graphene supports for better catalytic performance. Recently, Yuan et al. also considered the possibility of reducing the activation energy of the supported catalysts by using bimetallic catalysts. $Ni_{12}Pd$ and $Pd_{12}Ni$ clusters, which were created by impregnating one transition metal atom endohedral at the center.[19] Then, the reaction pathways for the Suzuki C-C reaction were computed. The results showed that the electronic properties of the individual Pd and Ni active sites are modified significantly in the bimetallic cluster, altering the charge donating and accepting capability of the atoms, which then translated into the variation of the activation energies. They also found that depositing the bimetallic clusters on the graphene surface further decreased the activation energy.

Hence, for our future work, we plan to incorporate noble metal atoms like silver atoms (Ag) on the vertex of the icosahedral Pd_{13} cluster instead of endohedral doping of Ag-atom. The bimetallic $Pd_{12}Ag$ cluster might result in the efficient catalyst as we deem doping Ag-like metal on the outer surface instead of at the centre of the cluster would significantly change the charge distribution of the cluster's surface. Consequently, the property of the surface can be substantially altered, which can be confirmed via conceptual density functional theory. The choice of noble metal atoms like Ag is driven by its electronic configuration with a filled d-shells and a single 5s electron. Hence, it can act as an efficient donor or acceptor by losing 5s-electron or accepting an electron to complete 5s-shell respectively, thereby enhancing the catalytic activity of nearby Pd-sites. Furthermore, Ag is significantly less expensive than the Pd. Hence, the $Pd_{12}Ag$ blend might serve as an efficient and inexpensive catalyst. The reaction pathways can be calculated to check whether such bimetallic $PdAg_{12}$ clusters can significantly reduce the barrier heights of the redox steps of

Suzuki coupling compared with the pristine Pd_{13} clusters. Additionally, computing the reaction pathways by adsorbing bimetallic $Pd_{12}Ag$ clusters on different graphene supports such as double vacant graphene, reduced graphene oxide, and graphene acid would be the next step towards finding a novel heterogeneous catalyst for C-C reactions.

References

1 N. Miyaura and S. L. Buchwald, *Cross-coupling reactions: a practical guide*, Springer, 2002, vol. 219.

2 F. Diederich and P. J. Stang, *Metal-catalyzed cross-coupling reactions*, John Wiley & Sons, 2008.

3 T. Kohei and N. Miyaura, in *Cross-Coupling Reactions*, Springer, 2002, pp. 1–9.

4 A. Dumrath, C. Lübbe and M. Beller, *Palladium-Catalyzed Coupling Reactions: Practical Aspects and Future Developments*, 2013, 445–489.

5 C. Torborg and M. Beller, *Advanced Synthesis & Catalysis*, 2009, **351**, 3027–3043.

6 P. Mpungose, Z. Vundla, G. Maguire and H. Friedrich, *Molecules*, 2018, **23**, 1676.

7 T. J. Colacot, *platin met rev*, 2011, **55**, 84–90.

8 A. Suzuki, *Journal of organometallic chemistry*, 2002, **653**, 83–90.

9 N. Miyaura and A. Suzuki, *Chemical reviews*, 1995, **95**, 2457–2483.

10 M. Pagliaro, V. Pandarus, R. Ciriminna, F. Béland and P. Demma Carà, *ChemCatChem*, 2012, **4**, 432–445.

11 I. P. Beletskaya and A. V. Cheprakov, in *The Mizoroki–Heck Reaction*, ed. M. Oestreich, John Wiley & Sons, Ltd, Chichester, UK, 2009, pp. 51–132.

12 S. Mukhopadhyay, G. Rothenberg, D. Gitis, H. Wiener and Y. Sasson, *J. Chem. Soc., Perkin Trans. 2*, 1999, 2481–2484.

13 I. W. Davies, L. Matty, D. L. Hughes and P. J. Reider, *J. Am. Chem. Soc.*, 2001, **123**, 10139–10140.

14 Z. Niu, Q. Peng, Z. Zhuang, W. He and Y. Li, *Chem. Eur. J.*, 2012, **18**, 9813–9817.

15 D. Astruc, *Chem. Rev.*, 2020, **120**, 461–463.

16 Y. Yang, A. C. Reber, S. E. Gilliland III, C. E. Castano, B. F. Gupton and S. N. Khanna, *Journal of Catalysis*, 2018, **360**, 20–26.

17 K. Yam, N. Guo, Z. Jiang, S. Li and C. Zhang, *Catalysts*, 2020, **10**, 53.

18 A. A. Ibrahim, A. Lin, M. S. Adly and M. S. El-Shall, *Journal of Catalysis*, 2020, **385**, 194–203.

19 Y. Yang, VCU Libraries, 2018.

20 E. D. Sultanova, V. V. Salnikov, R. K. Mukhitova, Y. F. Zuev, Y. N. Osin, L. Ya. Zakharova, A. Y. Ziganshina and A. I. Konovalov, *Chem. Commun.*, 2015, **51**, 13317–13320.

21 G. t Te Velde, F. M. Bickelhaupt, E. J. Baerends, C. Fonseca Guerra, S. J. van Gisbergen, J. G. Snijders and T. Ziegler, *Journal of Computational Chemistry*, 2001, **22**, 931–967.

Chapter 7

Summary and Future Directions

To summarize, in this thesis work, I have explored the ligand effects on the different atomic clusters. It is shown that by attaching suitable donor/acceptor ligands, the electronic and magnetic properties of the ligated clusters can be modulated.[1] Additionally, by fusing two clusters through their unligated metal sites, dimers can be formed. The dimer formed by attaching Re_6S_8-based clusters ligated by phosphine and CO ligands on opposite sides of the dimer showed substantial applications in photovoltaics. It can also be realized as a nanoscale pn-junction.[2] Similarly, dimer formed by combing Fe_6S_8-based clusters exhibited potential applications in spintronics-related applications.[3] Then, a theoretical investigation is performed on the experimental synthesis of a cluster assembly,[4] which utilizes Co_6Se_8-based dimers as a building block with fullerene counterions.

Moreover, such dimers exhibited intriguing magnetic properties with interfacial magnetic moment localized at the junction where clusters fuse to form a dimer. Likewise, forming dimers are not only limited to the metal-chalcogenides clusters. It is shown by forming dimers of simple metallic clusters (Al-based) using organometallic linkers. These dimers are shown to be helpful in light harvesting.[5] Finally, it was shown that the Pd clusters adsorbed on solid support enhance the catalytic performance of Suzuki cross-coupling reactions. The catalytic performances of Pd adsorbed on three different surfaces: defected graphene, reduced graphene oxide, and graphene-acid were compared. The prospect of my research work would be exploring more applications using ligated metal chalcogenides clusters, which are briefly summarized below.

> ➤ Extending pn-junction to transistor by making appropriately fused trimer: A primitive calculation provided an optimized ground state structure of Re_6S_8 based trimer, as shown

in Figure 1. Donor cluster $Re_6S_8Cl_2C(PMe3)$ is sandwiched between acceptor clusters $Re_6S_8Cl_2CO_3$ to form an analog of PNP transistor. Similarly, using appropriate arrangements of donor-acceptor clusters, an NPN transistor analog can also be developed. However, a comprehensive study of essential transistor characteristics is further required to conclude that the proposed combinations of clusters exhibit realistic transistor's analogy. Furthermore, this scheme can be applied by combining other ligated metal-chalcogenides clusters which have better acceptor-donor characteristics.
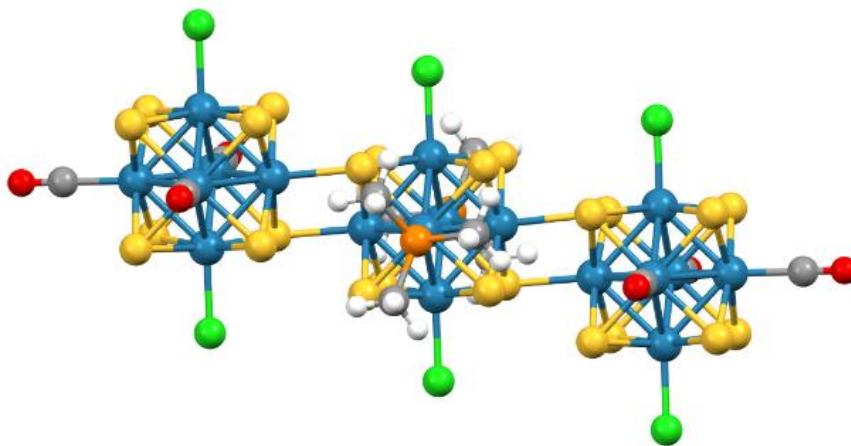

Figure 7.1 Optimized ground-state structure of $[Re_6S_8Cl_2(CO)_3]_2[Re_6S_8Cl_2(PMe_3)_3]$.

➤ Doping 2D metal dichalcogenides by magnetic cluster: This will be an extension of earlier work done by Reber et al., which showed that by doping suitably ligated Co_6Se_8 clusters on 2D WSe_2 surface, the characteristic-polarity of the 2D-semiconductor could be altered.[6] This theoretical work is inspired by an experimental job by Yu et al.[7] I want to explore if we can create a magnetic semiconductor by doping the Fe_6S_8-based magnetic cluster on the WSe_2 surface. As we know from our previous calculations, that the $Fe_6S_8(CO)_5$ cluster

has a spin multiplicity of 9.[3] When the $Fe_6S_8(CO)_5$ cluster is doped on a 2D WSe_2 surface, the spin multiplicity of the system remains 9. When CO ligands are subsequently exchanged by PMe_3 ligand one at a time until $Fe_6S_8(PMe_3)_5$ on WSe_2 is formed. Then, we can compare how the electronic and magnetic properties of the system (metal-chalcogenides clusters doped on the 2D surface) change. From preliminary calculations, it is seen that when all CO ligands are exchanged by PMe_3 ligands, the HOMO levels shift in an upward direction by almost 1.44 eV, matching our previous works.[1,6,8] Furthermore, the spin multiplicity stays the same throughout the transition, i.e., 9. Hence, exploring the electronic and magnetic properties of the whole series appears as an intriguing prospect. Consequently, such systems might serve as magnetic semiconductors.

(a)

$Fe_6S_8(CO)_5WSe_2$
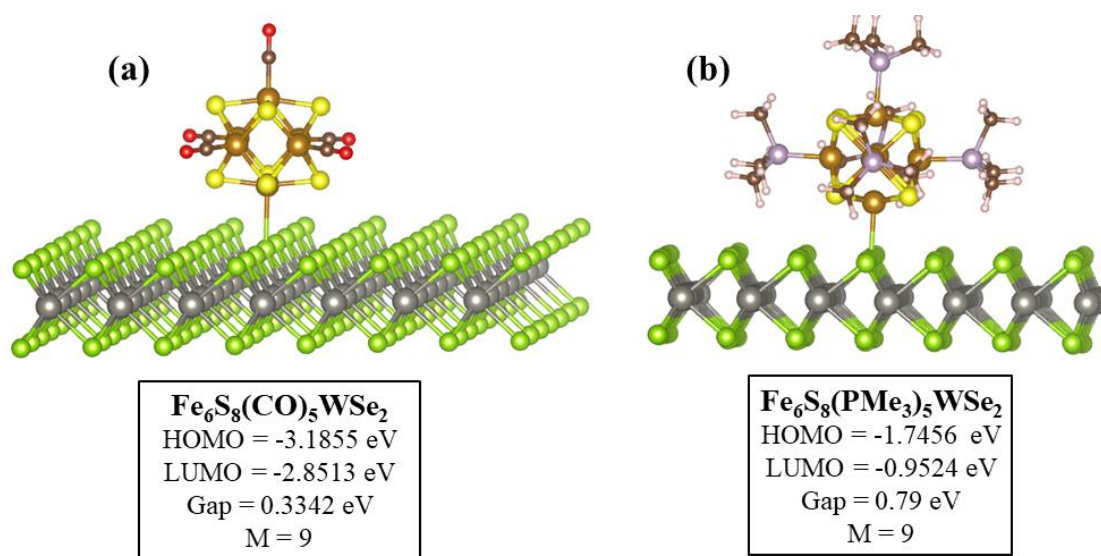HOMO = -3.1855 eV
LUMO = -2.8513 eV
Gap = 0.3342 eV
M = 9

(b)

$Fe_6S_8(PMe_3)_5WSe_2$
HOMO = -1.7456 eV
LUMO = -0.9524 eV
Gap = 0.79 eV
M = 9

Figure 7.2 Electronic and magnetic properties of (a) $Fe_6S_8(CO)_5WSe_2$ (b) $Fe_6S_8(PMe_3)_5WSe_2$.

➢ Doping noble metal atoms on the surface of Pd_n clusters to create an efficient and inexpensive catalyst: The key idea is to dope the surface of the Pd_n clusters with noble atoms such as Ag or Au aiming to alter the characteristics of the surface. The electronic characteristics of the Ag/Au atom, which has a filled d-shells and single 5s or 6s electrons, can make the Pd_n cluster act as an efficient donor or acceptor. The added donor/acceptor efficiency in the bimetallic cluster might lower the barriers in different steps of catalytic reaction pathways. Furthermore, the Ag/Au atoms are less expensive than Pd.

➢ Generalizing Superatomic Framework for ligated metal-chalcogenides clusters: The superatomic concept for simple metal clusters is generally exemplified by using nearly free electron gas. As described in the first chapter of this thesis, the stability of ligated metal-chalcogenides clusters in the solution and the formation of cluster-assembled materials with exciting properties from metal-chalcogenides clusters make them interesting spices in cluster science. It would be fascinating to explain the stability of ligated metal-chalcogenide clusters and their assembles from the superatomic framework. We can look if any specific magic numbers are available for the ligated metal-chalcogenide clusters and build our framework based on such a trend.

➢ Using Machine Learning (ML) and data-mining for predicting the properties of the metal-chalcogenide dimer formed by utilizing monomer clusters: As I have shown in my thesis that by combining two monomer units ($M_6X_8L_5$: M = Transition metal atom, X = chalcogen, L = CO/PMe$_3$ ligand), the dimer can be formed. I have already worked with three such systems and can be extended using other transition metal-atom or different chalcogens and various ligands also. Only using DFT can be computationally very

expensive. Hence, using DFT for few basic calculations and then using ML and data-mining can be a useful strategy to create a library of dimers.

References:

1   A. C. Reber, D. Bista, V. Chauhan and S. N. Khanna, *The Journal of Physical Chemistry C*, 2019, **123**, 8983–8989.

2   A. C. Reber, V. Chauhan, D. Bista and S. N. Khanna, *Nanoscale*, 2020, **12**, 4736–4742.

3   D. Bista, T. Sengupta, A. C. Reber and S. N. Khanna, *The Journal of Physical Chemistry A*, 2021, **125**, 816–824.

4   J. Yang, F. Wang, J. C. Russell, T. J. Hochuli, X. Roy, M. L. Steigerwald, X. Zhu, D. W. Paley and C. Nuckolls, *J. Am. Chem. Soc.*, 2020, **142**, 11993–11998.

5   D. Bista, V. Chauhan, T. Sengupta, A. C. Reber and S. N. Khanna, *Nanoscale*, 2020, **12**, 12046–12056.

6   A. C. Reber and S. N. Khanna, *npj Comput Mater*, 2018, **4**, 33.

7   J. Yu, C.-H. Lee, D. Bouilly, M. Han, P. Kim, M. L. Steigerwald, X. Roy and C. Nuckolls, *Nano Lett.*, 2016, **16**, 3385–3389.

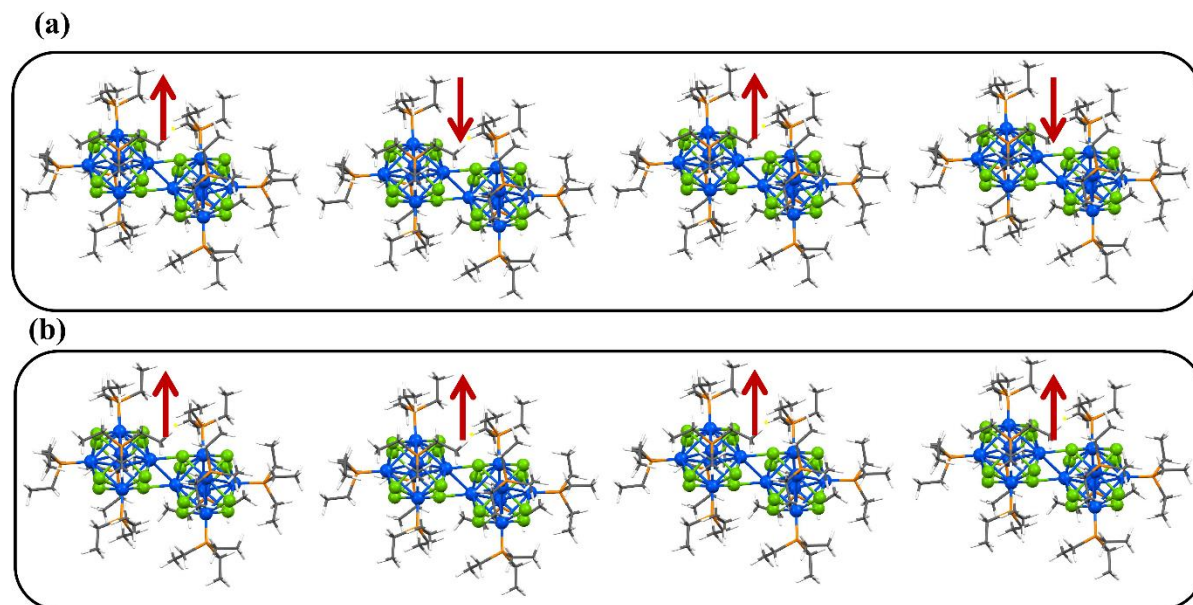8   V. Chauhan, A. C. Reber and S. N. Khanna, *J. Am. Chem. Soc.*, 2017, **139**, 1871–1877.

Appendix

Figure A1 Schematic showing (a) antiferromagnetic-coupling between dimers in the cluster assembled solid $\{[Co_6Se_8(PEt_3)_5]_2(Toluene)_2C_{140}\}_2$ (b) ferromagnetic-coupling between dimers in the solid. The red arrows show the direction of the spin-magnetic moment at the junction of the dimer. The antiferromagnetic coupling is more stable than ferromagnetic coupling by only 0.03 eV.